Electrochemical Sensors

and On-chip Optical Sensors

by

Tao Luo

A Dissertation Presented in Partial Fulfillment
of the Requirements for the Degree
Doctor of Philosophy

Approved August 2015 by the
Graduate Supervisory Committee:

Jennifer Blain Christen, Chair
Hongjiang Song
Michael Goryll
Hongbin Yu

ARIZONA STATE UNIVERSITY

December 2015

ABSTRACT

The microelectronics technology has seen a tremendous growth over the past sixty years. The advancements in microelectronics, which shows the capability of yielding highly reliable and reproducible structures, have made the mass production of integrated electronic components feasible. Miniaturized, low-cost, and accurate sensors became available due to the rise of the microelectronics industry. A variety of sensors are being used extensively in many portable applications. These sensors are promising not only in research area but also in daily routine applications.

However, many sensing systems are relatively bulky, complicated, and expensive and main advantages of new sensors do not play an important role in practical applications. Many challenges arise due to intricacies for sensor packaging, especially operation in a solution environment. Additional problems emerge when interfacing sensors with external off-chip components. A large amount of research in the field of sensors has been focused on how to improve the system integration.

This work presents new methods for the design, fabrication, and integration of sensor systems. This thesis addresses these challenges, for example, interfacing microelectronic system to a liquid environment and developing a new technique for impedimetric measurement. This work also shows a new design for on-chip optical sensor without any other extra components or post-processing.

ACKNOWLEDGEMENTS

It is a genuine pleasure to express my deep sense of thanks and gratitude to my advisor, Dr. Jennifer Blain Christen. I could not have finished this work without her guidance and support. Her enthusiasm, encouragement, and faith in me throughout have been extremely help.

Besides my advisor, I would like to thank the rest of my committee. I owe a deep sense of gratitude to Dr. Hongjiang Song for his valuable advice and constant patience for my research. His timely suggestions with kindness and dynamism have enabled me to finish my thesis. I would like to thank Dr. Michael Goryll for his great help and discussion throughout my research period. I want to express my gratitude to Dr. Hongbin Yu for serving as my committee since my qualified exam and for providing excellent comments.

I am extremely thankful to Dr. Hongyi Wang, who gives me excellent help in CMOS circuit design. Without his precious support it would not be possible to conduct this research.

I would like to thank Dixie Kullman, who is always willing to help and give her best suggestions. I thank my colleagues in our group, Hany, Jiu, Joe, Jon, Luyang, Neal, Uwa, Vishal, and Yuanda, for the stimulating discussions, and for the fun we have had in my graduate study.

I am very grateful to Cheng Lv for his support with the software.

My sincere thanks also goes to many ASU staff members, Dr. Stefan Myhajlenko, Carrie SinClair, Todd Eller. Special thanks to James Laux for his excellent Cadence support.

Last but not the least, it is my privilege to thank my father, Ziming Luo, my mother, Yanping Li, and my little sister, Wenwen Luo. They have given me constant

support and love throughout my entire life. I am grateful and unbelievably lucky to have them.

TABLE OF CONTENTS

Page

LIST OF TABLES viii

LIST OF FIGURES ix

CHAPTER

1 INTRODUCTION 1

2 ELECTROCHEMICAL METHODS 4

2.1 Cyclic Voltammetry 4

2.2 Electrochemical Impedance Spectroscopy 7

2.3 Square Wave Voltammetry 9

3 CYCLIC VOLTAMMETRY MEASUREMENTS 11

3.1 Background 11

3.2 System Overview 13

3.3 Potassium Ferricyanide CV Measurement by CMOS Potentiostat and Gamry 16

3.4 The Effect of Concentration and Scan Rate 17

3.5 Hexaammineruthenium Chloride CV Measurement by CMOS Potentiostat and Gamry Workstation 19

3.6 Potassium Ferricyanide CV Measurement with Three External Gold Electrodes 19

3.7 Conclusion 21

4 CMOS ELECTROCHEMICAL SENSOR AND PACKAGING 23

4.1 Background 23

4.2 System Overview 26

4.2.1 CMOS Potentiostat Structure 26

CHAPTER Page

4.2.2 Experimental Setup 27
4.3 Post-CMOS Electrode and Packaging 28
4.3.1 Die-Level Fabrication 28
4.3.2 Package-Level Fabrication 30
4.4 Results 31
4.5 Conclusion 33
5 PORTABLE IMPEDIMETRIC INSTRUMENT 34
5.1 Background 35
5.2 Complex Impedance Measurement Theory 36
5.3 Simulations 38
5.3.1 Verilog-A & Cadence Simulation 38
5.4 Randles Equivalent Circuit Measurements 40
5.4.1 Hardware 40
5.4.2 Experimental Setup 42
5.5 KCl Solution Measurements 44
5.6 Conclusion 45
6 A NEW IMPEDANCE MEASUREMENT METHOD 47
6.1 Background 47
6.2 Theory 48
6.3 Impedance Measurement System 50
6.4 Results and Discussion 52
6.5 Conclusion 58
7 SQUARE WAVE VOLTAMMETRY 59
7.1 Background 59

CHAPTER Page

7.2 Experimental Section 61
7.2.1 Chemical Reagents 61
7.2.2 System Architecture 62
7.2.2.1 Square Wave Relaxation Oscillator 63
7.2.2.2 Triangle Wave Relaxation Oscillator 64
7.2.2.3 Potentiostat & Current-to-Voltage Converter 65
7.2.3 Methods 65
7.3 Results and Discussion 66
7.3.1 SWV Analytical Characteristics of Individual Lead(II) 66
7.3.2 SWV Analytical Characteristics of Individual Copper(II) . . . 71
7.3.3 SWV Analysis of Simultaneous Detection of Copper(II) and Lead(II) 72
7.3.4 Evaluation of Copper(II) and Lead(II) Mutual Interference . 74
7.4 Conclusion 76
8 CMOS LIGHT-DIRECTION DETECTION SENSOR 77
8.1 Background 77
8.2 CMOS Sensor Structure 79
8.3 Theory 81
8.4 Results and Discussion 84
8.5 Conclusion 87
9 A SELF-POWERED SENSOR WITH DIGITALIZED OUTPUT FOR LIGHT DIRECTION 88
9.1 Background 88
9.2 Sensor Structure 89

CHAPTER Page

9.3 Principle of Operation 91

9.4 Results and Discussion 95

9.5 Conclusion 98

10 A SUN TRACKER WITH AN ON-CHIP SENSOR 99

10.1 Background 99

10.2 Sensor Design 100

10.3 Circuit Design 104

10.4 Implementation and Verification 108

10.5 Conclusion 113

NOTES 115

REFERENCES 116

LIST OF TABLES

Table Page

1 CMOS DAC Specifications 41

2 Currents and Current Ratio of the Photodiode versus Angle. 110

3 Parameters of Solar Panel 111

4 Parameters of Motor 113

LIST OF FIGURES

Figure Page

1 CV Potential Waveform 5

2 Cyclic Voltammogram 6

3 EIS Current Response in a Linear System 7

4 Impedance Plot for an Electrochemical Cell 8

5 Principle of Square-Wave Voltammetry. 9

6 Optical Micrograph of the 1.5 Mm × 3 Mm Die. 12

7 Single Channel Potentiostat Schematic for CV Measurements. 13

8 Amplifier Schematic for the Potentiostat Circuit. 15

9 CV Measurements of 100 MM Potassium Ferricyanide. 16

10 CV Measurements at Different Scan Rates. 17

11 CV Measurements for the Different Concentrations. 18

12 CV Measurements of 5 MM Hexaammineruthenium Chloride. 20

13 CV Measurement of Potassium Ferricyanide with Au Electrodes. 21

14 Photograph of Experimental Setup with Au Electrodes. 22

15 Photograph of the 1.5 Mm × 3 Mm CMOS Die. 26

16 Single Channel Potentiostat Schematic for CV Measurements. 27

17 Process for Post-CMOS Electrode Fabrication. 28

18 Photograph of Details before and after Electrode Fabrication. 29

19 Process for Package-Level Fabrication. 30

20 Photograph of Final Package Chip from above. 31

21 On-Chip Microelectrode CV Measurements. 32

22 Principle of Impedance Measurement. 37

23 Typical EIS Waveforms Showing Gain and Phase Shift at 1 KHz 38

Figure Page

24 Nyquist Plot of the Randles Circuit. 40

25 Microphotograph of the 1.5 Mm × 3 Mm CMOS Die. 41

26 Block Diagram of the Portable EIS System. 42

27 Nyquist Plot's Comparison of the Randles Circuit. 43

28 Nyquist Plot of 80 μl KCl Solution. 44

29 A Step Voltage V_ap Is Applied to a Randles Equivalent Circuit. 49

30 Proposed Integrated Impedance Measurement System. 50

31 Schematic Diagram of the Potential Step and Current Response. 51

32 Microphotograph of the Fabricated Chip. 52

33 A Potential Step and Its Response Current. 53

34 CMOS Impedance Measurement of the Randles Circuit. 54

35 Number of Bits B_int versus OSR at Various SNR Values. 58

36 A Schematic Diagram of the SWV System Architecture. 62

37 SWV Measurement Details. 67

38 SWV Response for Pb. 69

39 The Linear Fit Line of Pb Peak Current. 70

40 SWV Response for Cu. 71

41 The Linear Fit Line of Cu Peak Current. 72

42 SWV Response for Cu & Pb. 73

43 The Linear Fit Lines of Cu & Pb Peak Current. 73

44 SWV Response of Various Concentration Cu. 74

45 SWV Response of Various Concentration Pb. 75

46 Structure of the CMOS Light-Direction Sensor. 80

47 Diagram of the Basic Cell Geometry for the Light Direction Sensor. 81

Figure Page

48 Curves for R_D/B at Different α and β. 84

49 Micrograph of the CMOS Light-Direction Sensor. 85

50 Short-Circuit Photocurrents and the Ratio R_D/B. 86

51 Photocurrents and Ratio R_D/B vs. Incident Angle. 87

52 Structure of the On-Chip Light Direction Sensor. 90

53 Experimental Setup for Light-Direction Detection. 94

54 Micrograph of the Presented Chip. 95

55 Photocurrents of Each Diode at Different Angles. 96

56 Outputs of the Flash ADC versus the Angle of the Incident Light. 97

57 Comparison of the Tested Outputs. 98

58 Structure of the Proposed CMOS Light Direction Sensor. 101

59 Block Diagram of the Proposed Tracking Circuit. 105

60 Curve of the Tracking Circuit. 106

61 Microphotograph of the Chip. 108

62 Currents and Current Ratio of the Photodiode versus Angle. 109

63 Currents and Current Ratios of the Photodiode versus Light Power. 111

64 Photograph of the Tracking Setup. 112

65 Tracking Performance versus Light Power. 114

Chapter 1

INTRODUCTION

Electrochemical sensor research has experienced explosive growth over last thirty years. Typical electrochemical sensors are composed of transducers that detect changes in quantities and provide corresponding outputs, generally as electrical signals; electronic systems that include noise filters, signal amplifiers, and signal processors. More recently, since various sensors for electrochemical applications are being used extensively in daily lives, miniaturized, low-cost, and reliable sensors are required for routine applications. The wide use of these sensors can be mainly attributed to the rise of the microelectronics industry. Due to the advancements in microelectronics, sensors became small enough for portable applications with low power consumption and little heat generated. These advances have also enabled sensors to work at lower voltages to avoid expensive power supplies, leading to a reduction in the system cost. Small sensors only need small volumes of solutions and greatly reduce reagent costs, and the mass production. By eliminating solder joints and reducing interconnects, the fabrication technology of microelectronic meets the desire for highly reliable sensors. Moreover, advancements in microelectronic circuit technology allows for reducing noises, amplifying, and processing signals, causing no requirement of external electronic system. However, although several electrochemical techniques such as cyclic voltammetry, impedance spectroscopy, and square wave voltammetry have been developed, many electrochemical sensor systems are still sophisticated, bulky, and expensive. These instruments have been used as characterization tools rather than as

analytical tool for practical applications. Consequently, new and better electrochemical sensors need to be developed leveraging the advancement in microelectronics.

One problem is microelectronic circuits for signal read-out and processing. Small feature sensors generally generate small output signals. In order to obtain meaningful physical parameters, electronic signals from transducers need to be filtered, amplified, and processed. Since all the components are fabricated very close to each other, microelectronics are highly suitable for small signal operation. But it is not straightforward for microelectronic circuit to connect with transducers. In addition, microelectronic circuits should be close to the transducers, which can increase the signal-to-noise ratio. The combination of knowledge in electrochemistry, solid state physics, and electrical engineering offers the possibility of better sensors addressing this problem.

System integration in this design space presents numerous challenges. The first is material constraints for sensor packaging due to requirements for interface assembly, especially operation in a liquid environment. To meet these complicated constraints, die-level fabrication and post-package are proposed. Second, a custom fabrication process is used for the integration of microelectronic devices. However, some electrical interfaces of sensors such as nanowire array, nanoparticles, and optical devices can not be made by a standard fabrication process. Problems arise when connecting small size sensors with these external components. To overcome these issues, sensors without any other off-chip components or post-processing are developed.

This thesis describes new approaches for the design, fabrication, and packaging of sensor systems. The work presented here is organized as follows. Chapter 2 briefly discusses some background concepts about electrochemical methods such as cyclic voltammetry, electrochemical impedance spectroscopy, and square wave voltammetry. Chapter 3 demonstrates a CMOS potentiostat for chemical sensing

applications. The potentiostat chip is capable of performing cyclic voltammetry under different conditions such as varying scan rates and concentrations. The use of microfabrication processing allows for the integration of microelectronic circuits in the sensor substrate, providing a solution to portable sensors. Chapter 4 presents an on-chip electrochemical sensor. This sensor system shows all the advantages that make CMOS suitable for lab-on-a-chip platforms. Chapter 5 reports a portable electrochemical analysis system using impedimetric measurements instead of more commonly used potentiometric techniques. This impedimetric measurement system uses a small AC perturbation to get the impedance of an electrochemical cell without affecting it as opposed to cyclic voltammetry which repeatedly reduces and oxidizes the electrochemical cell. Chapter 6 presents a CMOS impedance measurement chip using a new impedance detection technique. The impedance of an electrochemical cell is measured by perturbing the system with a small potential stimulus instead of a small AC perturbation. The main advantage of this method includes an extremely short-time impedance measurements over the whole frequency range rather than measuring at each individual frequency. Chapter 7 describes a low-cost square wave voltammetry sensor based on relaxation oscillators. This chapter shows the ability to detect different chemical species simultaneously. Chapter 8 presents a novel method for light direction detection using commercial CMOS process. Design for this on-chip sensor is demonstrated without the requirement for other optical components or post-processing. Chapter 9 demonstrates a self-powered on-chip sensor for light-direction detection. This sensor provides digitized output and does not requires any off-chip power or external components. Chapter 10 shows an application of the on-chip light detection sensor, i.e. a solar tracking system capable of maximizing the energy harvesting.

Chapter 2

ELECTROCHEMICAL METHODS

Electrochemical methods are a class of techniques in electrochemistry to study the chemical response of a system to an electrical stimulation Bard and Faulkner 2000. In most electrochemical methods, a three-electrode setup is required: reference electrode (RE), counter electrode (CE) and working electrodes (WE). The reference electrode measures and controls the working electrode voltage to stabilize the solution potential. The counter electrode allows current to pass balancing the current through the working electrode. The three-electrode setup is connected to a potentiostat, an instrument which provides the applied potential and measures the response current.

Electrochemical methods can be divided in four categories: potentiometry (the potential is measured versus time), amperometry (the current is measured at a constant applied potential), voltammetry (the current is measured while a predetermined potential is applied), and impedimetry (the impedance of a system is measured with small sinusoidal waveform perturbations). This chapter mainly discusses three commonly used electrochemical methods: cyclic voltammetry, electrochemical impedance spectroscopy, and square wave voltammetry.

2.1 Cyclic Voltammetry

In 1938, cyclic voltammetry (CV) was first reported and theoretically discussed by Randles Randles 1948. CV investigates the kinetics of electrochemical reactions which take place at the electrode surface. The reactions proceed through two different

processes, i.e. Faradaic and non-Faradaic. A Faradaic process arises from the transfer of electrons across the metal electrolyte interface while a non-Faradaic process involves electrical double layer charging of the interface with no electron transfer. The electrochemical reaction occurring at electrode in the solution can be written as:

$$Ox + ne^{-} \Leftrightarrow Re \tag{2.1}$$

where Ox and Re are oxidized and reduced species, respectively Nicholson and Shain 1964. The two-arrow sign $\Leftrightarrow$ denotes that the reaction rate in the forward direction is equal to that in the reverse direction.

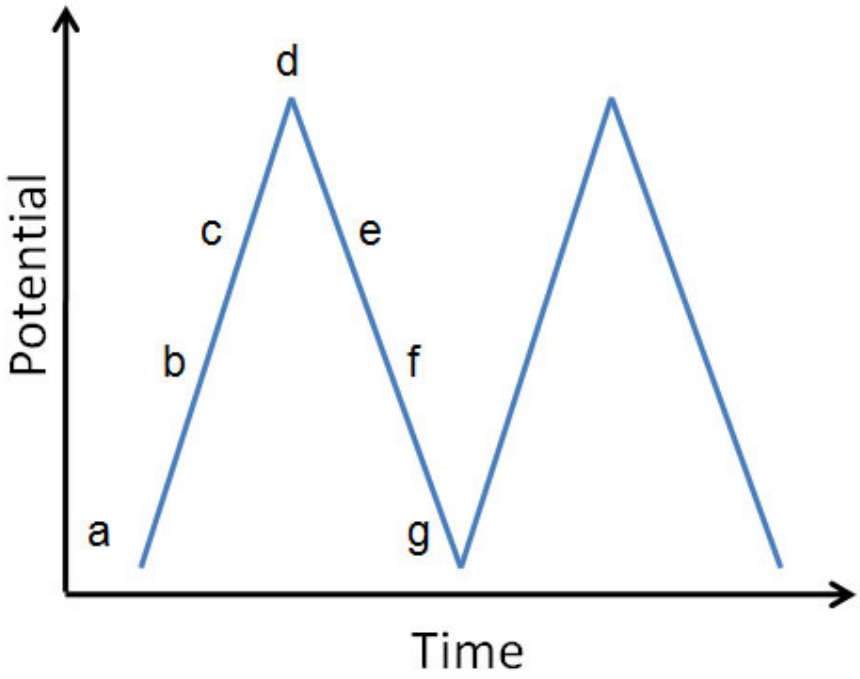

Figure 1. CV potential waveform

In Fig. 1, the electrode potential scans linearly versus time from a to d until it reaches a set potential called the switching potential, which leads to an oxidation of

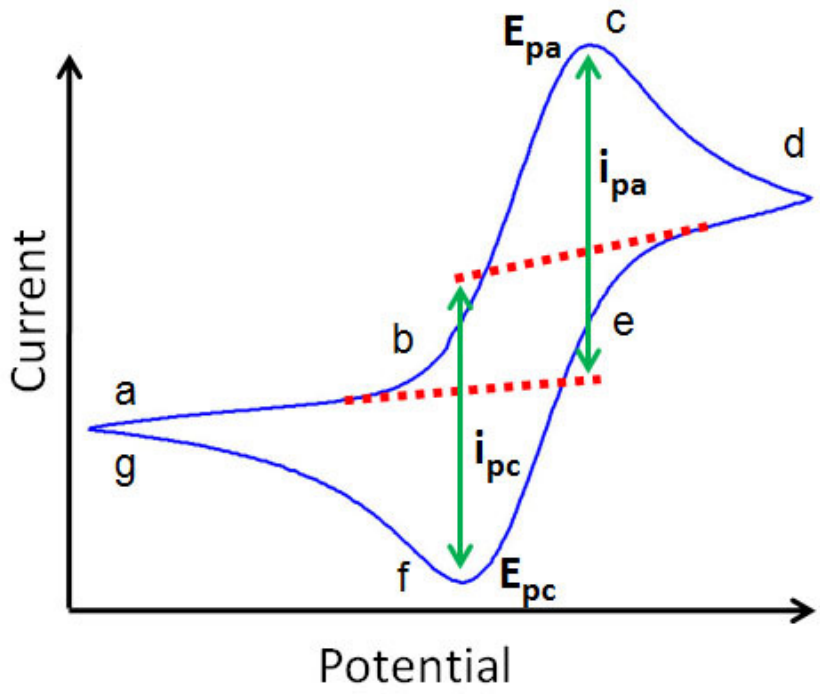

Figure 2. Cyclic voltammogram

the chemical species. Subsequently, the scan direction is inverted from d to g, and the scan repeats multiple times during an experiment. Fig. 1 demonstrates that from a low potential (initial potential) to a high potential (switching potential), the oxidation process happens and generates a current peak for the analyte. The resulting current is called anodic current (i_{pa}). The current first increases until the potential arrives at the oxidation potential, which is called the anodic peak potential (E_{pa}). Then it decreases as the oxidized chemical species is depleted in the vicinity of electrode surface. After the switching potential, the scan direction of the applied potential is reversed. This will produce an reduction peak (cathodic current i_{pc} and cathodic peak potential E_{pc}) which has a similar shape to the oxidation peak. Thus the redox potential and electrochemical reaction rates are recorded. The current peak i_p depends on both the

concentration C and the scan rate v according to the Randles–Sevcik equation Wang 2006.

2.2 Electrochemical Impedance Spectroscopy

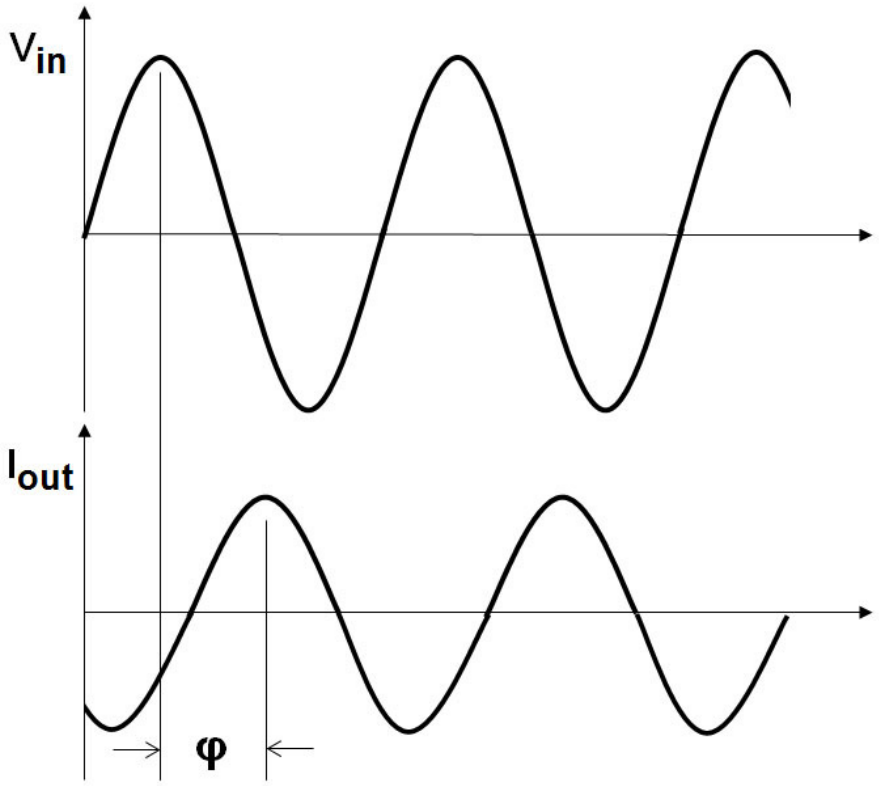

Figure 3. EIS current response in a linear system

Electrochemical impedance spectroscopy (EIS) is a method of measuring impedance of a system as a function of frequency Bard and Faulkner 2000; Barsoukov and Macdonald 2005. In traditional EIS, electrochemical impedance is usually measured by applying a small-amplitude sinusoidal signal to an electrochemical cell and record

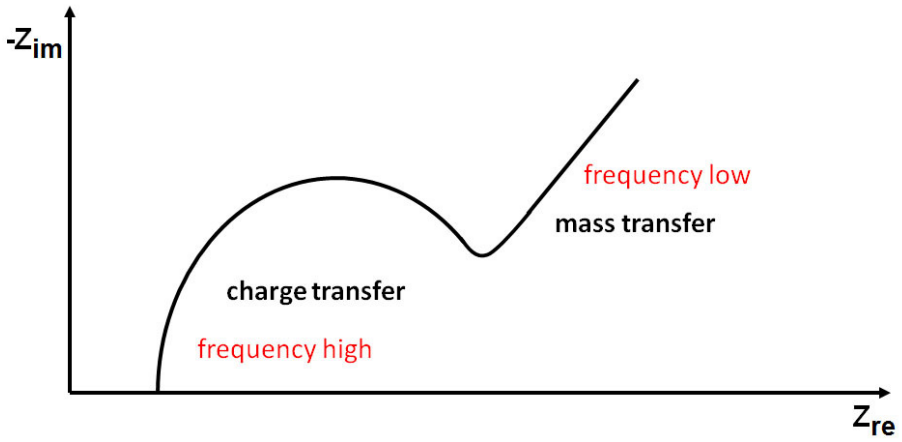

Figure 4. Impedance plot for an electrochemical cell

the response current through this system. When the excitation AC signal is small, the electrochemical cell's response is linear (or pseudo-linear). The response output to a sinusoidal input will be sinusoidal with the same frequency and a phase shift φ (see Fig. 3). The impedance of the electrochemical cell is calculated by:

$$Z = \frac{V_{in}}{I_{out}} =\mid Z \mid e^{j\varphi} = Z_{re} + jZ_{im} \tag{2.2}$$

where Z is the impedance of the system, V_{in} is the input potential, I_{out} is the response current, j is the imaginary unit, and Z_{re} and Z_{im} are the real part and imaginary part of Z. A typical Nyquist plot of EIS is illustrated in Fig. 4. The x-axis denotes Z_{re}, and the y-axis denotes the negative value of Z_{im}. On this plot, the frequency decreases from the left side to the right side. It is observed that charge-transfer and mass-transfer regions are located at low and high frequencies, respectively.

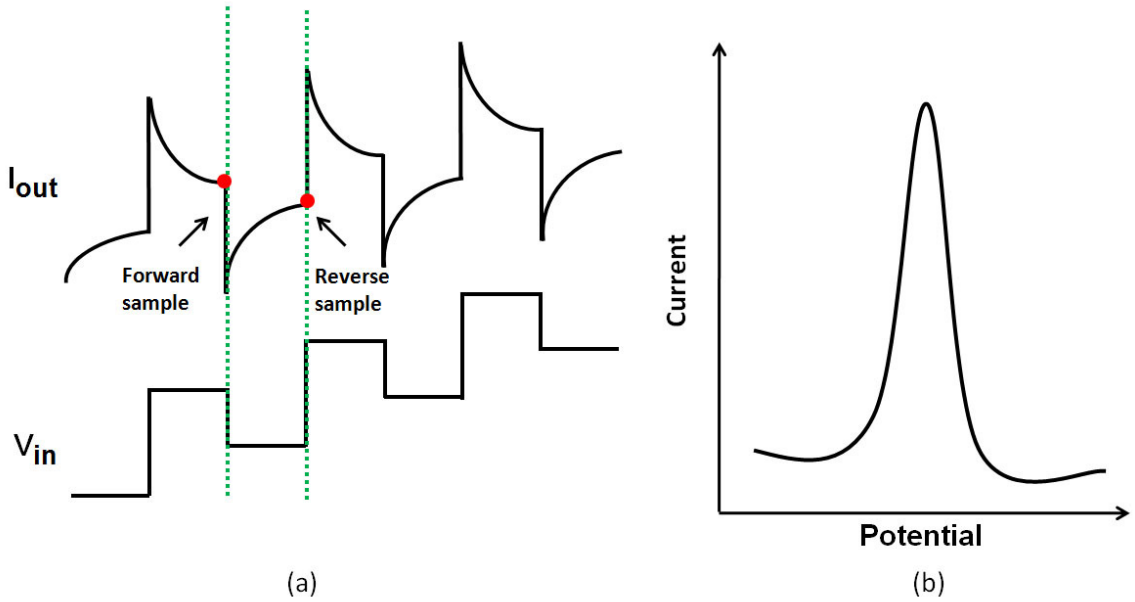

Figure 5. Principle of square-wave voltammetry. (a) Potential waveform V_{in} and the current response I_{out}. (b) A typical voltammogram in square-wave voltammetry.

2.3 Square Wave Voltammetry

Square-wave voltammetry (SWV) has seen tremendous advancements in recent years Chen and Shah 2013; Mirceski et al. 2013; Mirceski, Komorsky-Lovric, and Lovric 2007. This method stems from the Kalousek commutator Ruzic 1972 and Barker's square-wave polarography Barker and Gardner 1992. Because SWV combines the advantages of pulse techniques (high sensitivity), cyclic voltammetry (investigation of the electrokinetic), and impedance methods (analytic measurements), it is now one of the primary voltammetric techniques. The potential waveform V_{in} used in SWV can be considered as a superposition of a square wave onto a staircase potential ramp as seen in Fig. 5 (a). For each step of the staircase potential, two equal magnitude and duration but opposite in direction square pulses are applied. These two square

pulses are the forward pulse and the reverse pulse. The response current is sampled twice; one at the end of the forward pulse and again at the end of the reverse pulse. It should be noted that the current is sampled immediately before the potential direction is changed. Therefore, the contribution to the response current resulting from non-faradaic current is minimal. The current difference is obtain by subtracting the reverse current from the forward current. Subsequently, a curve is plotted against the staircase potential in Fig. 5 (b). The peak in the voltammogram appears as a result of redox processes. The magnitudes of the current peak is proportional to the concentration of the redox species Bard and Faulkner 2000; Mirceski et al. 2013.

Chapter 3

CYCLIC VOLTAMMETRY MEASUREMENTS

This chapter presents a CMOS potentiostat chip fabricated in a standard 0.5 μm CMOS process to perform electrochemical analysis via cyclic voltammetry Luo et al. 2013. This chip contains six independent channels for three electrode systems in electrochemical cells. Our low power circuit has been designed to drive electrochemical reactions in the solution using a class AB folded cascode amplifiers. The circuit operates with rail to rail input and output and strong drive ability. We have shown the potentiostat chip is capable of performing cyclic voltammetry (CV) with both potassium ferricyanide and hexaammineruthenium chloride solutions. The chip is capable of differentiating both the composition and concentration of the solution. We compare our results with control experiments on a Gamry commercial electrochemical workstation and demonstrate they are consistent.

3.1 Background

The detection of analyte composition and concentration in solution is essential for many applications in industrial control Freitas et al. 2012, environmental engineering Strycharz et al. 2011 and medical diagnosis Fairchild et al. 2009; La Belle et al. 2011. These applications can benefit from development of low cost, portable, robust devices that are simple to use Y. Huang et al. 2013. Many new methods have been developed for analysis including optical Warren-Smith et al. 2011, magnetic Hua Wang et al. 2009 and electrochemical Mason et al. 2007 analysis. To obtain direct

transduction of electrical signals and reduce interface noise electrochemical techniques have become an important and widely used Cao, Greve, and Oppenheim 2008; Li et al. 2011. In addition these electrochemical systems are fabricated in standard CMOS processes Mason et al. 2007; Cao, Greve, and Oppenheim 2008; Li et al. 2011, improving reliability and reducing not only the cost and reliability but the necessary sample volume as well. The use of a CMOS process also allows for the integration of state-of-the art circuits in the sensor substrate, providing a feasible pathway to handheld sensor platforms.

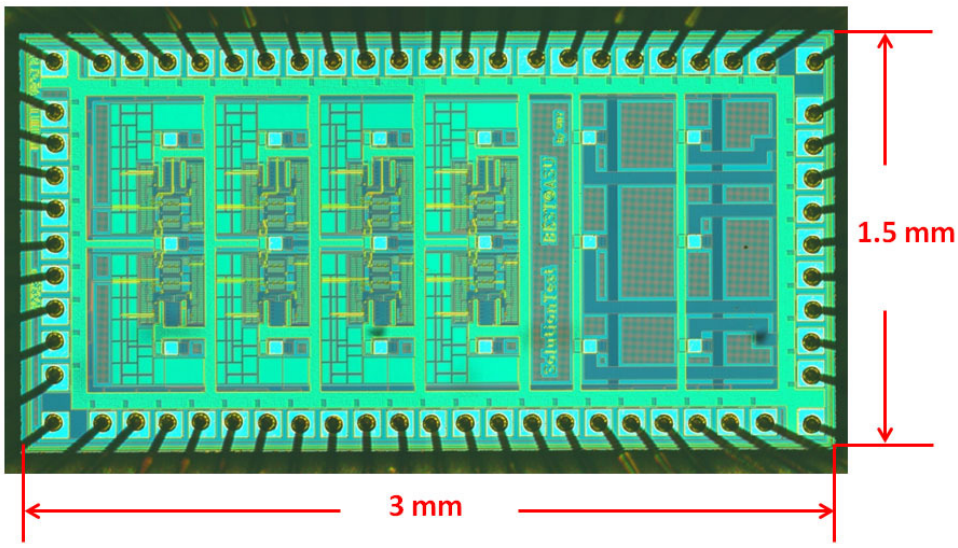

Figure 6. Optical micrograph of the 1.5 mm × 3 mm die. This potentiostat chip was fabricated in a standard CMOS process with six independent channels.

We describe a CMOS potentiostat chip shown in figure 6 that is used to preform cyclic voltammetry to detect the aforementioned peak current for analyte analysis in section 3.2. The chip was demonstrated by performing CV experiments with potassium ferricyanide (Sigma-Aldrich, product no. 702587) solution using screen printed carbon electrodes with a three electrode configuration (CH Instruments Inc.,

Part number TE100), described in section 3.3. Both the CMOS chip and a commercial electrochemical workstation (Gamry Instruments Inc., Reference 3000^{TM}) were used to run CV on various potassium ferricyanide concentrations and scan rates demonstrated in section 3.4. These experiments were conducted to illustrate the effect of scan rate and concentration on the peak current. We also use a different chemical species, hexaammineruthenium chloride (Sigma-Aldrich, product no. 262005), to find the change in the redox peak position to demonstrate identification of different species in section 3.5. In addition three external gold electrodes were used in the potassium ferricyanide solution for CV experiments in section 3.6. Finally the results are discussed in section 3.7.

3.2 System Overview

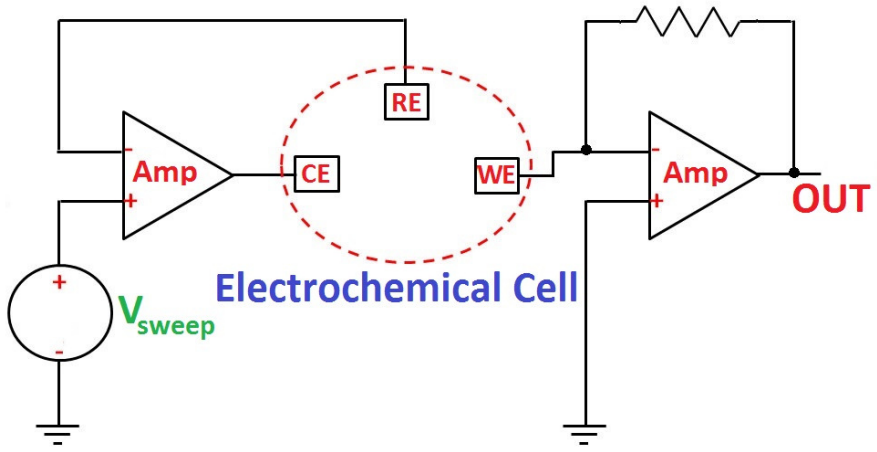

Figure 7. Single channel potentiostat schematic for CV measurements. The two amplifiers are on-chip and the voltage supplies, electrochemical cell and feedback resistor are external.

The 1.5 mm $\times$ 3 mm potentiostat chip was fabricated in a standard 0.5 μm CMOS process and is shown in Fig.6. This CMOS circuit was designed with the help of Dr. Hongyi Wang. The chip consists of six independent potentiostat circuits. The basic schematic for each of those six channels each used to perform CV is shown in figure 7. To conduct electrochemical experiments including cyclic voltammetry Yang, Huang, et al. 2009 and impedance spectroscopy Yang, Jadhav, et al. 2009, a three-electrode setup is required with reference electrode (RE), counter electrode (CE) and working electrodes (WE). In CV, the electrode potential scans linearly with time until it reaches a set potential called the switching potential. After reaching the switching potential, the scan direction is reversed until it reaches the initial potential, then the scan is repeated multiple times. When the scan potential moves from a high potential (initial potential) to a low potential (switching potential), reduction occurs and generates the current peak for the analyte, i_p. The current first increases until the potential arrives at the reduction potential then decreases since the reduced species becomes depleted near the electrode surface. At this point the scan direction for the applied potential is reversed. This produces an oxidation peak which has a similar shape to the reduction peak but is inverted. This allows us to determine the redox potential and electrochemical reaction rates. The peak current i_p depends on both the concentration and scan rate, according to the Randles-Sevcik equation Wang 2006. If the solution is at 25 °C, the equation is described as:

$$i_p = 2.69 \times 10^5 n^{3/2} A D^{1/2} v^{1/2} C \tag{3.1}$$

where n is the number of electrons transferred in the redox reaction, A is the electrode area, D is the diffusion coefficient, v is the scan rate, and C is the concentration. We use the setup in figure 7 to perform these measurements; it is implemented with

integrated amplifiers and external voltage supplies, electrochemical cell and feedback resistor.

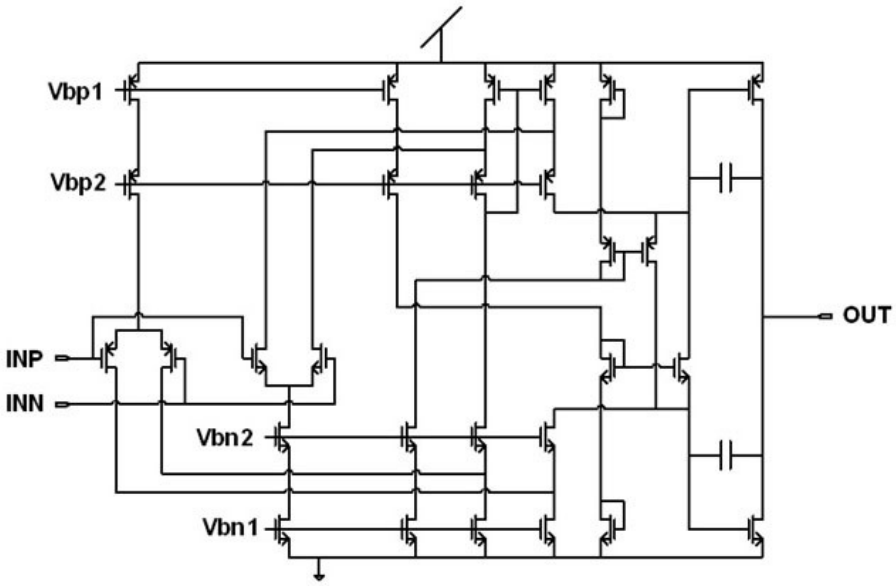

Figure 8. Class AB folded cascode amplifier schematic for the potentiostat circuit.

These CMOS potentiostat circuits were designed to achieve both low power and strong drive capability. The amplifiers used are class AB folded cascode amplifiers with the schematic shown in Fig.8. We have completely characterized the fabricated chip and tested the performance of the amplifiers. This low power design has a quiescent current of 44 μA and can be operated with a supply voltage from 5 V down to 2 V. The input and output range of the system is rail to rail and the gain is 105 dB with a phase margin of 78 degrees. The system was design for low frequency operation matched to our application and to minimize high frequency noise with a 0 dB bandwidth of 30 kHz. The PSRR is 70 dB, and the transconductance is 21 A/V. The system can drive over 10 mA, source or sink.

3.3 Potassium Ferricyanide CV Measurement by CMOS Potentiostat and Gamry

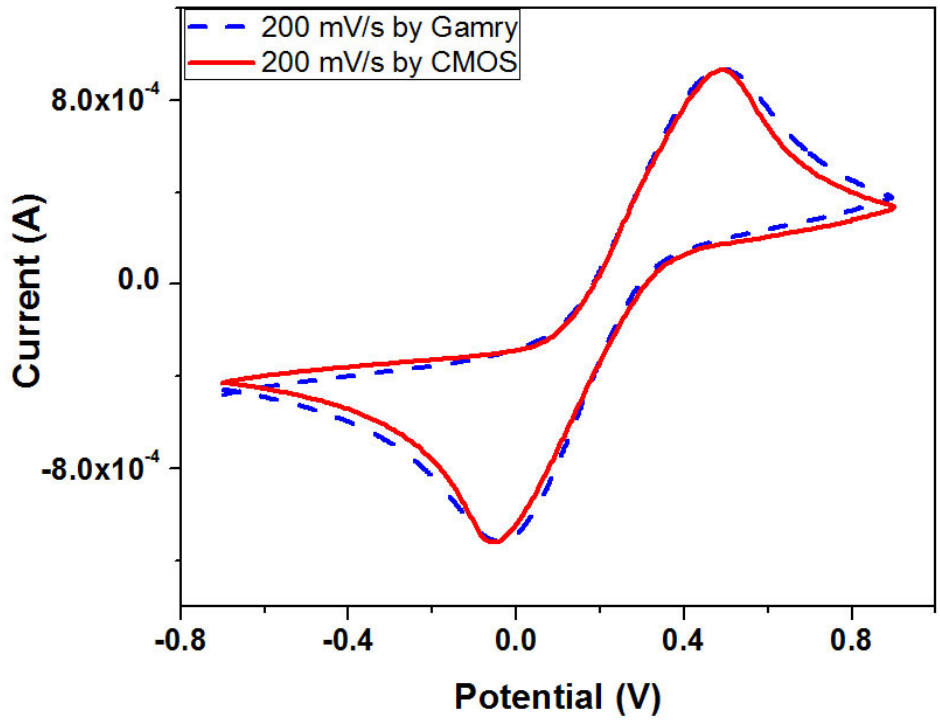

Figure 9. CV measurements of 100 mM potassium ferricyanide by our CMOS potentiostat chip and the Gamry workstation.

Potassium Ferricyanide is a standard in calibration and measurements for electrochemistry, thus it was chosen to demonstrate our system. A typical electrolyte solution with 1 M potassium chloride (EMD Chemicals, product no. PX1405-1) and 100 mM potassium ferricyanide was used to verify the operation of our chip. The cyclic voltammetry measurements were performed with an external electrochemical cell using the screen printed carbon three electrode strips that have a Ag/AgCl RE and carbon CE and WE. The experiment setup included a BK precision 1761 DC power supply and a two channel Keithley 2636A System Source Meter. To verify the

CMOS potentiostat performance, the results from the CMOS chip and Gamry are compared. We used a 200 mV/s scan rate for this experiment. The plot in Fig.9 shows agreement between the two voltammograms with both the magnitude and potential for the oxidation and reduction peaks being the key values indicative of this agreement.

3.4 The Effect of Concentration and Scan Rate

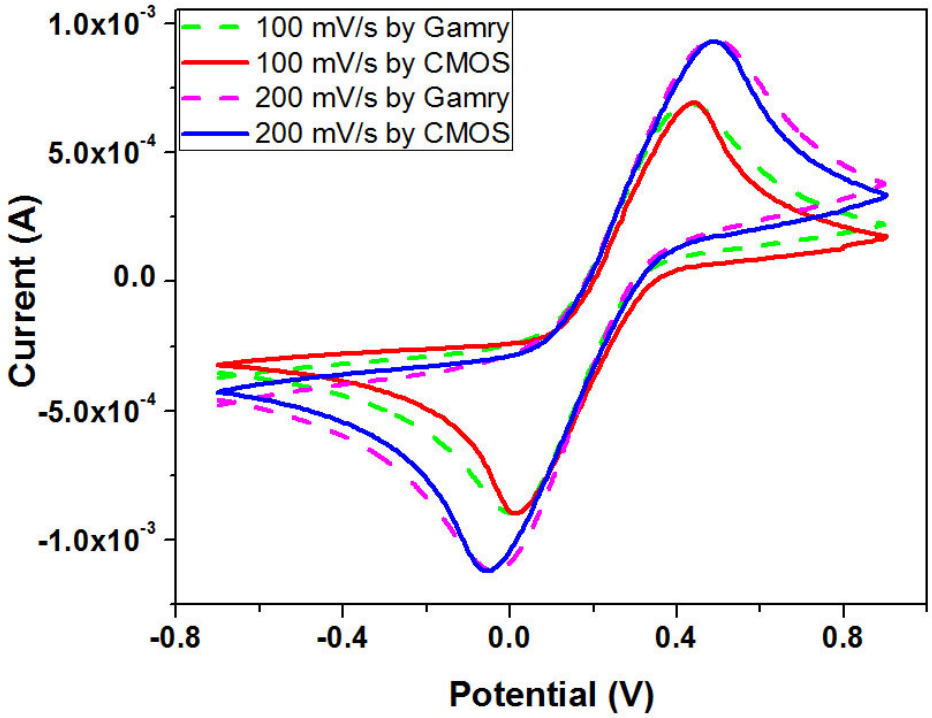

Figure 10. CV measurements of 100 mM potassium ferricyanide at different scan rates for both the Gamry and our CMOS potentiostat chip.

It is well know that from equation 3.1, the peak current depends not only on the concentration of the redox species but on scan rate as well. Therefore we have performed tests to demonstrate the effects of scan rate on CV for potassium ferricyanide for our chip and the commercial Gamry system. In Fig.10 the blue and red voltammograms show measurements with our chip at 100 mV/s and 200 mV/s scan

rate for the solution of 1 M potassium chloride and 100 mM potassium ferricyanide. We have also investigated the effects of concentration on the CV measurement. Fig.11 shows the voltammograms for different concentration at a 100 mV/s scan rate. The blue and red voltammograms represent 100 mM and 50 mM potassium ferricyanide, respectively both 1 M potassium chloride. All measurements were performed with the carbon electrodes by both the CMOS chip and Gamry. As expected, peak currents are dependent on redox concentrations and scan speeds and show good agreement between our chip and the commercial system.

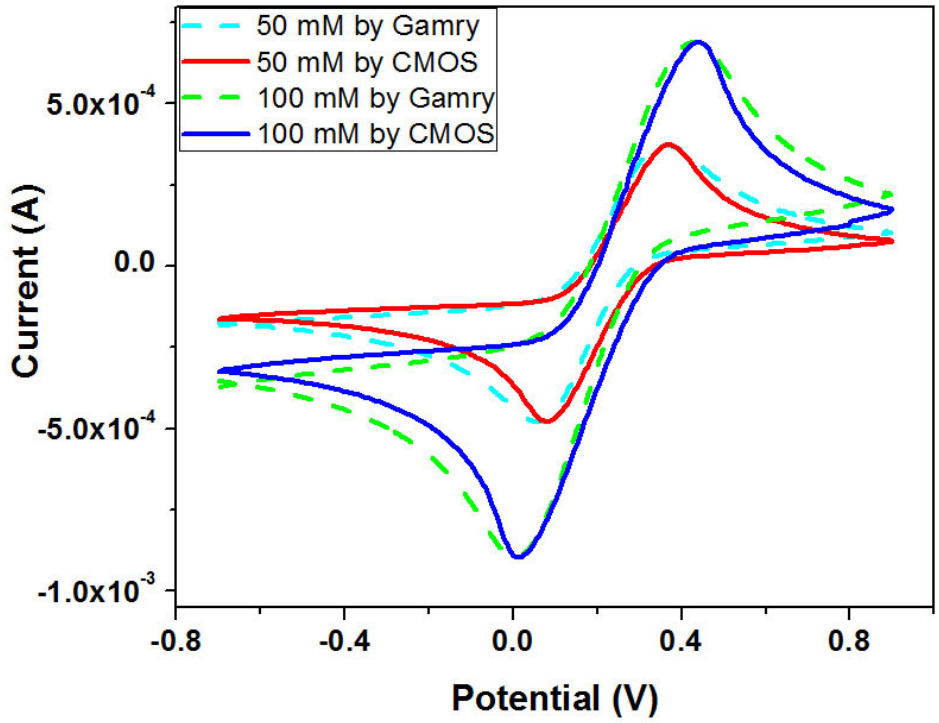

Figure 11. CV measurements for the different concentrations of potassium ferricyanide on our CMOS potentiostat chip and the Gamry.

3.5 Hexaammineruthenium Chloride CV Measurement by CMOS Potentiostat and Gamry Workstation

Thus far we have shown good agreement between our system and the commercial Gamry system as well as a match between our results and equation 3.1. We aim to show the system is also capable of distinguishing different chemical species. To this end we have performed CV with hexaammineruthenium chloride as the probe as shown in Fig.12. The potential scan was performed in solution of 1 M potassium chloride and 5 mM hexaammineruthenium chloride with a scan rate of 100 mV/s. The external screen printed carbon electrode in the three electrode configuration were used for the CV, and the voltammogram shows the measurements by CMOS chip are in agreement with measurements made using the Gamry. The measurement also shows a significant shift in the oxidation and reduction peaks relative to the measurements for potassium ferricyanide indicative of different chemical species.

3.6 Potassium Ferricyanide CV Measurement with Three External Gold Electrodes

In the future we will use integrated Au electrodes on our CMOS chip to perform CV measurements. To this end we have designed the chip with internal electrodes as can be seen in figure 6. We have chosen gold electrodes, since the integration of more preferable materials such as silver/silver chloride or platinum can not be accomplished with our thermal evaporator system. Since the change in the electrode material will cause a shift in the voltammogram, we utilize three external gold electrodes and repeat the CV measurements. From the plot of the results in Fig.14 we demonstrate the CV can be performed with gold electrodes. The electrochemical cell was implemented

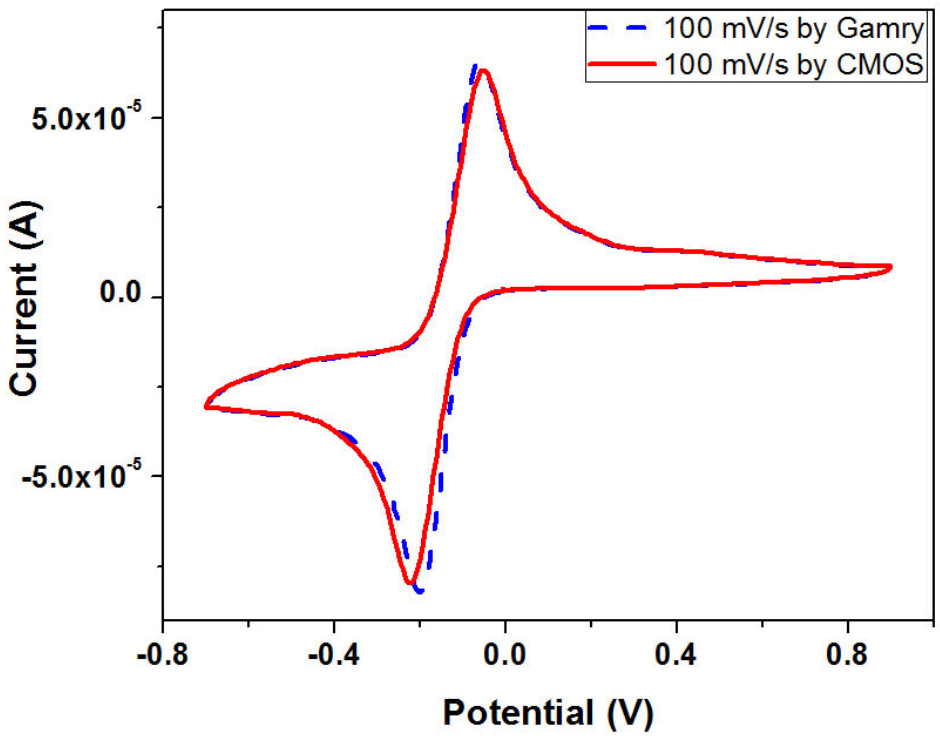

Figure 12. CV measurements of 5 mM hexaammineruthenium chloride by our CMOS potentiostat chip and the Gamry workstation.

in a cuvette with three external gold electrodes. We used 0.2 M potassium chloride and 20 mM potassium ferricyanide. Fig.13 shows results from both Gamry and the CMOS system are consistent. As expected the difference in electrode materials caused a shift in the voltammogram measured with Au electrodes relative to the previous measurements that were performed with the screen printed carbon electrodes.

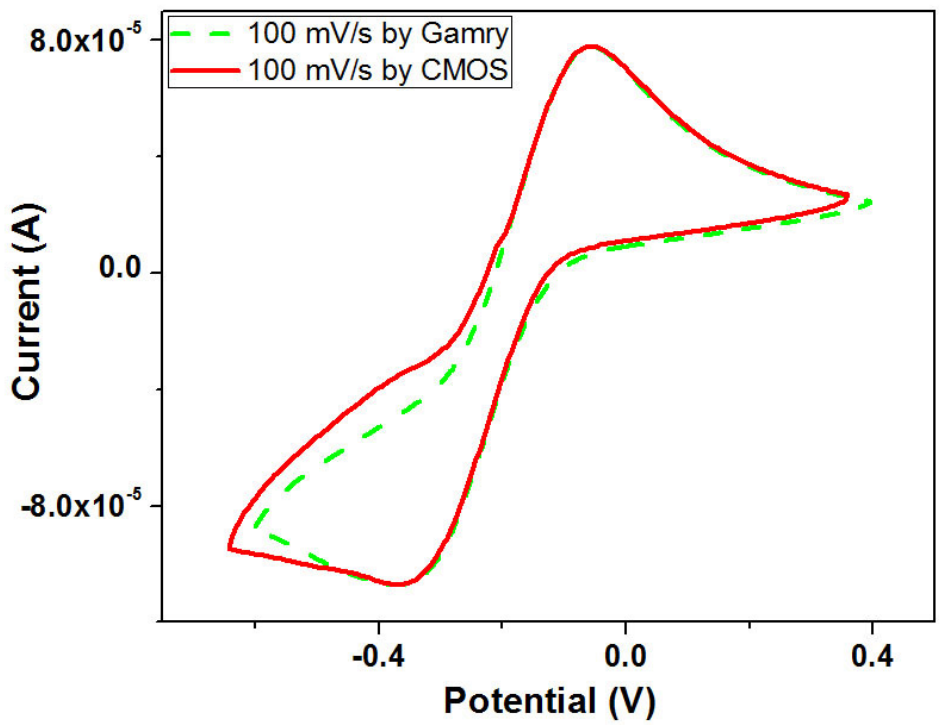

Figure 13. CV measurement of potassium ferricyanide with three external gold electrodes on the Gamry workstation and our CMOS potentiostat chip.

3.7 Conclusion

In this chapter, a CMOS potentiostat chip for electrochemical sensing application is presented. The chip was fabricated in a standard 0.5 μm CMOS process with six independent potentiostat circuits and integrated electrodes. The class AB folded cascode amplifier was fully characterized as described in section 3.2 and can be used to drive electrochemical reaction in the analyte solution. We have shown the potentiostat is capable of performing CV measurements under various conditions including varying sweep rates and concentrations. We have also shown the system can distinguish between potassium ferricyanide and hexaammineruthenium chloride. Further we have demonstrated the system works well using both screen printed carbon electrodes and

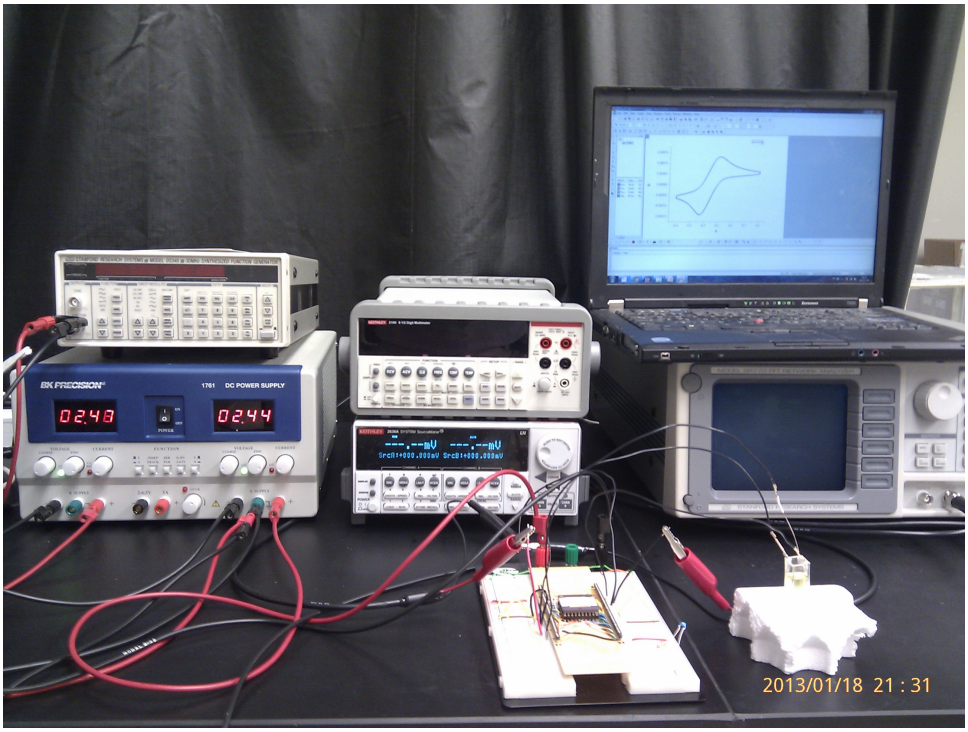

Figure 14. Photograph of experimental setup with three external gold electrodes

gold electrodes. All these test are performed with the reported CMOS potentiostat chip and the commercial Gamry electrochemical workstation, and the results verify the robust functionality of the CMOS system and agreement with the commercial standard.

Chapter 4

CMOS ELECTROCHEMICAL SENSOR AND PACKAGING

This chapter reports an integrated CMOS electrochemical sensor with on-chip electrodes and packaging Luo et al. 2014. The CMOS chip was fabricated in a standard 0.5 μm CMOS process, and it contains potentiostat circuits with integrated array of three electrode cells. This CMOS circuit was designed in collaboration with Dr. Hongyi Wang. In the potentiostat circuit, we designed high performance folded cascode class-AB operational amplifiers with rail to rail input and output suitable for low power consumption and strong drive capability. The 1.5 mm $\times$ 3 mm potentiostat array chip operates from a 5 V supply at 45 μA. A gold electrode array was made on the surface of the CMOS chip using a contact photolithographic process. For compatibility with liquid test environments a packaging approach was developed. The electrochemical sensor with on-chip electrodes was characterized by using cyclic voltammetry (CV) with potassium ferricyanide.

4.1 Background

Due to the significant advances of CMOS technology in the past decades, it is a well-established technology with a wealth of design techniques thoroughly investigated. This has lead to the application of CMOS technology to fields outside of traditional electronics including molecular sensing. Great effort has been made to miniaturize and integrate analytical instruments for chemical applications. These CMOS-based instruments include optical Lehmann et al. 2008, magnetic H. Lee et al. 2007 and

electrochemical Li et al. 2011 sensors. We are particularly interested in electrochemical sensors, since we can implement these in CMOS without any additional components such as lenses or filters. Electrochemical techniques allow for direct transduction of chemical information to electrical signals Li et al. 2011; Cao, Greve, and Oppenheim 2008, leading to the reduction of the interface noise. Moreover electrochemical sensors can be easily miniaturized by CMOS process Li et al. 2011; Cao, Greve, and Oppenheim 2008; Mason et al. 2007; Stanacevic et al. 2007; Hwang et al. 2009; Nazari et al. 2013; Manickam et al. 2010, which makes the detection systems low power, low cost, highly accurate, portable and low volume. CMOS implementation allows us to realize the analysis and readout circuit in the same substrate. However, in these applications, devices need to directly contact the solutions being tested. This requires some isolation of the reactive metals from the analyte solution. We demonstrate a simple technique to isolate the aqueous solution to achieve an integrated fluid-environment sensor interfaces. This system demonstrates all the advantages that make CMOS well-suited for lab-on-chip platforms.

While we can design circuits to accommodate the aforementioned electrochemical experimental techniques, there is a major challenge in the fluid environment for lab-on-chip CMOS sensors. Electrochemical microsystems need direct contact between liquid and electrodes for either voltammetry or impedance spectroscopy. It is well known that aluminum (Al) and copper (Cu) are the most common materials used for metal layers in CMOS fabrication. According to the standard 0.5 μm CMOS process used in this work, the bonding pads and integrated electrodes on the CMOS chip, i.e. the exposure area of top metal layer, are made of Al. However because of the oxidizing property of the solutions, Al and Cu cannot be utilized as a durable conductive electrode in the liquid environment. Moreover, the stable reference electrode needed to complete the

electrochemical cell can't be composed of such easily oxidized materials. To improve the performance and the sensitivity, the sensing electrodes can be post-processed to coat the fabricated the top metal layer of CMOS chip with another material. Because Au is a stable noble metal and considered to be biocompatible Radke and Alocilja 2005, it is commonly used as sensing electrodes for electrochemical applications. It can also be used as a pseudo-reference electrode. While gold is not an ideal reference, it works quite well in most applications, and it is convenient to use a single metal for all three electrodes.

Another issue for the use of CMOS chip within the liquid environment is the wire bonding technique utilized by industry-standard packages, resulting in exposure of wires to solution samples. In order to seal wires and create fluidic reservoirs, parylene-C is often used as the encapsulation material Prodromakis et al. 2009. But is is difficult to control the laser to ablate the parylene during patterning. And the ultrasonic bath could damage the sealing around the wire bonds. Another parylene packaging method was developed by Li et al Li et al. 2011. However their complicate method needs 300 W RF power RIE, which could damage the desired electrode surface, and is still lacks an accurate alignment method during patterning and etching of the parylene. We describe a simple methods for packaging that doesn't require sophisticated equipment or techniques to isolate the aqueous solutions from the galvanic connections.

In this paper, we report a CMOS based electrochemical microsystem with low power consumption and strong drive capability. We describe the integrated electrochemical system in section 4.2. Then the post-CMOS electrode microfabrication and packaging are presented in section 4.3. Finally, the measurement results are discuss in section 4.4.

4.2 System Overview

4.2.1 CMOS Potentiostat Structure

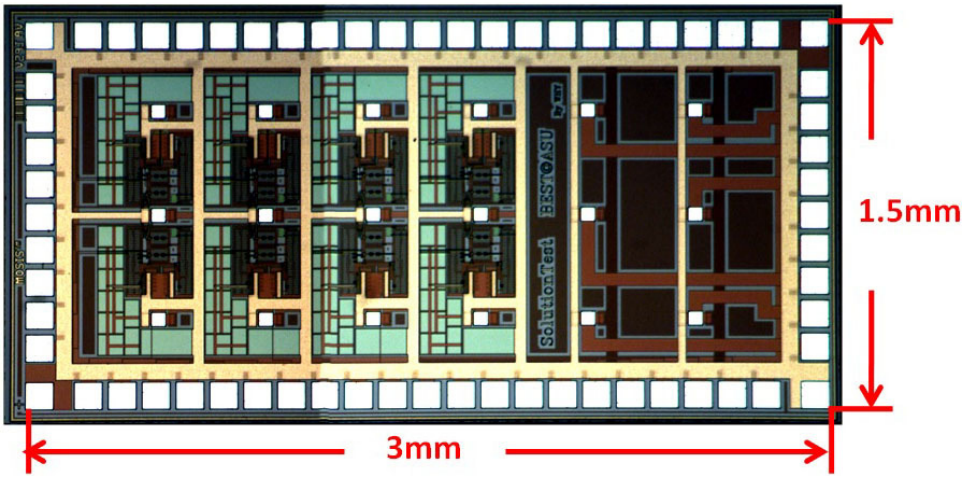

Figure 15. Photograph of the 1.5 mm × 3 mm potentiostat chip fabricated in a standard 0.5 μm CMOS process with six independent channels having integrated three electrode electrochemical cells. The chips is shown prior to post-processing.

Fig. 15 shows the potentiostat chip, which is fabricated in a standard 0.5 μm CMOS process and consists of six potentiostat channels with each channel having three integrated electrodes: RE, CE, and WE. A circuit is design to function as the potentiostat for the electrochemical cell. The amplifiers for the potentiostat are designed to be low power for portable applications but retain accuracy. In order to measure various impedances of different analyte concentrations, amplifiers are capable of supporting widely varying load properties. The amplifiers must also have sufficient ability to drive the electrochemical cells, which have complex impedance characteristics. A class AB folded-cascode amplifier was designed to meet these requirements. The specifications of the CMOS amplifier has been presented previously Luo et al. 2013.

For bioelectrochemical applications, the stimulus frequency is low, i.e. less than 100 Hz. The dc gain and the bandwidth of our amplifier are sufficient to operate the sensors accurately for detection of biological molecules, our target application.

4.2.2 Experimental Setup

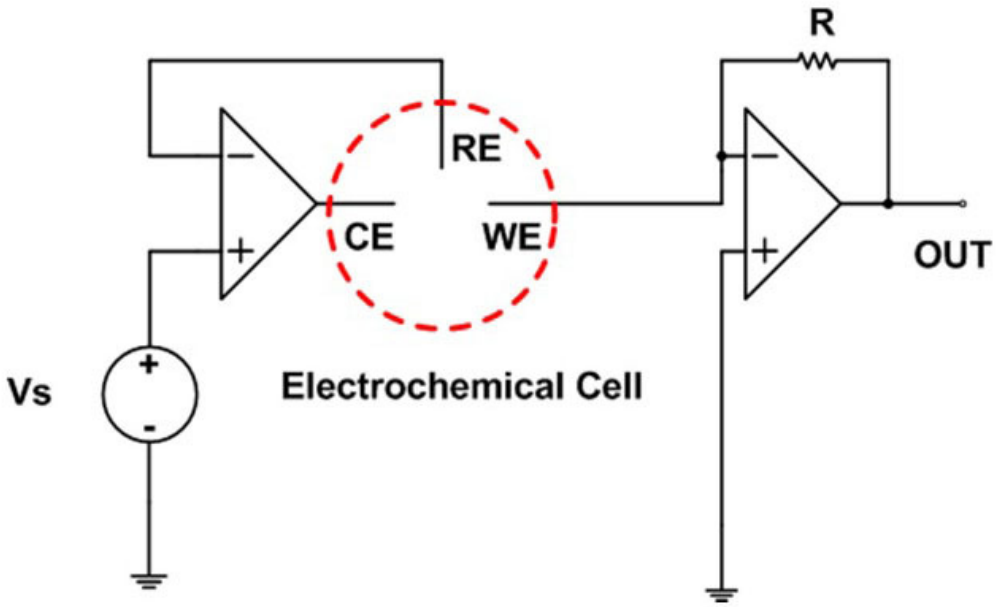

Figure 16. Single channel potentiostat schematic for CV measurements.

A typical potentiostat circuit used in an electrochemical experimental setup is shown in Fig. 16. This could be operated in voltammetry mode by sweeping Vs or impedance spectroscopy mode by applying a sinusoidal voltage instead. To characterize the chip performance of the on-chip electrochemical sensor, we operated the chip

in cyclic voltammetry (CV) mode. The experimental setup includes the integrated electrochemical system, which has the potentiostat circuit, the electrochemical cell, and a feedback resistor. In addition we used a BK precision 1761 DC power supply and a two channel Keithley 2636A System Source Meter for measurements. The power supply was used to power the chip and provide biasing while the Keithley was used to cycle the input voltage and measure the output of the potentiostat.

4.3 Post-CMOS Electrode and Packaging

4.3.1 Die-Level Fabrication

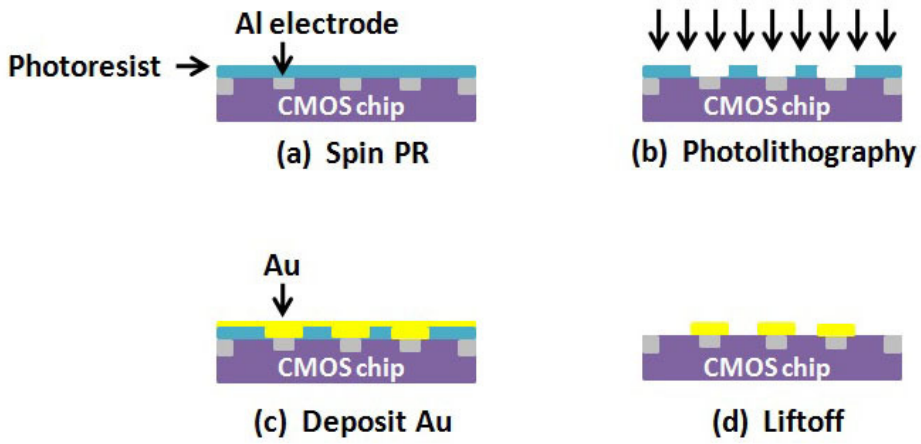

Figure 17. Process for post-CMOS electrode fabrication to both add a chrome/gold layer to the surface and increase the electrode surface area.

In standard CMOS processes the material used for electrical contacts and interconnections is Al or Cu, which can be easily oxidized by chemical solutions. To establish

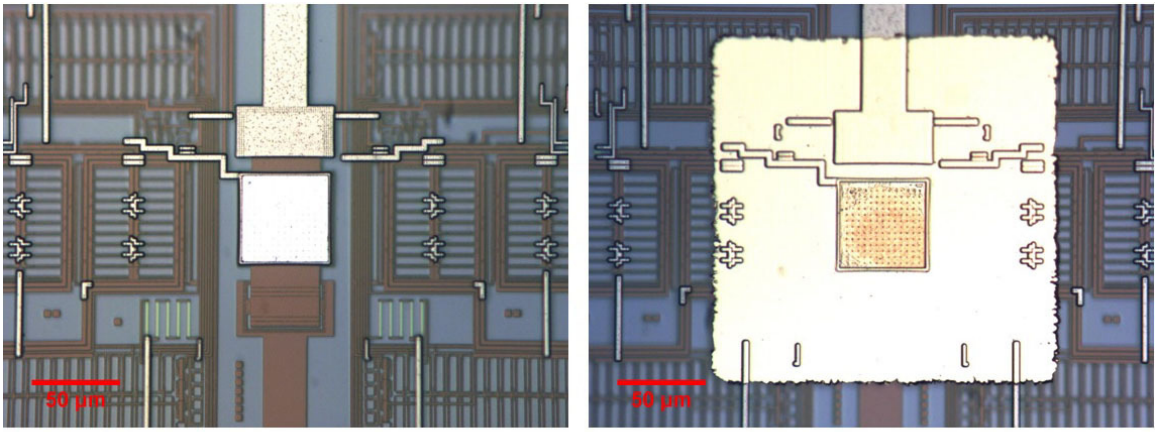

(a) Before Au electrode fabrication (b) After Au electrode fabrication

Figure 18. Electrodes are initially designed similarly to bond pads, and they are coated with gold for operation in aqueous solutions. A single electrode is shown in detail before (a) and after (b) Cr/Au patterning, deposition, and lift-off. The red scale bar on the images for reference is 50 μm.

a durable microelectrode array, a noble metal, Au in this case, can be employed as sensing electrode. We chose Au since it is considered to be biocompatible and relatively quite inert. Au layer can easily be deposit at low temperature with a chrome adhesion layer and patterned by using standard photolithography techniques.

The Fig. 17 illustrates our die level post-CMOS fabrication process. The S1813 photoresist is spin coated on the 1.5 mm $\times$ 3 mm CMOS chip at 3000 rpm for 30 seconds. Subsequently the chip is baked on a hotplate at 115 °C for 60 seconds. Then photolithography is performed with an HTG mask aligner. The photoresist film is exposed for 10 seconds. After exposure the pattern is developed in a mixture of DI water and 351 developer with ratio of 5 to 1 for 40 seconds. The metal film is formed by thermal evaporation of Cr/Au (30 nm/100 nm) with a Cressington 308R evaporator. Finally a lift-off process is used in acetone with a Branson ultrasonic cleaner for 1-2 minutes. The Au electrode array is characterized under an optical microscope as demonstrated in Fig. 18.

4.3.2 Package-Level Fabrication

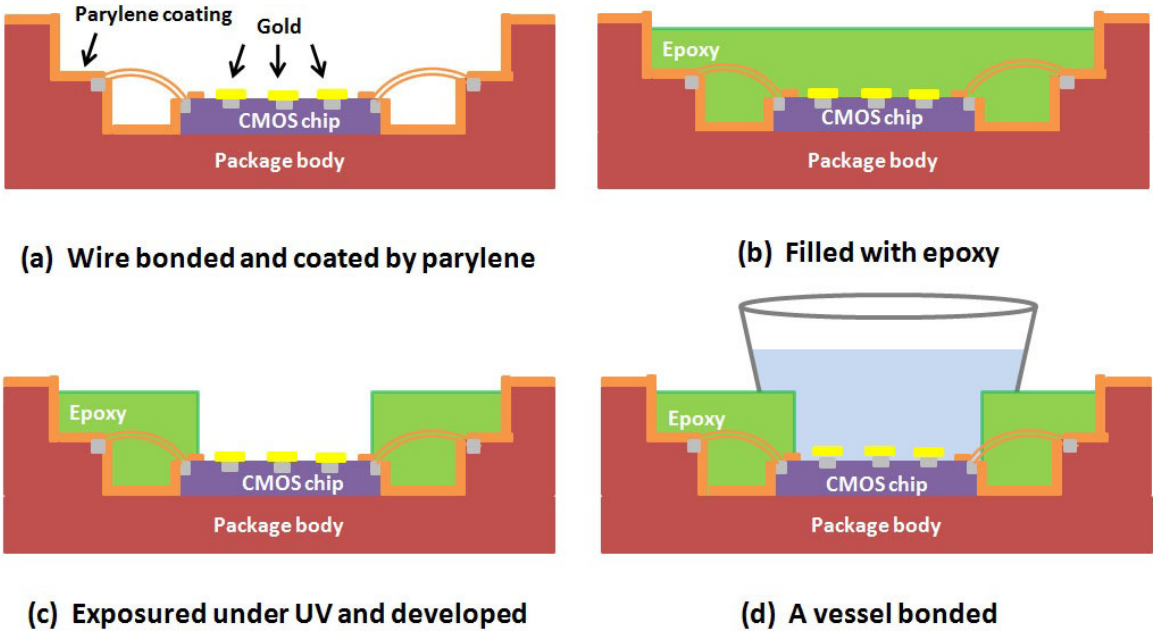

Figure 19. Fabrication process for the "chip in package" structure to hold the fluid volume for testing.

A packaging scheme was developed to allow the chip to operate in a liquid environment using a "chip in package" approach. Fig. 19 shows the package level fabrication process for this approach. The chip is wire bonded to a standard dual in line package (DIP), (Global Chip Materials, SB4840001). To protect Au electrode array, a drop of acrylic bonding compound is placed on the chip surface. Subsequently the packaged chip is conformally coated by a 3 μm thick layer of parylene C using the PDS 2010 LABCOTER 2 to seal electrical wires and prevent current leakage. Then the package cavity is filled with UV curing epoxy (Loctite 3335). Using a 1.4 mm $\times$ 2.8 mm Al foil mask the loctite 3335 is cured to form liquid reservoir on the chip

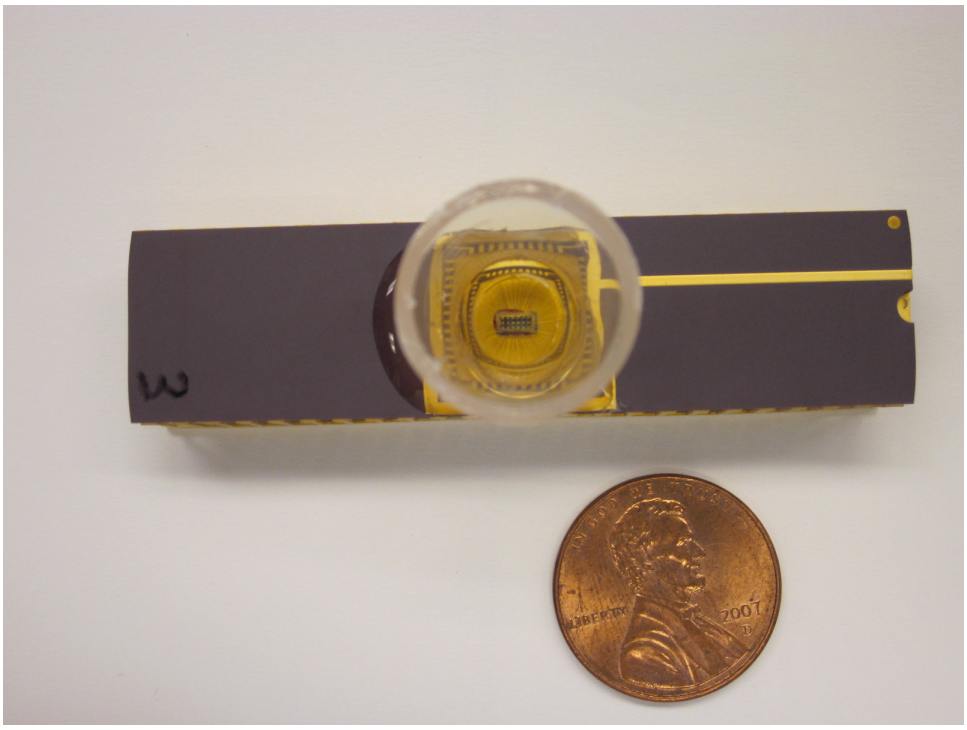

Figure 20. Photograph of final package chip from above. The top rim of the bonded vessel is visible as well as the surface of the CMOS die. The parylene C coating results in an excellent seal against moisture.

substrate under 365 nm UV light for 15 minutes. The uncured epoxy and the acrylic bonding compound are removed using acetone. Super glue is needed to bond a small vessel as a liquid reservoir to increase the volume. The final package results in an exposed Au electrode array with all other surfaces covered by parylene C. The final package with Au electrode array exposed and vessel bonded is shown in Fig. 20.

4.4 Results

CV experiments were chosen to verify the functionality of the on-chip electrochemical sensor. A typical electrolyte solution with 0.1 M potassium chloride (EMD

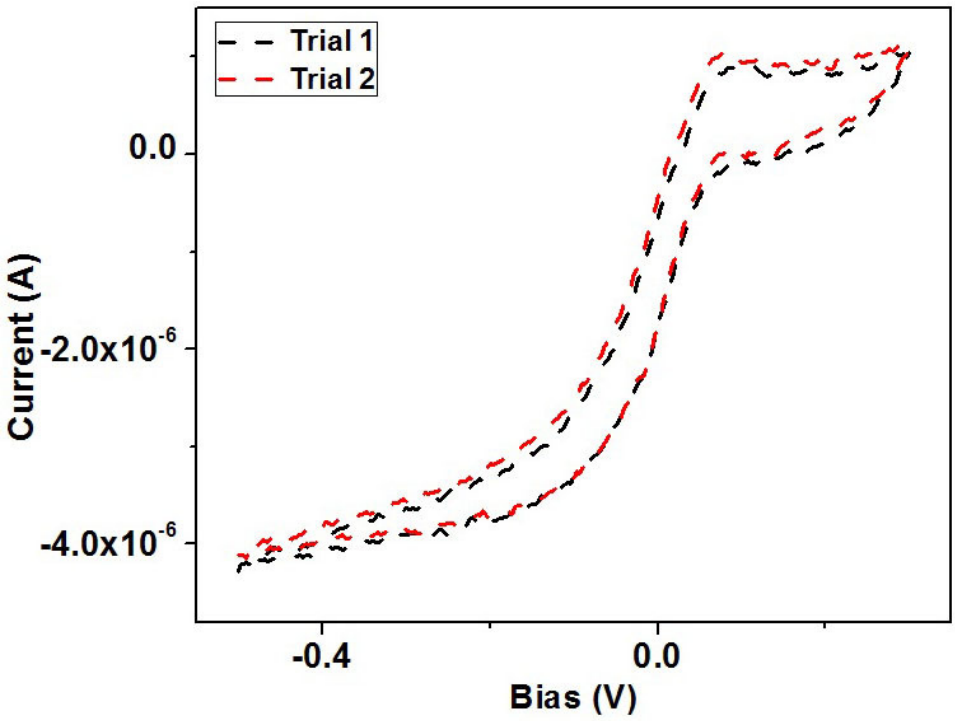

Figure 21. On-chip microelectrode CV measurements of the 0.1 M potassium chloride and 10 mM potassium ferricyanide solution with a sweep rate 188 mV/s.

Chemicals, product no. PX1405-1) and 10 mM potassium ferricyanide (Sigma-Aldrich, product no. 702587) was used as an analyte. The potential is swept at 188 mV/s, and the output is detected with Keithley 2636A source meter. The cyclic voltammogram shape differs from standard voltammograms due to the microscale integrated electrode array as illustrated in Fig. 21. The voltammogram matches well with other systems employing microelectrodes. The current is also quite low because of the smaller electrode area, and the current becomes a steady value without peak. One reason is that the integrated electrode is considered a dot with diffusion layer being hemispherical and extending into the solution Bard and Faulkner 2000. When the diffusion layer is much larger than the radius of electrode the diffusion to the electrode becomes

important. The current goes to a steady value and is proportional to the radius of the disk.

4.5 Conclusion

A CMOS electrochemical system with on-chip electrode array and packaging was demonstrated. The main advantage of this integrated systems is the simplicity of design and fabrication. This CMOS chip, fabricated in a standard 0.5 μm process, contains six independent potentiostat circuits suitable for low-power, portable chemical or molecular analysis applications. A die-level fabrication process was demonstrated to pattern integrated Au electrodes on the chip surface for biocompatibility and stability. Then a post-packaging technique was introduced to facilitate operation in a fluid environment. To verify the performance, CV was implemented with a typical redox probe, potassium ferricyanide. We have shown that our system works for the on-chip electrochemical analysis and is well-suited for a handheld, portable instrument.

Chapter 5

PORTABLE IMPEDIMETRIC INSTRUMENT

This chapter presents a low-cost, portable electrochemical analysis system using impedimetric measurements rather than more commonly used potentiometric techniques. The presented impedance spectroscopy (impedimetric) technique uses a small perturbation to obtain a linearized response without affecting the composition of the sample as opposed to cyclic voltammetry (potentiometric) which repeatedly reduces and oxidizes the sample. The presented system consists of an Arduino UNO microcontroller, a CMOS digital-to-analog converter (DAC) chip, a potentiostat, and data acquisition (DAQ) hardware. The Arduino UNO is loaded a program we have written to generated sinusoidal excitations signals in conjunction with the CMOS DAC chip. The CMOS chip fabricated in a standard 0.5 μm CMOS process contains a DAC with a unity gain buffer circuit. The potentiostat is capable of carrying out impedance measurements with both the Randles model and a potassium chloride (KCl) solution. We describe a behavioral model of the op-amp used in the potentiostat using Verilog-A hardware description language. Verilog-A simulation reduce the error relative to standard Cadence simulations and compare well with known Randles RC values giving an error less than 1%. The impedance measurements for a KCl electrochemical solution were performed with our system and a Gamry commercial electrochemical workstation giving a relative error up to 16% for lower frequencies (below 37 Hz) and up to 31% at higher frequencies. This work was completed in collaboration wiht Vishal Ghorband and Zhijian Lu, two fellow members in Dr. Jennifer Blain Christen's group.

5.1 Background

Electrochemical impedance spectroscopy (EIS) is an experimental technique for measuring the impedance of a system as a function of frequency Barsoukov and Macdonald 2005; Bard and Faulkner 2000 for many applications, such as detection of single-stranded DNA hybridization Anorga et al. 2010, single cell characterization studies Jang and Wang 2007, corrosion studies Nishikata, Ichihara, and Tsuru 1995, adsorption properties of molecules Mohsen, Fadl-allah, and El-Shenawy 2012 and microbial fuel cell research He and Mansfeld 2009.

Generally, impedance measurement techniques can be classified by the excitation functions employed Barsoukov and Macdonald 2005, which are frequency domain Anorga et al. 2010; Jang and Wang 2007; Nishikata, Ichihara, and Tsuru 1995; Mohsen, Fadl-allah, and El-Shenawy 2012; He and Mansfeld 2009 or time domain Yoo and Park 2000; Yoo et al. 2003; Chang and Park 2007; X. Huang et al. 2011. For the frequency domain methods, the impedance is normally measured by applying a small amplitude AC signal that is varied over a range of frequencies Bard and Faulkner 2000. The technique is most commonly used in commercial electrochemical workstations, which are large, complex, and expensive. Time domain based methods involve a small amplitude potential step used as the excitation source with the current response collected, followed by proper data analysis. This measurement strategy is limited by the sampling rate, the total number of the sampled points, and signal to noise ratio X. Huang et al. 2011; it also requires complicated instrumentation and data analysis. Even commercial potentiostats cannot meet these requirements Yoo and Park 2000. Our aim is to demonstrate a portable impedance measurement device for biological applications that can be used in a point of care setting.

In this paper, we describe a portable EIS instrument using Arduino UNO interfaced to DAC to produce a small sinusoidal signal. A CMOS chip, which contains a DAC and a unity gain buffer, was designed and fabricated in a standard 0.5 μm CMOS process. The purpose of the unity gain buffer is to ensure that the amplifier's non-inverting input to the potentiostat does not disrupt the DAC circuitry producing the small sinusoidal signal. Then, the output voltage was recorded by DAQ (NI-USB-6212). After appropriate data analysis, the magnitude and phase of the detected impedance were obtain.

5.2 Complex Impedance Measurement Theory

An impedance measurement is usually performed by applying a small amplitude AC potential to a Randles equivalent circuit or electrochemical cell and then collecting the response current through the cell as shown in Fig. 22(a). The reason for applying the small sinusoidal excitation is to ensure the electrochemical system behaves linearly Bard and Faulkner 2000. However, real electrochemical cells exhibit more complex behavior. A Randles equivalent model, which consists of a solution resistance R_s, a double layer capacitance C_d and a charge transfer resistance R_{ct}, is used to simplify the electrochemical cell model as demonstrated in Fig. 22(b). In a linear system, the current response to sinusoidal excitation should be a sinusoidal signal at the same frequency but with an amplitude decrease and phase shift (φ in Fig. 22(c)). Thus the impedance of the system can be expressed as equation (5.1).

$$Z = -\frac{V_{in}}{V_{out}} R_f = \mid Z \mid e^{(\varphi - \pi)} = Z_{re} + jZ_{im} \tag{5.1}$$

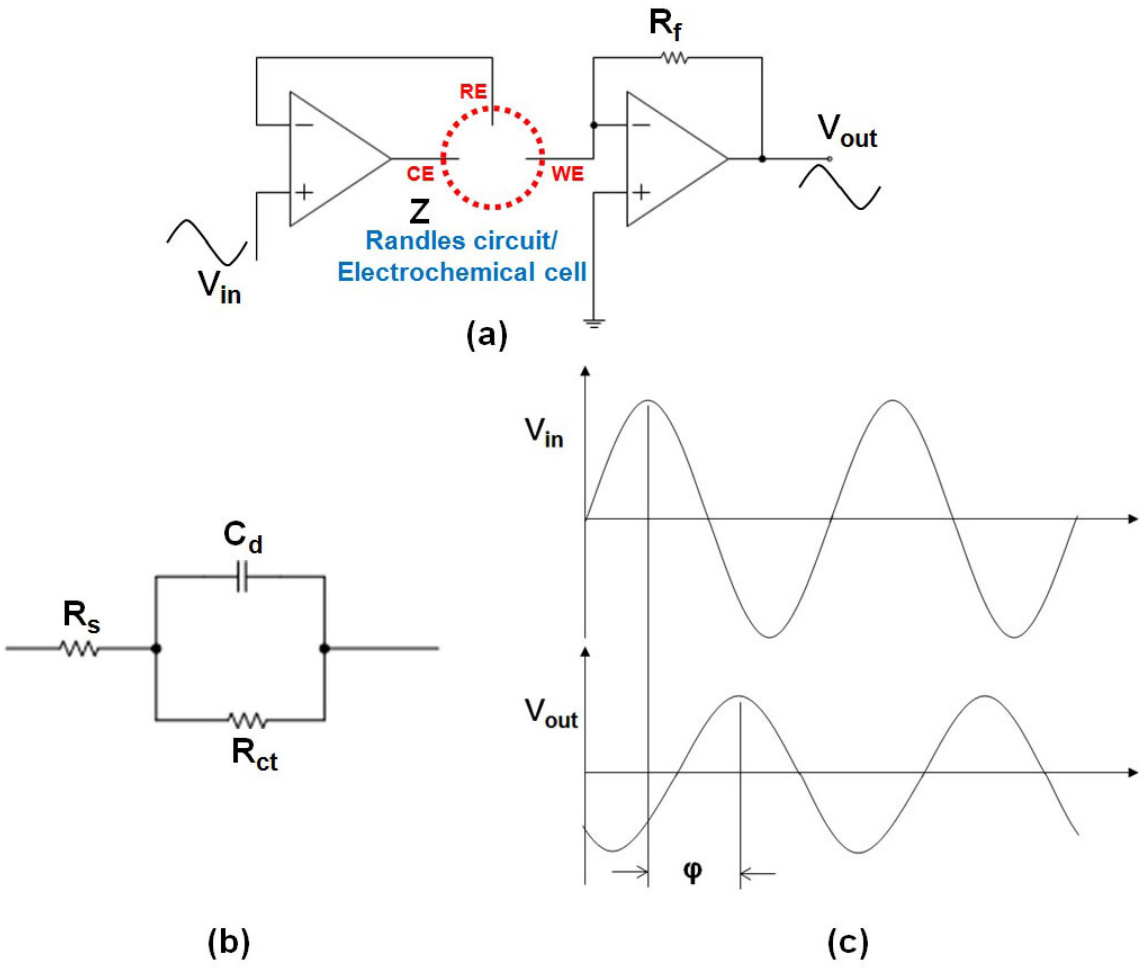

Figure 22. (a) Impedance measurement system with potentiostat (b) Simplified Randles circuit schematic diagram contains solution resistance R_s, double layer capacitance C_d & charge transfer resistance R_{ct} (c) Sinusoidal response to a Randles circuit or electrochemical system. φ denotes phase shift between V_{in} and V_{out}.

where Z is the impedance of the system, V_{in} and V_{out} are the input potential and output response signal, respectively, R_f is the feedback resistance, φ is phase shift between input signal and output signal, j is the imaginary unit, and Z_{re} and Z_{im} are the real part and imaginary part of Z.

The equivalent impedance of Randles model can be described by equation (5.2).

$$Z = R_s + \frac{R_{ct}}{1 + \omega^2 {R_{ct}}^2 {C_d}^2} - j\frac{\omega C_d {R_{ct}}^2}{1 + \omega^2 {R_{ct}}^2 {C_d}^2} \tag{5.2}$$

where $\omega = 2\pi f$ is the angular velocity. Therefore, the real and imaginary parts of the system impedance are given by equations (5.3) & (5.4).

$$Z_{re} = R_s + \frac{R_{ct}}{1 + \omega^2 {R_{ct}}^2 {C_d}^2} \tag{5.3}$$

$$Z_{im} = -\frac{\omega C_d {R_{ct}}^2}{1 + \omega^2 {R_{ct}}^2 {C_d}^2} \tag{5.4}$$

5.3 Simulations

5.3.1 Verilog-A & Cadence Simulation

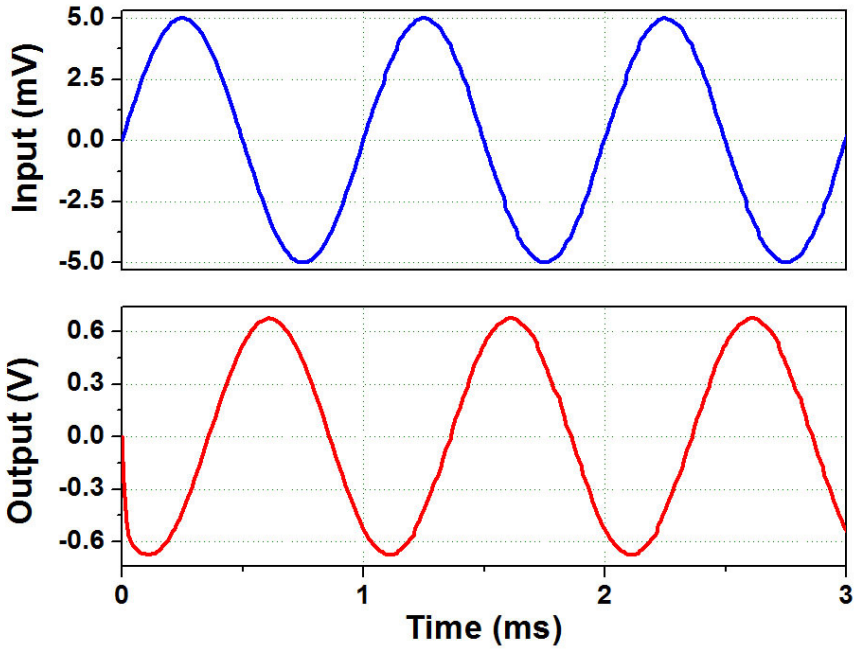

Figure 23. Typical EIS waveforms showing gain and phase shift at 1 kHz

The impedance measurement circuit was simulated to determine the gain and phase difference we expect to measure for a given Randles model using a spectre circuit simulator in Cadence. Verilog-A hardware description language provides a new dimension in modeling, design, and simulation capability for analog and mixed signal electronic systems. Presently, Verilog-A provides a means to incorporate testability studies in the mixed signal design flow, our reason for performing Verilog-A simulations of this system. Using a Verilog-A module for the op-amp and other components, including resistors and capacitors, gives more practical results from simulations.

The main Verilog-A module in this system is an op-amp. Based on the datasheet and our tests of the performance of the op-amp, we obtained the specifications (e.g., DC gain, phase margin, slew-rate and unity gain bandwidth). These values were used to create the Verilog-A module for the op-amp which was used in the schematic and simulated in an analog Cadence environment.

The circuit shown in Fig. 22(a) was simulated with a 10 mV peak to peak sinusoidal signal applied to the input of the potentiostat and a feedback resistance R_f of 389 kΩ. The simulated output voltage was measured with the gain and phase of the output signal analyzed to find the real and imaginary impedance of Randles model circuit, where R_s, C_d, and R_{ct} are 220 Ω, 47 nF, and 4.7 kΩ, respectively. We chose these specific values to compare the simulation results with the empirical results in the section 5.4. Fig. 23 demonstrates typical input and output waveforms at 1 kHz.

Many iterations were performed for different frequencies from 1 Hz to 1.5 kHz to accumulatea gain-phase data. Using the mathematical expressions (equations (5.3) & (5.4)) from section 5.2, the real and imaginary impedance of the Randles model were plotted. In Fig. 24, graphs of both theoretical (blue diamond) and simulated (red circle) values of real and negative imaginary values of impedance of Randles model are

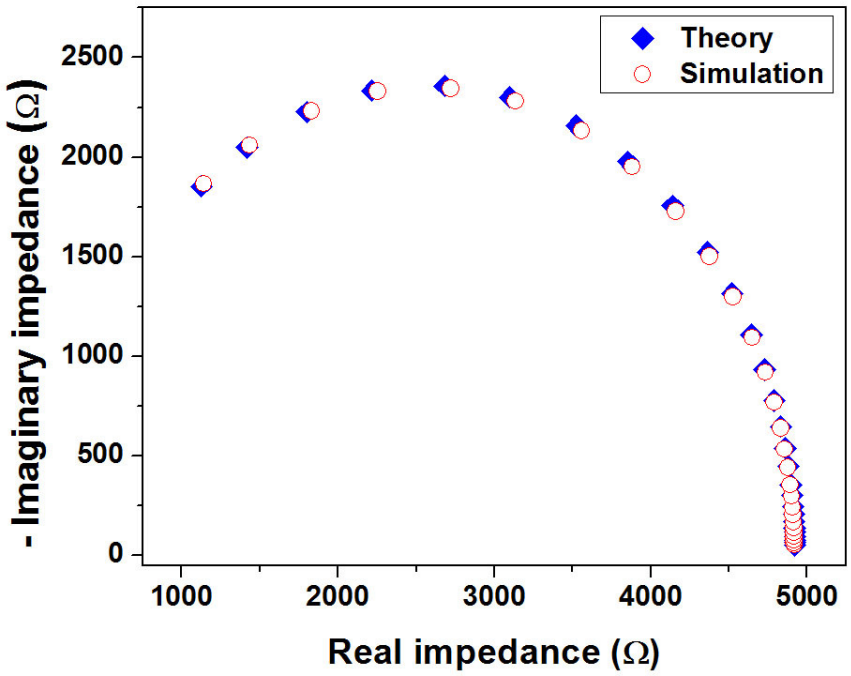

Figure 24. Nyquist plot of the Randles circuit from mathematical calculation (Blue) and simulation (Red).

shown. Compared to the theoretical values the error from the simulations is less than 1%, demonstrating the accuracy that can be achieved with the Verilog-A module.

5.4 Randles Equivalent Circuit Measurements

5.4.1 Hardware

An Arduino UNO microcontroller that provides sets of 10-bit digital I/O pins was used with the DAC to generate the input signals. The Arduino UNO was selected to provide a portable, inexpensive, and precise microcontroller. It is easily programmable by uploading programs via a USB connection. The input signal from the Arduino is converted to a sinusoidal signal using a custom DAC.

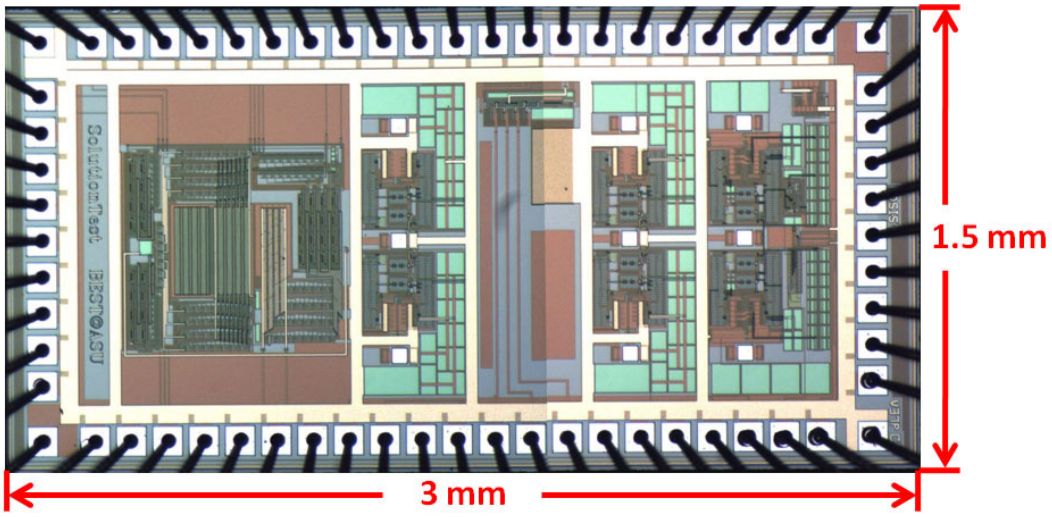

Figure 25. Microphotograph of the 1.5 mm × 3 mm CMOS die.

The 10-bit segmented DAC with unity gain buffer was fabricated in a standard 0.5 μm CMOS process and operates with ±2.5 V power supply. The unity gain buffer is composed of an op-amp circuit that ensures the input side of the circuit (DAC) is isolated from the output, i.e. the potentiostat circuit. The specifications of the CMOS op-amp have been reported previously Luo et al. 2013. Both the static and dynamic performance of the 10-bit CMOS DAC were tested, and the measured specifications are given in Table 1. Fig. 25 show a micrograph of the die which is 1.5 mm × 3 mm.

Table 1. CMOS DAC Specifications

Power Supply	±2.5 V
Reference Voltage (low & high)	-2.5 V & +2.5 V
Quiescent Current	202 μA
Resolution	10 bits
DNL	-0.6∼0.1 LSB
INL	-0.5∼0.7 LSB
Sampling Rate	400 kS/s
SNDR(390.6 Hz at 400 kS/s)	54.85 dB
ENOB	8.8 bits

5.4.2 Experimental Setup

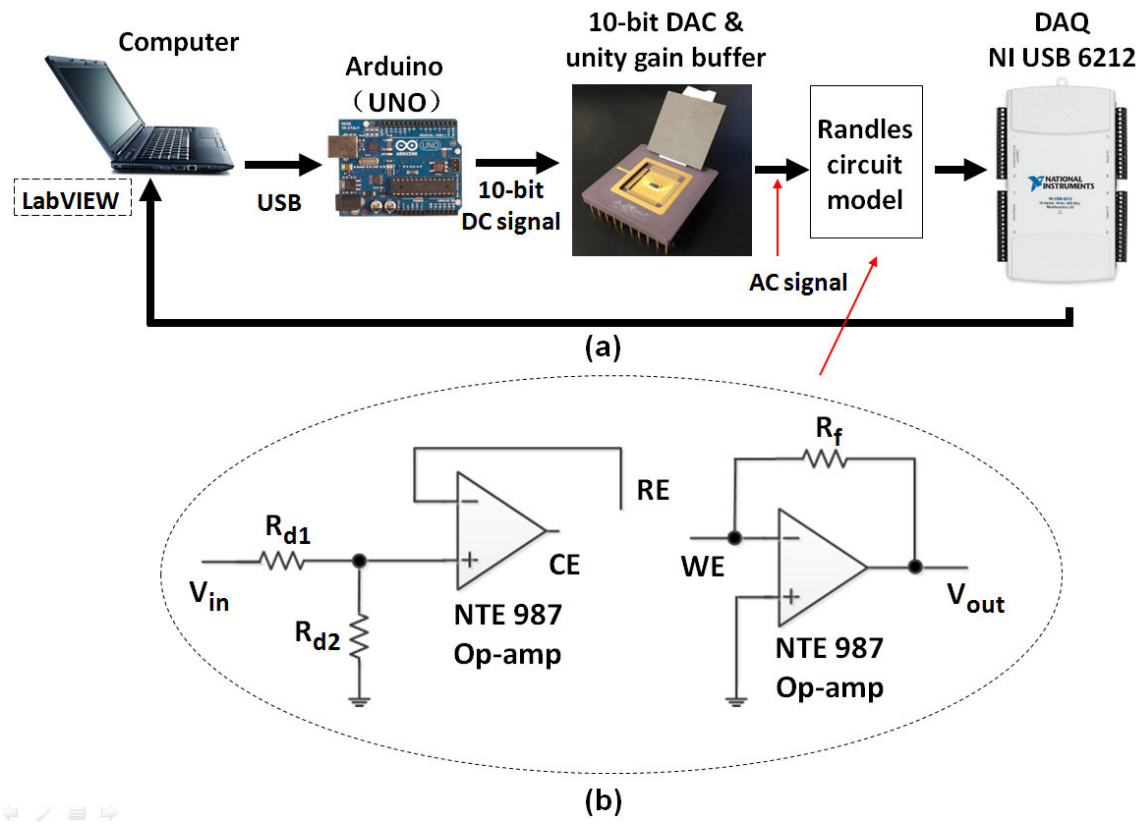

Figure 26. (a) Block diagram of the portable EIS system with a 10-bit DAC designed to provide the AC excitation. (b) circuit diagram for the potentiostat with R_{d1} 506 kΩ, R_{d2} 1.02 kΩ, and R_f 385 kΩ.

The experimental setup for the Randles cell impedance measurement consists of a laptop, an Arduino UNO, a CMOS chip with a 10-bit DAC and unity gain buffer, a potentiostat composed of NTE 987 op-amps, a Randles circuit and a DAQ (NI USB 6212) as shown in Fig. 26(a). The UNO custom code uploaded generated 10-bit DC values with ±2.5 V full scale range. Subsequently, the DC signal was converted to AC signal by the CMOS DAC buffered. Since the ±2.5 V AC signal from the unity

gain buffer was large, a voltage divider was required to produce a ±5 mV amplitude excitation (in Fig. 26 (b)). The impedance response of the Randles model to the excitation was measured using the potentiostat. Finally, the response signal was acquired by the DAQ followed by appropriate data analysis.

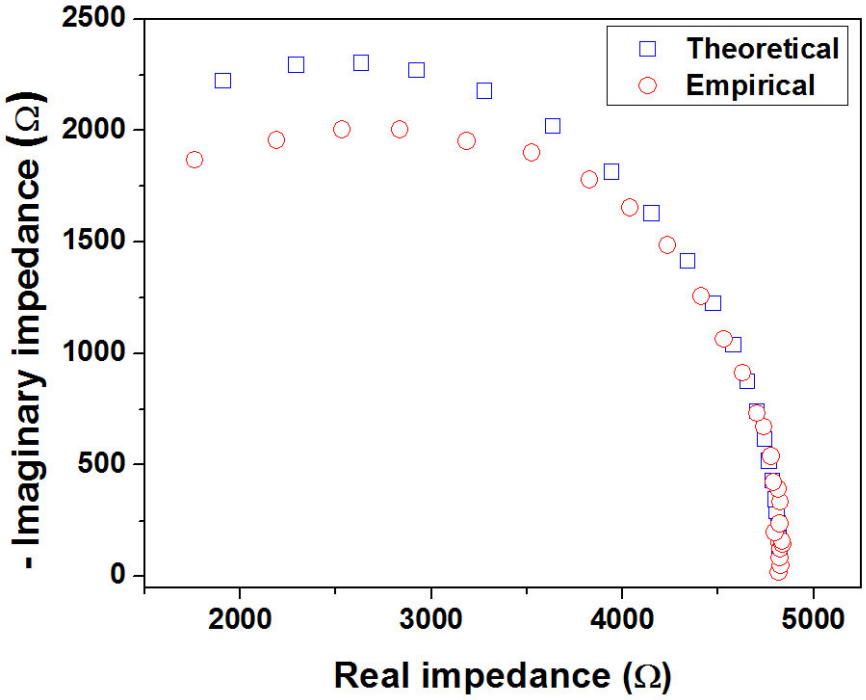

Figure 27. Nyquist plot of the Randles circuit from mathematical calculation (blue squares) and experimental results (red circles).

A Randles circuit with 216 Ω R_s, 44 nF C_d, and 4.61 kΩ R_{ct} was tested to verify our impedance measurement technique. The impedance spectra for the Randles model for both the mathematical calculation and the experimental measurement are plotted in Fig. 27. The experimental measurement was carried out over the frequency range from 8.22 Hz to 1220 Hz. The mathematical calculation closely approximates the experimental measurement at low frequencies. However, the impedance differences between the two becomes larger as the frequency increases. For example, the relative

error with respect to the imaginary impedance between calculated and measured values is approximately 16% at 1220 Hz. We believe this is due to the time delay, caused by the software and discrete components, which plays an important role in the impedance measurements at high frequency.

5.5 KCl Solution Measurements

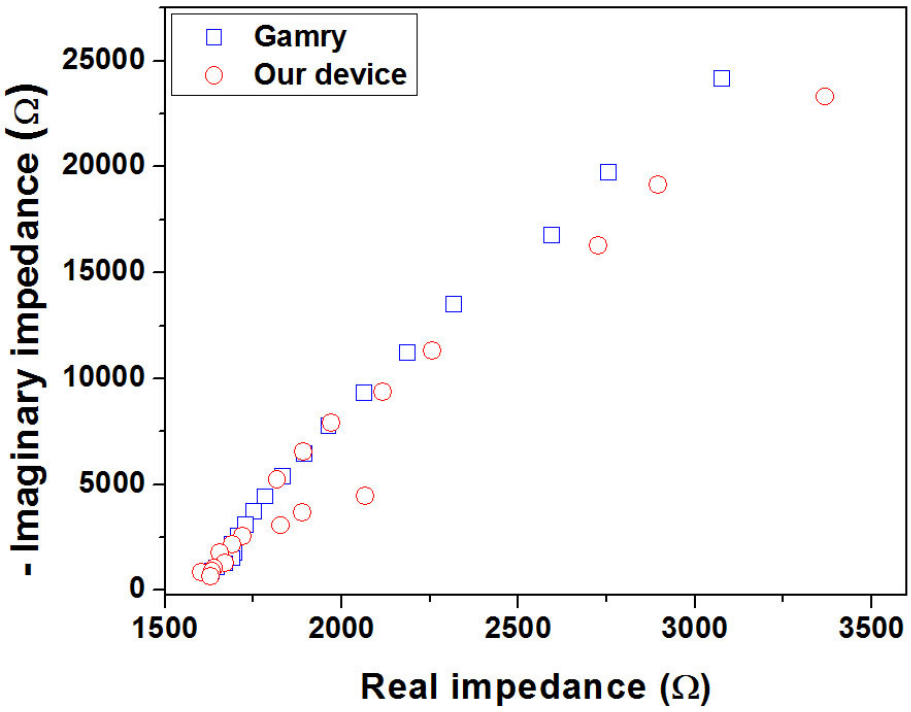

Figure 28. Nyquist plot of 80 μl KCl solution at 4 mM concentration measured by Gamry work station (Blue) and our portable device (Red).

Impedance measurement were performed with a 4 mM KCl solution to evaluate the performance of our device. The potassium chloride was commercially available from EMD Chemicals (PX1405−1). The aqueous solution was diluted using water (18.2 MΩ·cm) purified water from a Milli−Q water purification system. The experiment was

carried out using screen printed carbon electrodes with a three-electrode configuration (CH Instruments Inc., Part number TE100). An eighty μl solution of 4 mM KCl was placed on the electrodes and tested over the frequency range from 37.2 Hz to 1220 Hz with both our instrument and a Gamry commercial electrochemical workstation (Gamry Instruments Inc., Reference 3000^{TM}).

The complex impedance spectra obtained by our portable instrument and the Gamry workstataion are plotted in Fig. 28. This allows us to compared our results with control experiments on the Gamry electrochemical workstation. We had difficulty measuring the KCl solution impedance below about 37.2 Hz. However, the impedance of Randles circuit could be detected starting at about 8.22 Hz. This results from noise at the interface between solution and carbon electrodes. The impedance spectra demonstrated the measurements with our portable instrument were in agreement with measurements made using the Gamry at high frequencies. For the lower frequencies, e.g. at 37.2 Hz, the relative error with respect to the imaginary impedance between our portable device and the Gamry is estimated to be 16.1%. Especially around 60 Hz, the ambient noise generated by power lines strongly affects the impedance measurements. It is interesting that the maximum relative error with respect to imaginary impedance appearing at 147 Hz is approximately 31.1%.

5.6 Conclusion

In this chapter, we reported a portable impedimetric system which consists of an Arduino UNO microcontroller, a CMOS DAC chip, a potentiostat, and DAQ. Our code on the Arduino generated a 10-bit DC signal with $\pm$2.5 V amplitude. In order to convert the DC signal to AC, a DAC circuit was designed and fabricated

in a standard 0.5 μm CMOS process. Since the sinusoidal output from the CMOS chip was $\pm$2.5 V, much larger than desired $\pm$5 mV, a voltage divider was created. The potentiostat was capable of carrying out measurements with both a Randles circuit and KCl solution. Simulations with Cadence were performed to verify the performance our device and improved with Verilog-A modules. The impedance spectra from our device and the Gamry were compared with reasonable results. However, we believe further integration of the system onto a single board with provide significant improvements to the accuracy leading to a viable point of care system.

Chapter 6

A NEW IMPEDANCE MEASUREMENT METHOD

This chapter presents an integrated realization of a simple and fast impedance measurement technique. The impedance spectra are measured by perturbing the system with a small potential stimulus generated by a relaxation oscillator and then obtained by a followed processing of the current response. The circuit, fabricated in a standard 0.5 μm CMOS process, contains a relaxation oscillator and a potentiostat. This CMOS circuit is complete with the help of Dr. Hongyi Wang. The chip occupies 1.5 mm $\times$ 3 mm, and operates from $\pm$2.5 V supplies at 225 μA. The reliability of the instrument was verified by the measurement of Randles equivalent circuit over the frequency range of 0.1 Hz - 3 kHz in a couple of milliseconds, showing good correlation with the known results. The remarkable advantages, i.e. simplicity, rapidity, low noise and miniaturization based on the CMOS process, make this technique a promising candidate for impedance applications.

6.1 Background

Traditional electrical impedance spectroscopy (EIS) method measures the impedance of a system as a function of frequency by applying a small AC signal at each individual frequency Barsoukov and Macdonald 2005. The main limitation while using this technique is the long measurement time over a whole frequency range especially at the low frequency. To solve this limitation, a fast impedance measurement method, in which a potential step was applied to the working electrode and the current response

was recorded, has been proposed Yoo and Park 2000. But their method involves the high performance instruments which are non-portable. Huang et al did some modifications to this algorithm and constructed a portable and low-cost instrument X. Huang et al. 2011. However time delay caused by the discrete component results in error when measuring impedance. Moreover their detection time was approximately 50 times slower than Park's Yoo and Park 2000 and ours. To overcome the time delay issue this letter reports an integrated solution using a relaxation oscillator to provide a small potential step. The system serves as a proof-of-concept and the CMOS realization carries out the impedance measurement over the frequency range of 0.1 Hz - 3 kHz.

6.2 Theory

From chapter 5, we know that the total impedance of the Randles model is given by equation (6.1)

$$Z = R_s + \frac{R_{ct}}{1 + \omega^2 {R_{ct}}^2 {C_d}^2} - j\frac{\omega C_d {R_{ct}}^2}{1 + \omega^2 {R_{ct}}^2 {C_d}^2} \tag{6.1}$$

In Fig. 29, a step voltage V_{ap} is applied to a Randles model. From Kirchhoff's law, the V_{ap} can be expressed as (6.2)

$$V_{ap} = V_{cd} + \left(\frac{V_{cd}}{R_{ct}} + C_d \frac{\mathrm{d}V_{cd}}{\mathrm{d}t}\right) = VH(t) \tag{6.2}$$

where V is the magnitude and $H(t)$ is the step function. Solving the equation (6.2), the V_{cd} is obtained (6.3)

$$V_{cd} = H(t)\frac{VR_{ct}}{R_{ct} + R_s}\left(1 - \exp\left(-\left(\frac{R_{ct} + R_s}{R_{ct}R_sC_d}\right)t\right)\right) \tag{6.3}$$

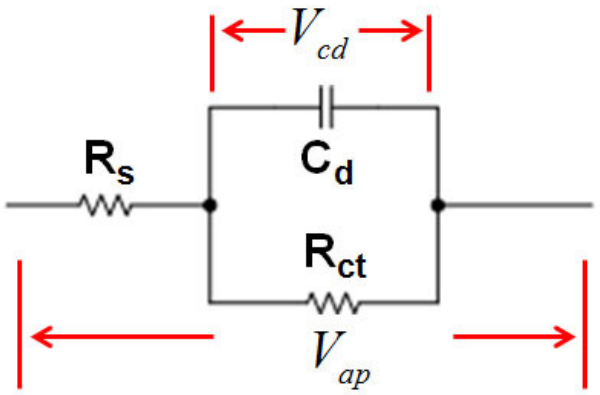

Figure 29. A step voltage V_{ap} is applied to a Randles equivalent circuit.

Therefore, the total current can be calculate by (6.4).

$$I_{total}(t) = H(t)\left[\frac{V}{R_s}\exp\Big(-(\frac{R_{ct}+R_s}{R_{ct}R_sC_d})t\Big) + \frac{V}{R_{ct}+R_s}\Big(1-\exp\Big(-(\frac{R_{ct}+R_s}{R_{ct}R_sC_d})t\Big)\Big)\right] \tag{6.4}$$

which can be simplified further to (6.5).

$$I_{total}(t) = H(t)\Big(\frac{V}{R_{ct}+R_s}\Big)\left[1+\frac{R_{ct}}{R_s}\exp\Big(-(\frac{R_{ct}+R_s}{R_{ct}R_sC_d})t\Big)\right] \tag{6.5}$$

Subsequently the first derivative of applied voltage and the total current is calculated by (6.6) and (6.7).

$$I_d(t) = \frac{\mathrm{d}I_{total}(t)}{\mathrm{d}t} = \delta(t)\frac{V}{R_s} - H(t)\frac{V}{R_s^2C_d}\exp\Big(-(\frac{R_{ct}+R_s}{R_{ct}R_sC_d})t\Big) \tag{6.6}$$

$$V_d(t) = \frac{\mathrm{d}V_{ap}(t)}{\mathrm{d}t} = V\delta(t) \tag{6.7}$$

Then we have the current and voltage expressions (6.8) & (6.9) in frequency domain by taking the Fourier transform.

$$I_{ft}(\omega) = \int_{-\infty}^{\infty} I_d(t)\exp\big(-j\omega t\big)\,\mathrm{d}t = \frac{V}{R_s} - \frac{V}{R_s^2C_d}\frac{1}{\Big(\frac{R_{ct}+R_s}{R_{ct}R_sC_d}+j\omega\Big)} \tag{6.8}$$

$$V_{ft}(\omega) = \int_{-\infty}^{\infty} V_d(t)\exp\big(-j\omega t\big)\,\mathrm{d}t = V \tag{6.9}$$

Finally, the total impedance is describe by (6.10),

$$Z = \frac{V_{ft}}{I_{ft}} = R_s + \frac{R_{ct}}{1 + \omega^2 {R_{ct}}^2 {C_d}^2} - \frac{j\omega {R_{ct}}^2 C_d}{1 + \omega^2 {R_{ct}}^2 {C_d}^2} \tag{6.10}$$

which is identical to equation (6.1).

6.3 Impedance Measurement System

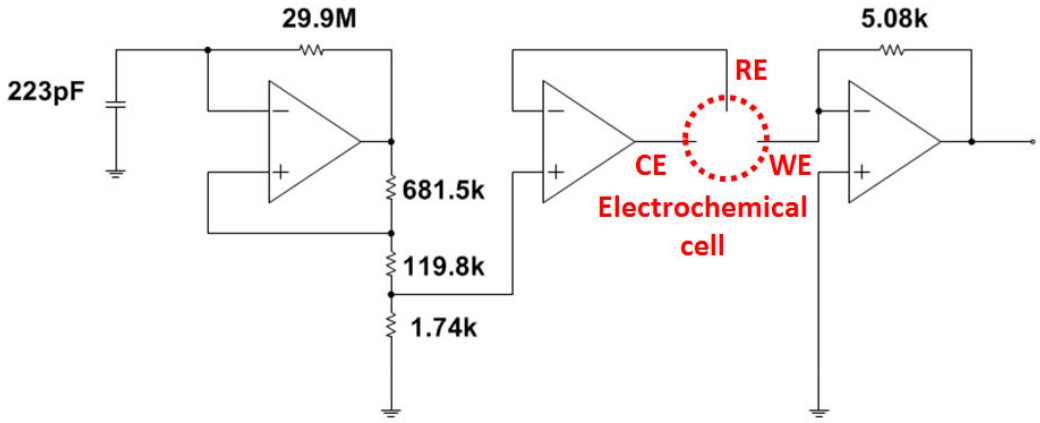

Figure 30. Proposed integrated impedance measurement system.

The proposed integrated impedance measurement sensor consists of a relaxation oscillator and potentiostat as shown in Fig. 30. A Schmitt trigger is employed to implement the relaxation oscillator, which produces a square wave. It is well known that the electrical stimulus must be small enough (normally less than 10 mV) to make sure that the electrochemical system behaves linearly Yoo and Park 2000. Thus, a voltage divider is required to generate 9.5 mV peak-to-peak waveforms in our experiment. In each square wave cycle, there are two edges, i.e. a rising edge and falling edge. A schematic diagram of the potential step (top) and current response

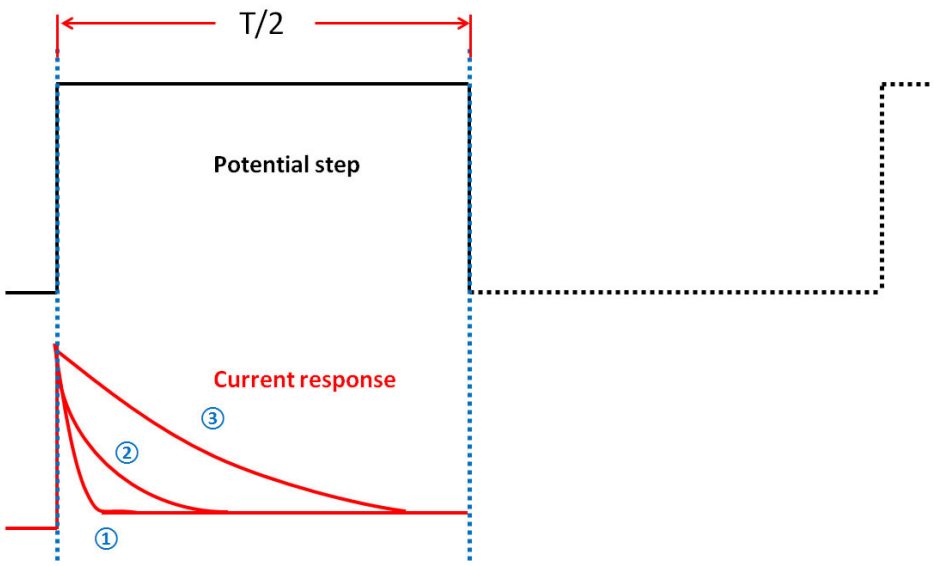

Figure 31. Schematic diagram of the potential step and current response.

(bottom) is shown in Fig. 31. To make impedance measurement, only the rising edge is needed. Then the electrical signals are applied to the electrochemical cell between the reference electrode (RE) and the working electrode (WE) with the potentiostat. Subsequently, the output signals are generated by the response current through the counter electrode (CE). Finally both input and output signals are collected by an oscilloscope (Tektronix DPO3014). By taking the first derivative of the applied potential step and the small chronoamperometric current and subsequently using Fourier transform, the impedance over a range of frequencies is calculated (in section 6.2).

The die microphotograph is demonstrated in Fig. 32. This chip, fabricated in a standard 0.5 μm CMOS process, occupies 1.5 mm $\times$ 3 mm silicon area. The CMOS impedance measurement sensor consists of operational amplifiers for the relaxation oscillator and potentiostat. To support different loading characteristics the class

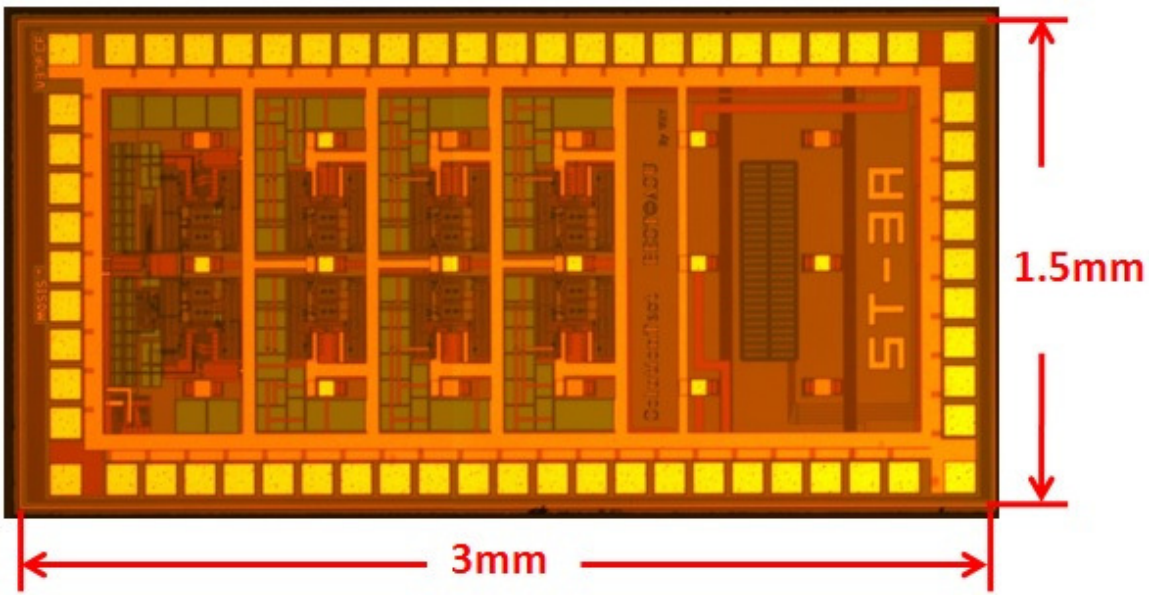

Figure 32. Microphotograph of the fabricated chip.

AB folded-cascode amplifiers with rail-rail input and output are designed to meet the requirements. Another advantage of this kind of amplifier is the low power consumption, enabling efficient use of energy in a portable device. The performance of the op-amp has been tested Luo et al. 2013.

6.4 Results and Discussion

To evaluate the performance of the system, a Randles circuit (inset, Fig. 33) was utilized as the equivalent impedance to be measured from 0.1 Hz to 3 kHz. The Randles model consists of a 1 kΩ resistor (R_s) with the parallel combination of 101 nF capacitor (C_d) and a 10 kΩ resistor (R_{ct}). The square wave generated by the relaxation oscillator is approximate ±4.75 mV, which represents the applied potential step is 9.5

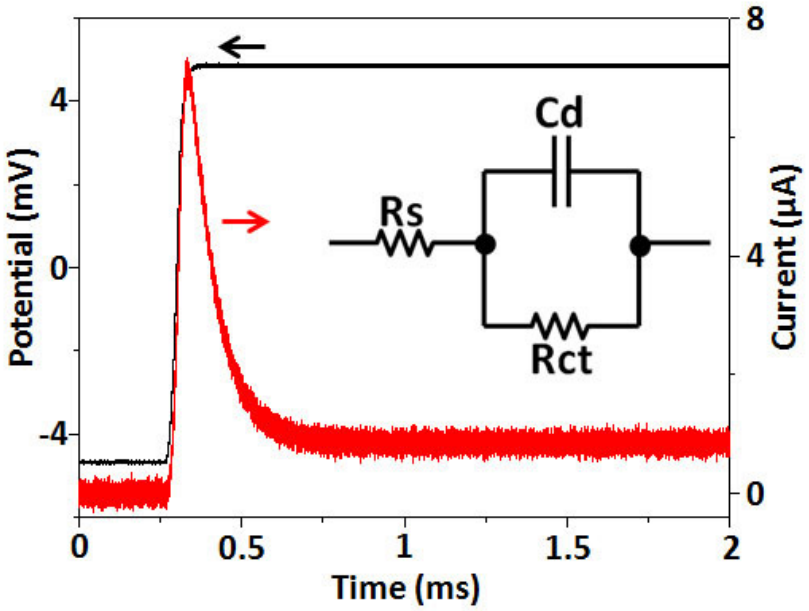

Figure 33. A 9.5 mV peak-to-peak potential step (black) and Transient current observed as the pulse is applied.

mV. Since the amplitude of the applied potential step was around 10 mV, the noise may lead to distortion on data analysis X. Huang et al. 2011. We did not directly collect the actually applied potential. Instead we detected the OPAMP non-inverting input's potential of the relaxation oscillator. From Fig. 30 the potential step actually applied was the detected potential divided by 69.9. The advantage of using a voltage divider is to decrease the input noise signal. The response current was the output signal divided by the 5.08 kΩ resistance. The actually applied potential step and response current were demonstrated in Fig. 33. After analysis described in section 6.2, Fig. 34 shows the real and negative imaginary impedance of Randles circuit over the bandwidth of 0.1 Hz to 3 kHz. To obtain the Randles model parameters, the fitting of the equivalent circuit is performed. The experimental parameters are R_s 1.06 kΩ,

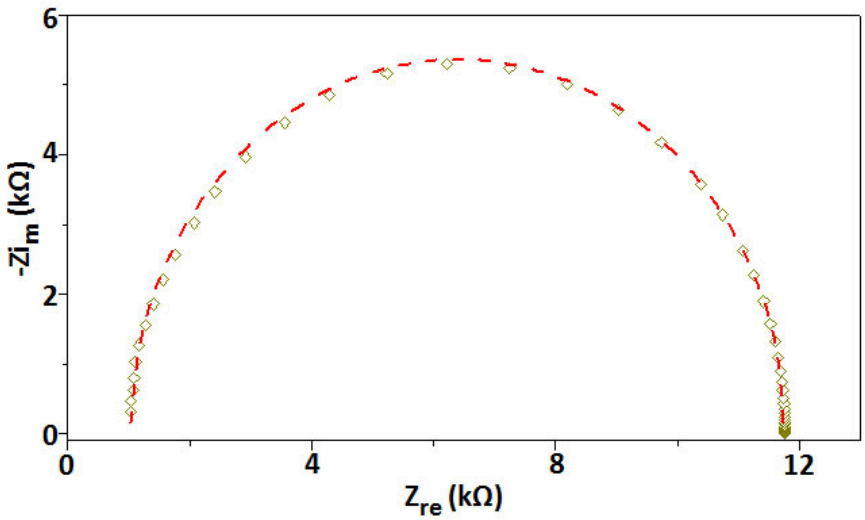

Figure 34. Nyquist plot of the Randles circuit measured by this integrated impedance system. The red dash line represents the fitting curve.

C_d 104.5 nF, and R_{ct} 10.7 kΩ, which have the errors 6.0%, 3.5%, and 7.0% with the known reference values.

It should be noted that for our experiment only a couple of milliseconds are needed to make measurements. Followed by the appropriate analysis, the tested magnitude and phase of different concentrations of equivalent circuit over the bandwidth of 0.1 Hz to 3 kHz can be obtained. For bioelectrochemical applications, low frequencies (less than 100 Hz) are of interest Bhavsar et al. 2009. Measuring the impedance spectra at low frequencies is essential. We extracted the electrical parameter values by fitting measured data to Randles equivalent circuit Fig. 34. Thus, this impedance measurement technique based on the relaxation oscillator is an effective method to investigate the impedance properties. By utilizing the integrated impedance detection system, the delay time can be significantly reduced.

In addition, record time and sampling rate are important factors to this method if it is not properly dealt with. In Fig. 31, because only the rising edge is required, the

measurement time is approximately equal to or less than half of the square waveform cycle, $T/2$. According to equation (6.5), the response current decreases exponentially. Thus, different response current curves in Fig. 31 mainly result from the exponential decay constant, i.e. $(R_{ct}+R_s)/(R_{ct}R_sC_d)$. It is obvious that the curve 1 decays faster than curve 3, which means the exponential decay constant of curve 1 is greater than that of curve 3. The noise level of the instrument is estimated to be 5 mV. Thus, the response signal can not be detected less than 5 mV. Since the chip operates at 5 V, which means the maximum potential is 5 V, the exponential cutoff of the response signal is approximately chosen to be $0.001 \approx e^{-6.9} = e^{-\alpha_1}$, i.e. $\alpha_1 = 6.9$. As a result, the decay time t_1 is calculated by (6.11),

$$t_1 = \frac{\alpha_1 R_{ct} R_s C_d}{R_{ct}+R_s} \leq T/2 \tag{6.11}$$

which means the period of square wave is estimated to be (6.12).

$$T \geq \frac{2\alpha_1 R_{ct} R_s C_d}{R_{ct}+R_s} \tag{6.12}$$

For the Randles model in our experiment, the decay time is approximately equal to 0.64 ms and the period of square wave should be greater than 1.3 ms. Lasia et al reported that the acquired impedance spectra may be reliable only for frequencies between $1/(N\Delta t_s)$ and $1/(2\Delta t_s)$ Jurczakowski and Lasia 2004, where N denotes the number of points obtained in the experiments and Δt_s is the sampling time. The record time is the product of N and Δt_s, and the sampling rate is the reciprocal of Δt_s. Therefore, it may be feasible to perform multiple impedance tests with various sampling rates and then combining the reliable segments in each measurements together to obtain the impedance spectra.

Finally, though real world signals are analog in nature, is it preferable to convert them in digital domain using an analog to digital converter (ADC) Kozak and Kale

2003; Schreier and Temes 2005; Ortmanns and Gerfers 2006. The reasons are the high accuracy, and reliability of digital circuits, and the low-cost, low-power, as well as high-speed device produced by digital VLSI techniques. Therefore, it is important to discuss the oversampling principle, which can improve the resolution of the conversion. From the equation (6.5), the response signal potential V_{out} is given by (6.13)

$$V_{out}(t) = H(t)\left(\frac{VR_f}{R_{ct}+R_s}\right)\left[1+\frac{R_{ct}}{R_s}\exp\Big(-(\frac{R_{ct}+R_s}{R_{ct}R_sC_d})t\Big)\right] \tag{6.13}$$

where R_f is the feedback resistance. It is obvious that the maximum output potential is $V_{MAX} = VR_f/R_s$ when V_{out} is at $t = 0$. To find the power of output signal, the square of V_{out} is calculated by (6.14).

$$\begin{aligned} V_{out}^2(t) = H^2(t)\left(\frac{VR_f}{R_{ct}+R_s}\right)^2\Bigg[1+\frac{2R_{ct}}{R_s}\exp\Big(-(\frac{R_{ct}+R_s}{R_{ct}R_sC_d})t\Big) \\ +\frac{R_{ct}^2}{R_s^2}\exp\Big(-(\frac{R_{ct}+R_s}{R_{ct}R_sC_d})2t\Big)\Bigg] \end{aligned} \tag{6.14}$$

Thus, the response signal power σ_{sig}^2 is obtained by (6.15).

$$\begin{aligned} \sigma_{sig}^2 &= \frac{1}{t_1}\int_0^{t_1} V_{out}^2\,\mathrm{d}t \\ &= \left(\frac{VR_f}{R_{ct}+R_s}\right)^2\left[1+\frac{2R_{ct}}{\alpha_1 R_s}\Big(1-\mathrm{e}^{-\alpha_1}\Big)+\frac{R_{ct}^2}{2\alpha_1 R_s^2}\Big(1-\mathrm{e}^{-2\alpha_1}\Big)\right] \end{aligned} \tag{6.15}$$

where t_1 and α_1 is from equation (6.11). Because of $e^{-\alpha_1}\approx 0.001$, equation (6.15) could be simplified to (6.16).

$$\sigma_{sig}^2 \approx \left(\frac{VR_f}{R_{ct}+R_s}\right)^2\left[1+\frac{2R_{ct}}{\alpha_1 R_s}+\frac{R_{ct}^2}{2\alpha_1 R_s^2}\right] \tag{6.16}$$

Consider a B_{int} bit ADC with $2^{B_{int}}$ quantization levels, i.e., with quantization error $\Delta = 2V_{MAX}/(2^{B_{int}}-1)\approx 2V_{MAX}/2^{B_{int}}$. The power of the quantization error σ_e^2 is given by (6.17).

$$\sigma_e^2 = \frac{\Delta^2}{12OSR} \approx \frac{V_{MAX}^2}{3\cdot 2^{2B_{int}}OSR} = \frac{V^2R_f^2}{3\cdot 2^{2B_{int}}R_s^2OSR} \tag{6.17}$$

where $OSR = f_s/(2f_b)$ is the oversampling ratio and f_s & f_b are sampling frequency & signal bandwidth. The quotient of the signal power σ_{sig}^2 divided by the quantization error power σ_e^2 is expressed as (6.18).

$$\frac{\sigma_{sig}^2}{\sigma_e^2} = \frac{3 \cdot 2^{2B_{int}} R_s^2 OSR}{\left(R_{ct} + R_s\right)^2} \left(1 + \frac{2R_{ct}}{\alpha_1 R_s} + \frac{R_{ct}^2}{2\alpha_1 R_s^2}\right) \tag{6.18}$$

The signal-to noise ratio SNR is obtained by (6.19).

$$\begin{aligned} SNR &= 10\log_{10}\left(\frac{\sigma_{sig}^2}{\sigma_e^2}\right) \\ &= 6.02B_{int} + 10\log_{10} OSR + 4.77\big[\text{dB}\big] \\ &+ 10\log_{10}\left(\frac{R_s^2}{\left(R_{ct} + R_s\right)^2}\left(1 + \frac{2R_{ct}}{\alpha_1 R_s} + \frac{R_{ct}^2}{2\alpha_1 R_s^2}\right)\right) \end{aligned} \tag{6.19}$$

For the Randles equivalent circuit used in this chapter, the SNR in expression (6.19) could be rewritten as (6.20).

$$SNR = 6.02B_{int} + 10\log_{10} OSR - 5.59\big[\text{dB}\big] \tag{6.20}$$

According to equation (6.20), every additional bit for the quantizer improves the SNR by almost 6 dB. Further, each doubling of the OSR increases the resolution by approximately 3 dB. Fig. 35 demonstrates the number of bits B_{int} versus the OSR at various SNR values. The curves are linear when the x-axis is in log scale. For a constant SNR value, the enhancement of the OSR corresponds to fewer bits B_{int} required. However, larger OSR needs higher clock frequency, and therefore results in more power consumption Ortmanns and Gerfers 2006. It is clear that increasing B_{int} is an effective way to improve SNR especially when the OSR cannot be increased due to frequency limitation. This sets a tough requirement on the linearity of the multi-bit ADC, which can further complicate tradeoffs (including cost) in real world implementations of the circuit Ortmanns and Gerfers 2006.

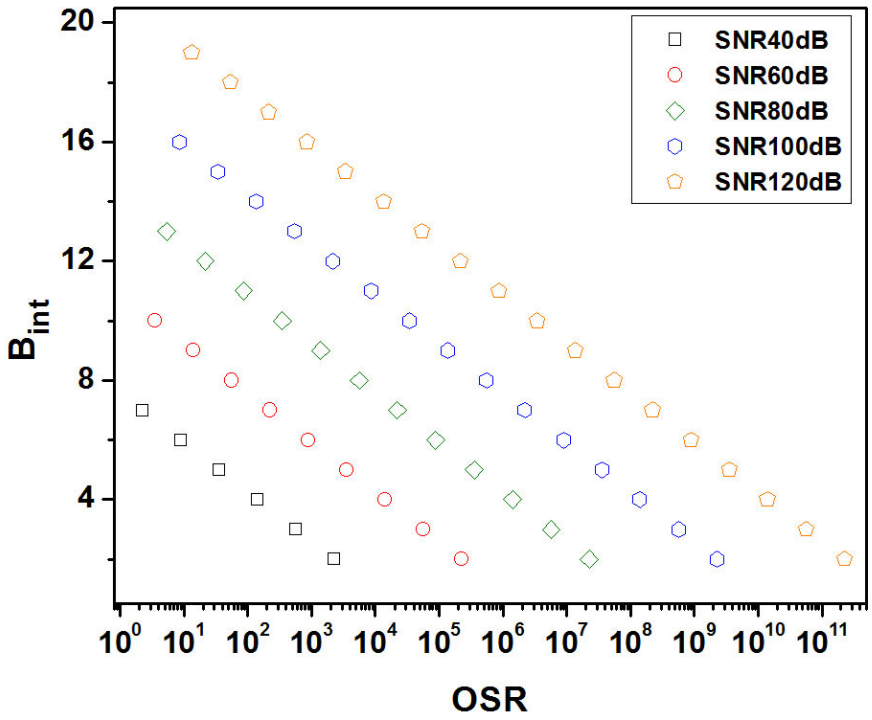

Figure 35. Number of bits B_{int} versus OSR as SNR is 40 dB (black), 60 dB (red), 80 dB (green), 100 dB (blue) & 120 dB (orange).

6.5 Conclusion

A integrated impedance measurement system on a relaxation oscillator was proposed in this chapter. To verify this measurement technique, the experiment with a Randles cell was implemented. The tested result is in good agreement with the real resistors and capacitor. We demonstrated the corresponding CMOS based impedance measurement instrument, which is simple, low-power, low noise and low cost. The apparent advantages make this device promising in the practical impedimetric measurement.

Chapter 7

SQUARE WAVE VOLTAMMETRY

This chapter presents a simple, low-cost square-wave voltammetry (SWV) sensor based on relaxation oscillators. The circuit of the system consists of a square wave relaxation oscillator, a triangle wave relaxation oscillator, and a potentiostat. Relaxation oscillators produce a small amplitude square wave and a triangle wave so the sensor does not require an external signal generator. The whole sensor operates from a ± 2.5 V supply, which made it suitable for utilization in a portable device. The instrument was tested with copper(II) and lead(II) nitrate for simultaneous SWV detection. Oscillation pattern differences are directly observed for different types of metal ions. Electrochemical parameters that exert influence such as various concentration were carefully studied. For measurement results, peak current vs concentration are linearly fitted, which agree with theoretical equation. Advantages with respect to simplicity and low-cost make this technique suitable for practical applications.

7.1 Background

SWV is a powerful electrochemical method in the research of electrode process and analytic measurement Mirceski et al. 2013; Mirceski, Komorsky-Lovric, and Lovric 2007; Lovric 2002; Eccles 1991. Because SWV combines the advantage of pulse techniques, cyclic voltammetry and impedance techniques, this technique is considered as one of the best voltammetric methods. Thus the new SWV devices will expand their application.

However most SWV sensors have been studied using an expensive commercial potentiostat Rattanarat et al. 2014; Cui, Wu, and Ju 2015. These sensor systems are not portable due to bulk and the need to connect with a personal computer. There is a trend to perform rapid on site analyses to minimize the effects of transportation and avoid pre-treatments. Large-size commercial potentiostats can not meet this need. Although several portable commercial potentiostats are available on the market, they are expensive and complicated in terms of both hardware and software Pellicer et al. 2010; Nagatani et al. 2011. Economou et al designed a "virtual" SWV instrument which contains a potentiostat powered by two 9V batteries, and a 6025 E multifunction I/O card (National Instruments, Austin, TX) Economou et al. 2002. The card is programmed by LabVIEW to control the potentiostat. But because of the software delay and slow conversion time of ADC the time delay will result in error in peak detection. To solve this problem, Chen et al proposed a more complicated design in hardware based on an FPGA, which makes cost prohibitive Chen and Du 2010. With SWV, the oscillation pattern of the response signal contains the insight into the electrode mechanism and electrokinetic information of the electrode processes especially at the peak current Bard and Faulkner 2000. Unfortunately, none of them has demonstrated the response oscillation pattern in the time domain.

Recently, Lim et al proposed a SWV redox sensor fabricated in standard CMOS process technology Lim et al. 2013, 2014. They measured a potassium ferricyanide solution from 0.6 mM to 6 mM by controlling the square wave pulse generator. However, their ability to detect low concentration is poor. Moreover they could not demonstrate the simultaneous detection of multi-metal ions.

In this paper we present the design and construction of a simple but effective device for SWV. The SWV instrument is based on a square wave relaxation oscillator

and a triangle wave relaxation oscillator, which generate a small amplitude square wave and a triangle wave. The circuit of the sensor system is made of commercial op-amps (NTE987) and inexpensive electronic components (resistors and capacitors), which allow for mass production at low-cost. In addition, the device operates from a ±2.5 V supply, which makes it a candidate for portable use. Our algorithm for this design is evidently simplified which did not require the complicated hardware and controlled software. Therefore, the system avoids software delay issues and eliminates the slow conversion time of ADC, which results in the error associated with detection of peak current. The sensor system can demonstrate the current response oscillation patterns for various chemical species in the time domain so that the significant details of current peak are observed. The algorithm simplified the instrument and made this method very suitable for practical applications.

7.2 Experimental Section

7.2.1 Chemical Reagents

Copper(II) nitrate and lead(II) nitrate were commercially available from J.T. Baker (Product number:1800−01) and Sigma−Aldrich (Product number:228621), respectively and were used without further purification. Acetate buffer solution of 0.1 M at pH 4.7 was prepared by mixing stock solutions of acetic acid and sodium hydroxide. The water (typical resistivity 18.2 MΩ·cm) used to prepare all the solutions was purified with a Milli−Q water purification system.

7.2.2 System Architecture

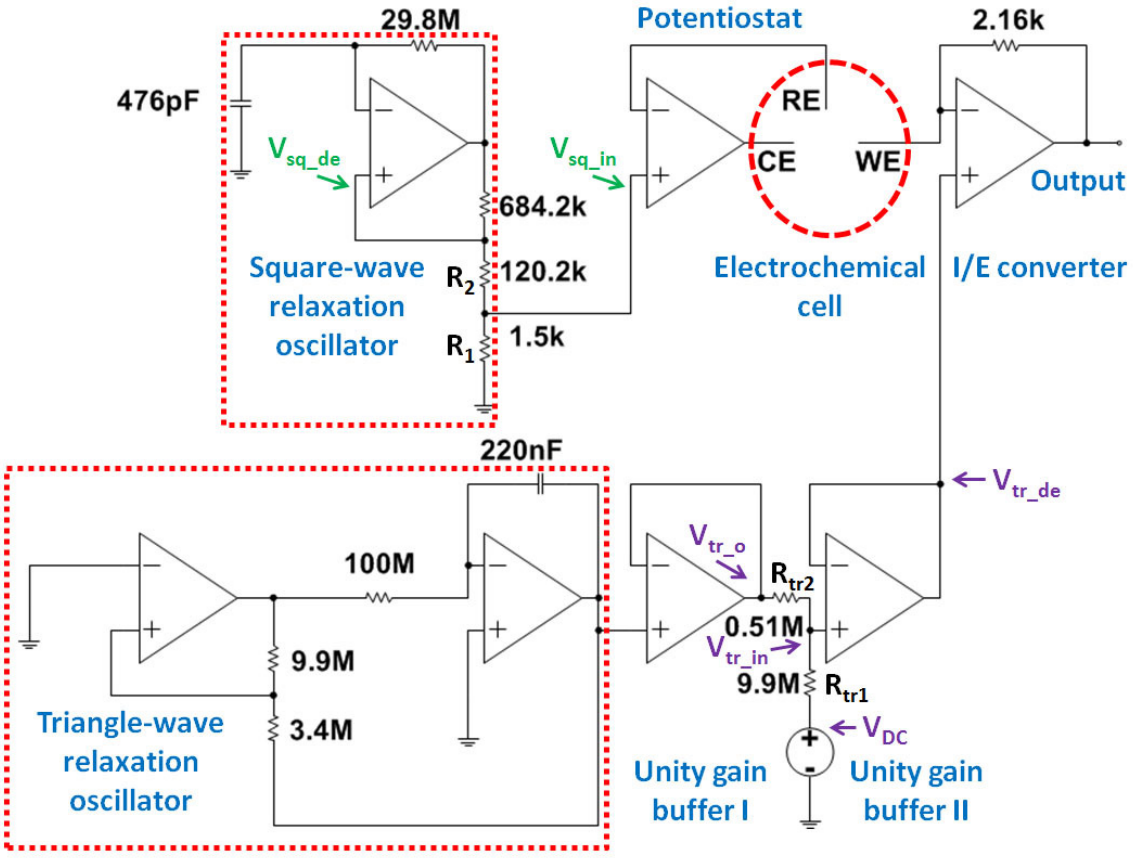

Figure 36. A schematic diagram of the system architecture shows the square wave relaxation oscillator, the triangle wave relaxation oscillator and the potentiostat. The square wave relaxation oscillator and the voltage divider produced a small amplitude (∼7 mV) perturbing the electrochemical system. The triangle wave relaxation oscillator was used to generated the scan potential ramped at low speed (∼50 mV/s). The aim of the unity gain buffer is to ensure that the buffer isolates the input side of the circuit from the output side.

Our measurement system mainly consists of a square wave relaxation oscillator, a triangle wave relaxation oscillator and a potentiostat as demonstrated in Fig. 36. All

of them are made of commercial op-amps (NTE987), which operate from a ±2.5 V supply.

7.2.2.1 Square Wave Relaxation Oscillator

The op-amp relaxation oscillator demonstrated in Fig. 36 produced a square wave. The circuit's period of square wave oscillation relied on the charge and discharge of a capacitor (476 pF) through a feedback resistor (29.8 MΩ) Bakshi and Godse 2009. The oscillator utilized positive feedback, i.e. Schmitt trigger circuit, which increased the gain of the amplifier. The high gain resulted in the op-amp's output to switch fast from one state to another and vice versa. The positive feedback was used to add hysteresis to the transition threshold voltage. The op-amp square wave oscillator was valid over the frequency range of about 10 Hz - 10 kHz. At the higher frequencies, the op-amp slew rate limited the slope of the output square wave. As an approximation, an electrochemical system is considered as a linear system when small potential perturbations are applied Bard and Faulkner 2000. However, the output voltage of the square wave oscillator, i.e. positive and negative saturation, were approximately 3.7 V peak-to-peak, which violated the linearity requirement of the electrochemical system. Thus, a voltage divider was needed to make the square wave amplitude small (peak-to-peak amplitude ∼7 mV). Subsequently, this small-amplitude square signal was applied to the electrochemical system using a potentiostat.

7.2.2.2 Triangle Wave Relaxation Oscillator

The potential waveform of SWV is made up of a superposition of a square wave onto an underlying staircase Bard and Faulkner 2000. The response current was sampled at the end of the forward potential pulse and at the end of the reverse potential pulse. However, this measurement strategy required a very complicated circuit design. This paper presented a new method employing a linear sweep voltage at slow speed instead of a staircase voltage. This algorithm simplified the instrument, and therefore made this technique suitable for a low-cost device in future applications. Using an op-amp integrator circuit rather than RC, a triangle wave, which had two liner sweep segments, was produced as shown in Fig. 36. However to make SWV measurements, only the sweep potential ramped from low to high voltage was needed. The SWV response peaks appeared at approximately -0.1 V, and -0.6 V for Cu(II) and Pb(II), respectively, in their coexistence Wei et al. 2012. In order to adjust the linear ramp range and include -0.1 V, and -0.6 V, a divider and DC offset V_{DC} were required in Fig. 36. Thus, the adjusted linear sweep potential was described by equation (7.1)

$$V_{tr\_de} = V_{tr\_in} = \frac{V_{tr\_o}R_{tr1} + V_{DC}R_{tr2}}{R_{tr1} + R_{tr2}} \tag{7.1}$$

where V_{tr_o} is the output of unity gain buffer I, V_{tr_in} is the non-inverting input of unity gain buffer II, V_{tr_de} is the output of unity gain buffer II measured by an oscilloscope (Tektronix DPO3014), and R_{tr1} & R_{tr1} are 9.9 MΩ & 0.5 MΩ respectively. Because R_{tr1} was much great than R_{tr2} (i.e. $R_{tr1} \gg R_{tr2}$), equation (7.1) could be simplified further to equation (7.2).

$$V_{tr\_de} = V_{tr\_in} = V_{tr\_o} + \frac{R_{tr2}}{R_{tr1} + R_{tr2}}V_{DC} \tag{7.2}$$

The purpose of the unity gain buffer is to make sure that the buffer isolates the input side of the circuit from the output side. Then the linear sweep potential from the unity gain buffer was applied to the electrochemical cell.

7.2.2.3 Potentiostat & Current-to-Voltage Converter

In Fig. 36, a potentiostat is an electronic instrument which controls a three-electrode cell, i.e. a working electrode (WE), a reference electrode (RE) and a counter electrode (CE). The potentiostat system maintains the WE potential with respect to the RE by adjusting the current through the CE. The small-amplitude square signal and the linear sweep potential were applied to the RE and WE, respectively.

The electrochemical cell current is measured by the current-to-voltage (I/E) converter, which forces the cell current to flow through a feedback resistor (2.16 kΩ). Thus the cell current is equal to the voltage drop over the feedback resistor. In some experiments, because the current varies by several orders of magnitude, a number of various resistors are required to be automatically switched into the I/E circuit Chen and Du 2010. But for our experiments, because the cell current doesn't change too much (approximately from $\sim$15 μA to $\sim$1.5 μA), using a single resistor is enough for the current detection.

7.2.3 Methods

Using our instrument for SWV detection, chemical solutions were added on the screen-printed electrode (CHI TE100). Under the same experimental conditions, selective and simultaneous detections of Cu(II) and Pb(II) were performed. To measure

the signal from the I/E converter, a low noise preamplifier (SR560, Stanford Research Systems) with a low pass bandwidth less than 100 kHz was used to filter the output. The square wave signal, the linear sweep signal and the response output were recorded by an oscilloscope (Tektronix DPO3014). Because the external signal generator and the control software were not needed, this technique significantly simplified the design of the SWV detection system. Therefore, this algorithm eliminated the software delay and the slow conversion time of ADC.

7.3 Results and Discussion

7.3.1 SWV Analytical Characteristics of Individual Lead(II)

To verify performance, the lead(II) nitrate solutions at various concentrations were tested individually with our instrument. Volumes of 80 μl containing 0.3 mM lead(II) nitrate and 0.1 M acetate buffer at pH 4.7 were pipetted on the screen-printed electrode. A small-amplitude square wave (peak-to-peak amplitude 7 mV) produced by a square wave relaxation oscillator was applied to the electrochemical cell using a potentiostat. Meanwhile a linear sweep potential from -0.9 V to 0.25 V, generated by a triangle wave relaxation oscillator, was applied to the WE at a scan rate of $\sim$50 mV/s. Fig. 37 (a) demonstrates SWV measurements of 0.3 mM lead(II) nitrate in 0.1 M acetate buffer at pH 4.7. The blue line and the red line denote the linear ramp and the output signal, respectively. The insets of Fig. 37 (a) illustrate the response details near and away from the current peak. From the insets, the oscillation patterns of the response signal change significantly for these locations. The Fig. 37 (b) shows the response waveform obtained near the current peak (top), and small

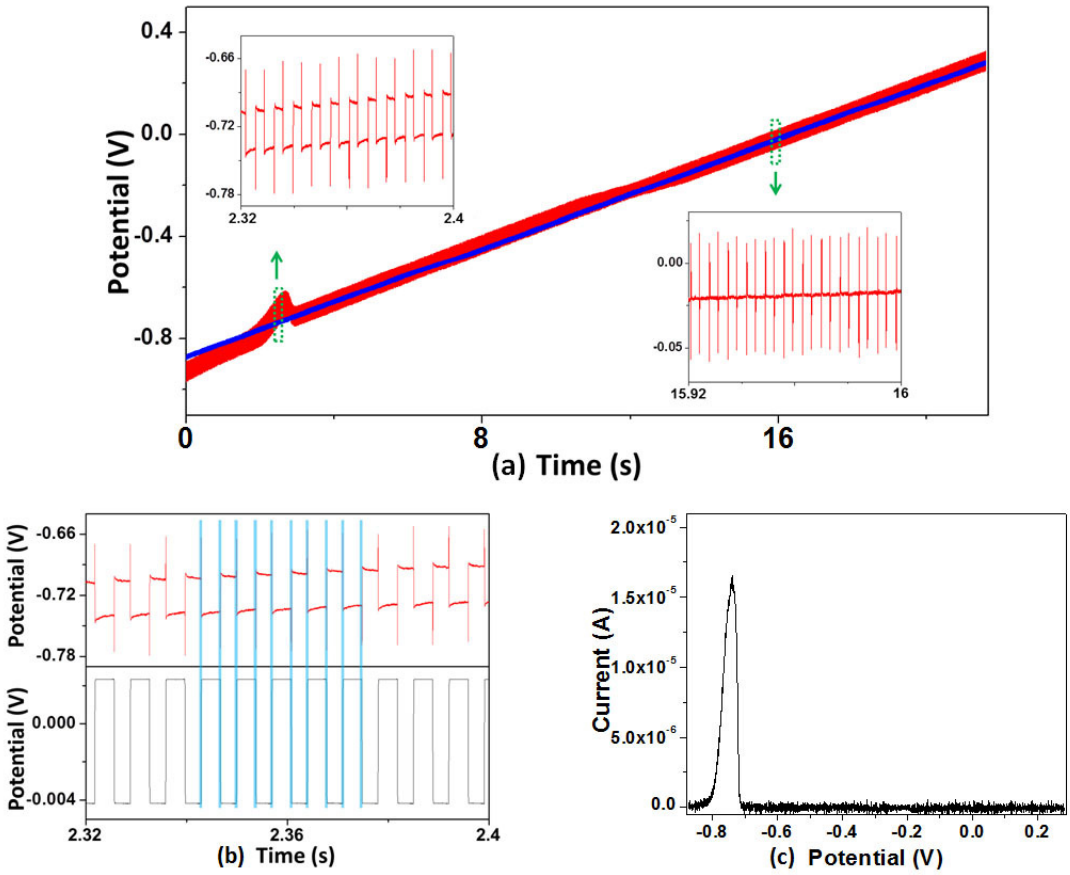

Figure 37. (a) The linear ramp (blue) and the response signal (red) obtained by an oscilloscope for SWV measurement of 0.3 mM lead(II) nitrate in 0.1 M acetate buffer (pH 4.7). The top-left inset and bottom-right inset show oscillation patterns of the response signal near and away from the current peak, respectively. (b) The response signal detail near the current peak (top), and small-amplitude square waveform (bottom). In response to a rising edge or falling edge, overshoots were observed. (c) SWV response of 0.3 mM lead(II) nitrate in 0.1 M acetate buffer at pH 4.7.

square waveform (bottom) applied to the RE. In each square wave cycle, there are two pulses, i.e. the forward pulse and the reverse pulse. For data analysis the response signal obtained from the oscilloscope was sampled twice during one cycle, i.e. one at the end of the forward pulse and another at the end of the reverse pulse. The signal difference of the two measurements in each cycle, and the average value of the linear

sweep potential were both calculated in this cycle. Obviously, the response difference reaches the maximum value at the current peak and is almost zero in other locations. The difference of each pair of current was plotted vs the linear sweep potential in Fig. 37 (c). The peak current for 0.3 mM Pb(II) reached a maximum at potential -0.74 V. This method can minimize the charging current which obscures the faradaic current. SWV causes the current peaks for a faradaic process, in which the peak height is proportional to the concentration of the chemical species of solution as seen in equation (7.3) Mirceski, Komorsky-Lovric, and Lovric 2007.

$$\Delta I_p = nFAC_O^*(D_O f)^{1/2}\Delta\Psi \tag{7.3}$$

where ΔI_p is the peak current, n is the number of electrons, F is the Faraday constant, A is the electrode area, C_O^* is the concentration of the reactant, D_O is the reactant diffusion constant, f is the SWV frequency and $\Delta\Psi$ is the dimensionless peak current, which relies on the square wave amplitude and potential increment in each cycle.

There are a few points that should be noticed in our experiment. First, because the peak-to-peak amplitude of the applied square wave potential is small ($\sim$7 mV), the noise may cause some distortion. Thus, we utilized the oscilloscope to detect the non-inverting input potential of the square wave relaxation oscillator V_{sq_de} instead of the small square wave signal V_{sq_in} as seen in Fig. 36, which is given by equation (7.4).

$$V_{sq\_in} = \frac{V_{sq\_de}R_1}{R_1 + R_2} \tag{7.4}$$

where R_1 and R_2 are 1.5 kΩ and 120.2 kΩ, respectively. Second, the linear sweep potential actually applied to the WE was collected by the oscilloscope. However the noise level of the linear signal would be as small as several mV. In order to minimized the influence of the noise for data analysis, we assume the linear sweep potential

actually applied was exactly as desired by using MATLAB software to create the potential. Consequently, in each square waveform cycle, the mean value of the assumed linear potential was estimated to be the potential staircase. Third, we have to point out that the potential staircase in each cycle is not a constant. But the linear potential increment of each cycle (0.26 mV) is much less than the peak-to-peak amplitude of the square wave (∼7 mV). Therefore we can consider the linear sweep as an approximate constant value for every square wave period. Finally, from Fig. 37, we observed that the output signal could overshoot in response to a rising edge or falling edge. Because these overshoots were undesirable, the response signal obtained from the oscilloscope should be sampled before overshoots appeared, i.e. before the end of the forward pulse or reverse pulse.

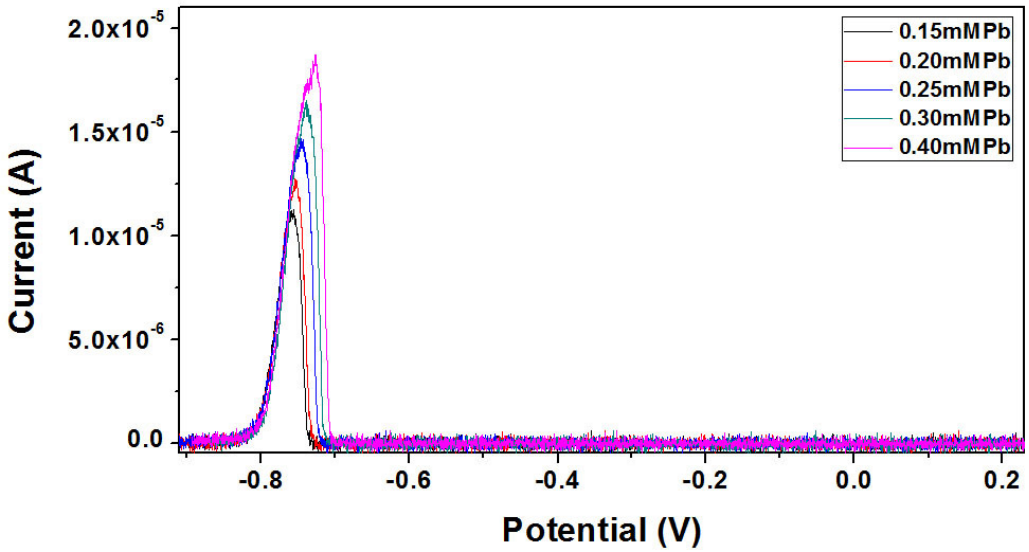

Figure 38. SWV response for the individual analysis of Pb(II) over a concentration range of 0.15 mM to 0.4 mM.

Fig. 38 demonstrated SWV responses with regard to Pb(II) at different concentra-

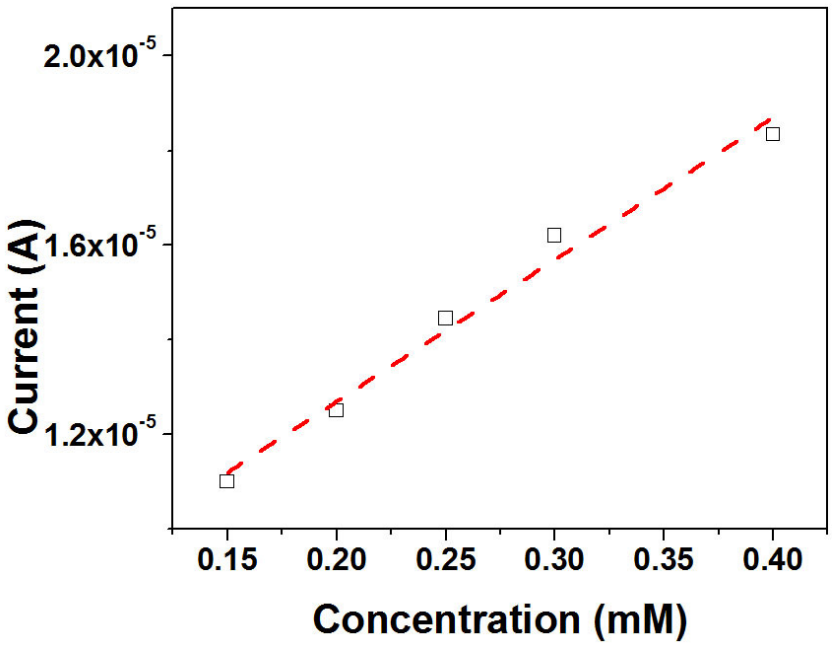

Figure 39. The linear fit line of Pb(II) peak current corresponding to Fig. 38. Supporting electrolyte, 0.1 M acetate buffer (pH 4.7).

tions. Well-defined current peaks were observed in the concentration range of 0.15 to 0.4 mM. The current peaks, which were proportional to the concentration of Pb(II), agreed with the equation (7.3). In Fig. 39, the current vs potential plot was fitted with a linear equation $i/A = 6.71 \times 10^{-6} + 3.00 \times 10^{-5} c/mM$ giving an R^2 value of 0.979. A detection limit is defined as the lowest concentration for which the metal ions were detected against the current baseline. For lead(II), the detection limit was found to $1.5 \times 10^{-5} M$. As seen in Fig. 38 the locations of the current peaks were not stable but changed from -0.758 V to -0.728 V when the concentration of Pb(II) increases from 0.15 to 0.4 mM.

7.3.2 SWV Analytical Characteristics of Individual Copper(II)

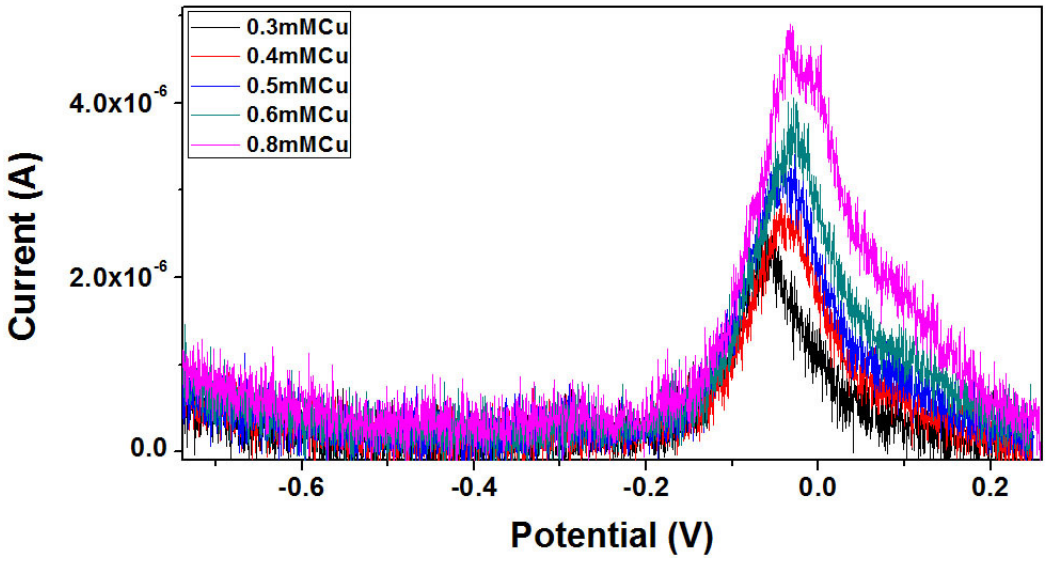

Figure 40. SWV response for the individual analysis of Cu(II) over a concentration range of 0.3 mM to 0.8 mM.

Under the identical experimental condition in Section 7.3.1, Cu(II) was determined using our SWV device. Fig. 40 demonstrates the SWV responses of Cu(II) at various concentrations. It is obvious that the current peak shape of the Cu(II) is poor compared to that of Pb(II). In Fig. 41, the current peaks were proportional to the concentration of Cu(II) in the range of 0.3 to 0.8 mM, which was consistent with equation (7.3). The linearization expression was $i/A = 8.01 \times 10^{-7} + 4.68 \times 10^{-6} c/mM$ with an R^2 value of 0.989. Similarly, the SWV peak positions of Cu(II) at different concentration had a slight shift as the concentration changed.

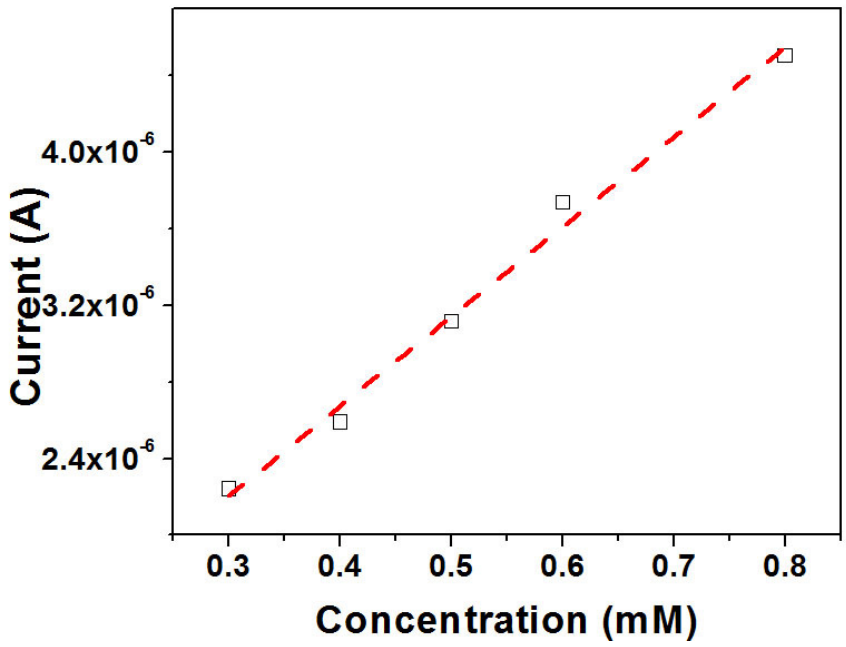

Figure 41. The linear fit line of Cu(II) peak current corresponding to Fig. 40.

7.3.3 SWV Analysis of Simultaneous Detection of Copper(II) and Lead(II)

By using the new instrument, we demonstrated the typical records of SWV analysis for the simultaneous detection of Cu(II) and Pb(II) over the concentration range from 0.3 mM to 0.8 mM and 0.15 mM to 0.4 mM, respectively (in Fig. 42). Well-defined peaks of Pb(II) were observed. However the shape of the Cu(II) peaks were poor especially at high concentration, compare to those of Pb(II). This result was likely because of the formation of Pb-Cu intermetallic compound Wei et al. 2012. In Fig. 43, the linearization equations were $i/A = 1.06 \times 10^{-6} + 7.60 \times 10^{-6} c/mM$ and $i/A = 8.86 \times 10^{-6} + 2.61 \times 10^{-5} c/mM$, with R^2 value of 0.978 and 0.938, respectively. In Fig. 42, the individual peaks of Cu(II) and Pb(II) were estimated at -0.046 V and -0.599 V in their coexistence. The separation between the peaks of Cu(II) and

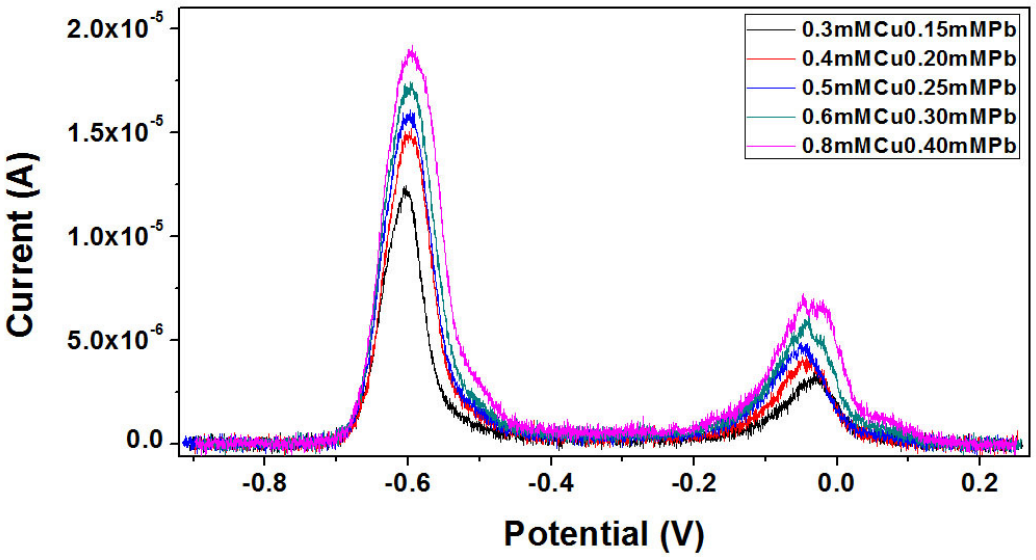

Figure 42. SWV response for the simultaneous analysis of Cu(II), & Pb(II) over a concentration range of 0.3 mM to 0.8 mM, & 0.15 mM to 0.4 mM, respectively.

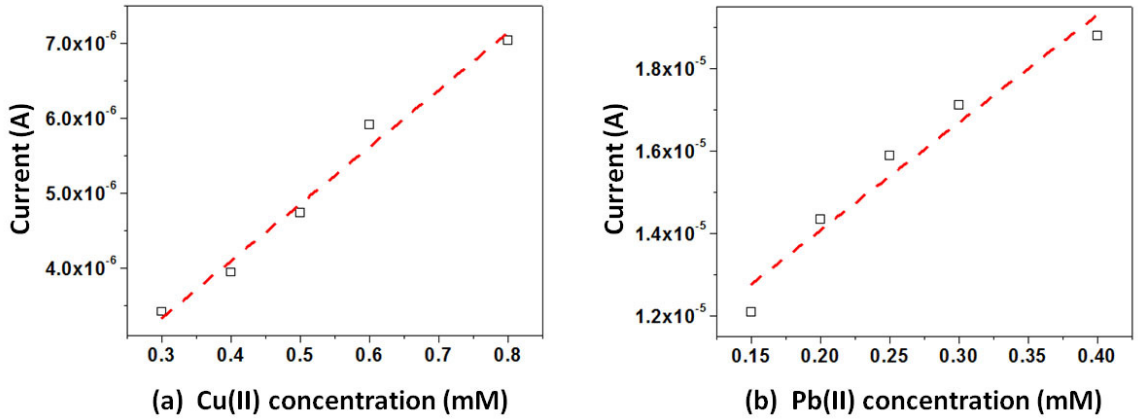

Figure 43. The linear fit lines of Cu(II) & Pb(II) peak current corresponding to Fig. 42.

Pb(II) is so apparent that the simultaneous or the individual detection using the new instrument is feasible. In addition, the peak position of Pb(II) remains relatively constant at various concentrations. But it was observed a slight change for the peak of Cu(II).

7.3.4 Evaluation of Copper(II) and Lead(II) Mutual Interference

We observed differences in terms of sensitivity when we compared individual with simultaneous analysis. For the individual detection of Cu(II) and Pb(II), the sensitivities of Cu(II) and Pb(II) were 4.68×10^{-6} A$\cdot mM^{-1}$ and 3.00×10^{-5} A$\cdot mM^{-1}$ from Section 7.3.1 and 7.3.2. However, for the simultaneous analysis of Cu(II) and Pb(II), the sensitivities obtained were 7.60×10^{-6} A$\cdot mM^{-1}$ and 2.61×10^{-5} A$\cdot mM^{-1}$ from Section 7.3.3. We also found that the sensitivity of Pb(II) changed slightly, whereas the sensitivity of Cu(II) obviously increased.

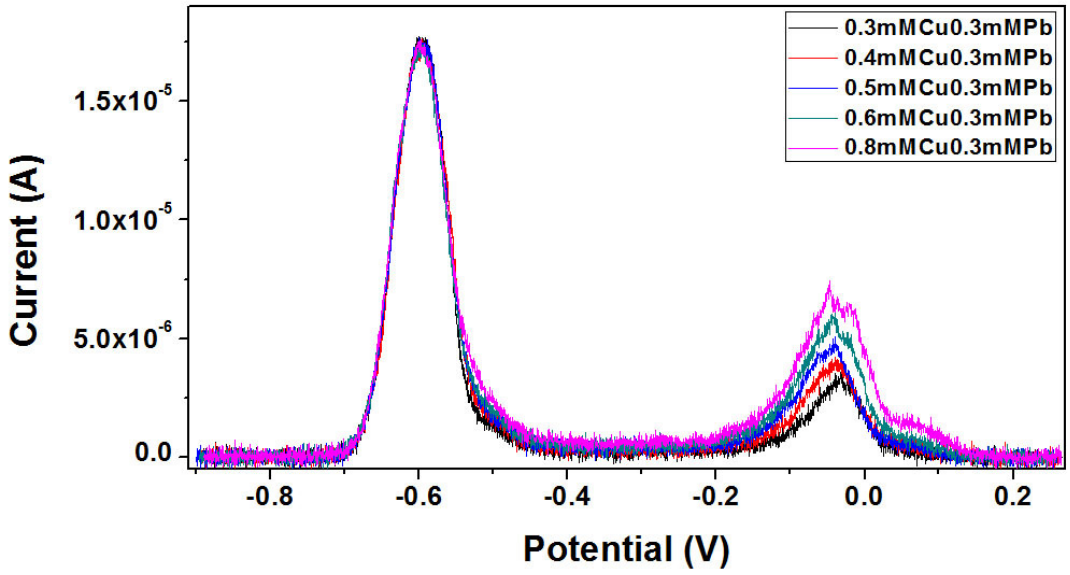

Figure 44. SWV response of 0.3 mM, 0.4 mM, 0.5 mM, 0.6 mM, and 0.8 mM Cu(II) in the presence of 0.3 mM Pb(II) in 0.1 M acetate buffer (pH 4.7), demonstrating the interference of the concentrations of Cu(II) on the peak current of Pb(II).

For a better understanding of the differences in sensitivity for Cu(II) and Pb(II) during the simultaneous analysis, the effect of the concentrations of Cu(II) on the

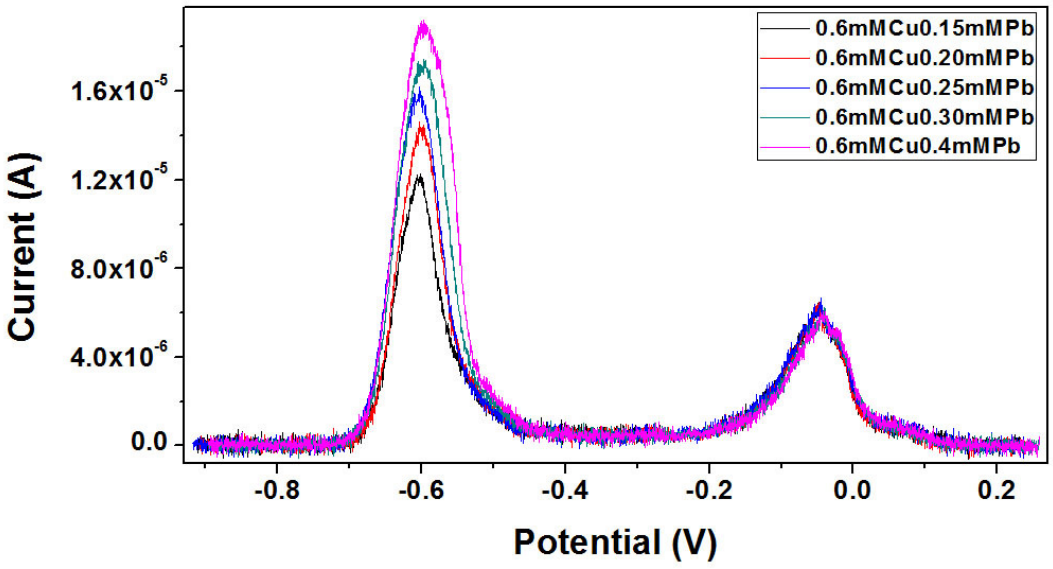

Figure 45. SWV response of 0.15 mM, 0.2 mM, 0.25 mM, 0.3 mM, and 0.4 mM Pb(II) in the presence of 0.6 mM Cu(II) in 0.1 M acetate buffer (pH 4.7), demonstrating the interference of the concentrations of Pb(II) on the peak current of Cu(II).

current peaks of Pb(II) and the effect of the concentrations of Pb(II) on the current peaks of Cu(II) were further studied. Fig. 44 shows the SWV responses at varying concentrations of Cu(II) in the presence of 0.3 mM Pb(II). The interference of the concentrations of Cu(II) on the Pb(II) was observed. As the concentration of Cu(II) increases, the current peaks of Pb(II) remain relatively constant. Similarly, we investigated the SWV responses at different concentrations of Pb(II) in the presence of 0.6 mM Cu(II) in Fig. 45. When the concentration of Pb(II) increases, slight shifts in the current peaks of Cu(II) were observed. This may indicate mutual interferences result from the formation of Pb-Cu intermetallic compounds Wei et al. 2012. Therefore, simultaneous detection of Cu(II) and Pb(II) ions is possible by using our measurement system.

7.4 Conclusion

In this chapter, we described a simple, low-cost SWV measurement device. Our instrument consists of a square wave relaxation oscillator, a triangle wave relaxation oscillator and a potentiostat. To verify performance of the device, the selective and simultaneous SWV detections of Cu(II) and Pb(II) were performed. Due to simplicity of use and cost, this system provides a practical alternative for electrochemical analysis.

Chapter 8

CMOS LIGHT-DIRECTION DETECTION SENSOR

This chapter presents an on-chip optical sensor capable of detecting the direction of incident light. No off-chip optical or mechanical components or modifications, for example, baffles, slit structures, mirrors, etc. are needed. The sensor was implemented in a standard 0.5 μm CMOS process Hongyi Wang et al. 2013. The CMOS chip was designed in collaboration with Dr. Hongyi Wang. A pair of on-chip photodiodes separated by a metal "wall" (created by stacking all metal layers, contacts and vias available in the process) is used to detect the direction of the incident light. This metal stack "wall" creates on-chip shadowing to facilitate detection so the two photodiodes produce different amounts of photocurrent. A model for this device is presented. The analysis indicates that the ratio of the difference of these two currents to the larger of the two currents has a linear relationship with the angle of the incident light. Moreover, we also demonstrate this ratio is almost independent of the incident light intensity. Test results verify these two conclusions and show good sensitivity to the light direction and immunity to the light intensity. An accuracy of 1.6 degrees over a 100 degree range is achieved by the linear relationship.

8.1 Background

Light direction detection is essential in numerous applications including positioning solar panels, orienting solar thermal collectors, and spacecraft altitude determination Mohammad and Karim 2013. There are many methods introduced in the prior arts

Yamada et al. 1996; Amemiya and Miyake 1995; Hill 1993; Hegyi 1993 to address this problem. However, these methods require special off-chip mechanical and/or optical components, for example, a board with apertures Amemiya and Miyake 1995, one or more baffles Hill 1993, mirrors, etc. In addition, it is often necessary to have a relative long distance between the light window and the sensing devices so that the light can illuminate different sensors with varying directions. Modifications to standard processing add complexity in post-processing and make it difficult for the sensor to remain small volume and light weight. Furthermore previous publications are susceptible to high thermal drift coupled with sensitivity to the intensity of the incident light. The ratio to indicate the angle is often nonlinear Hegyi 1993 which affects the detection accuracy or makes it difficult to calculate the angle.

In this paper, we present a light direction detection sensor based on the most popular integrated circuit process, namely, the Complementary Metal Oxide Semiconductor (CMOS) process. The presented sensor does not need any other mechanical and optical components or post-processing. Utilizing CMOS allows integration of many complex integrated circuits, for example, amplifier, ADC (analog to digital converter), DSP (digital signal processing unit), memory, or even RF (Radio Frequency) circuits. A standard CMOS process provides ease of fabrication, low cost, small size and excellent reliability. Another significant feature of the presented sensor is that it produces a signal ratio with a linear relationship to the angle of the incident light. This ratio also has very good immunity to light intensity, which is very helpful for the angle calculation.

8.2 CMOS Sensor Structure

The presented sensor uses shadowing effect that is demonstrated in the following text to improve detection with respect to macroscale Pineda and Arredondo 2012 or MEMS S. Mobasser and C. Liebe 2003 implementations. The sensor consists of 50 basic cells connected in parallel. Fig.46 shows the structure of two basic cells. The essential feature of this sensor is created by stacking all metal layers, contacts and vias available in the process to create on-chip "walls" as optical baffles. Two identical photodiodes are located on opposite sides of the "wall". When the light comes from directly above of the "wall", the two photodiodes are illuminated equally and produce same currents. When the light comes from one side above the "wall", it blocks part of the light to the opposite photodiode which therefore produces less current than the other photodiode. The difference of these two currents depends on the angle of the incident light. It is possible to calculate the angle based on these two currents. A theoretical model is created to understand the mechanism and compared to our experimental results in this paper.

In Fig.46, θ is the angle between the light direction and the metal "wall", h is the height of the metal "wall". The length, width and depth of each photodiode cell are l, w, and v respectively. s is the length of the shadow region. In this design, $h = 5.6$ μm, $l = 6$ μm, $w = 80$ μm, $v = 0.3$ μm. D_{Li} and D_{Ri} are the left side and right side photodiodes respectively with subscript indicating different cells, $i = 1 - 50$. I_L and I_R are the currents of left and right photodiodes, respectively, and V_L and V_R are the voltages of left and right photodiodes. The schematic current sources shown alongside the diodes indicate the photocurrents generated by the corresponding photodiodes due to the incident light.

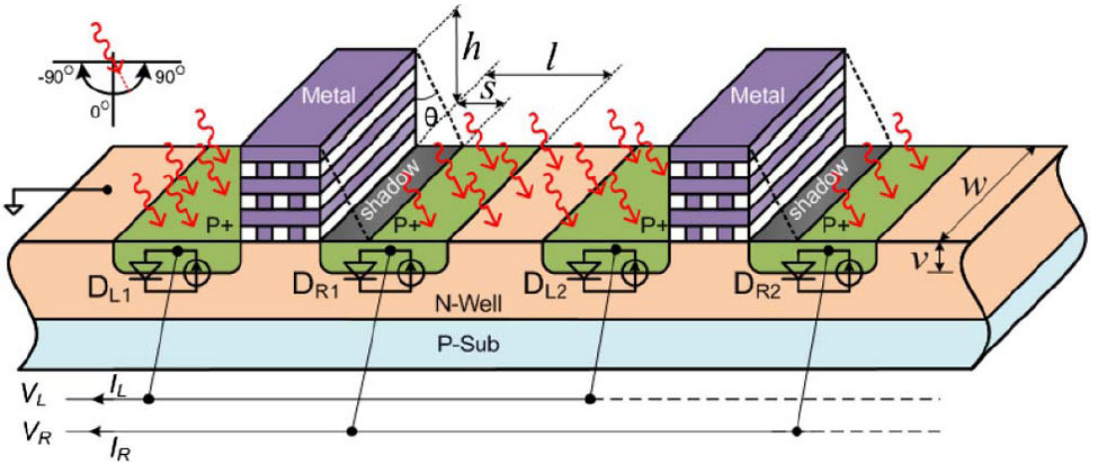

Figure 46. Structure of the proposed CMOS light direction sensor demonstrating the wall and its operation.

For simplicity in the derivation, Fig.47 shows the geometry of a basic cell within the sensor. OA and OB indicate the left side diode D_L and right side diode D_R in the basic cell. They have the same length, namely, $\overline{OA} = \overline{OB} = l$. l is also shown in Fig.46. OE is the metal "wall", and the arrows indicate the incident light. The angle between the metal "wall" and the light is the same θ shown in Fig.46.

Because the band gap voltage of silicon is 1.12 V, the longest wavelength of the light that the photodiode can absorb is 1.1 μm. The absorption peak is at about 0.7 μm of wavelength. On the other hand, the space between two metal walls in this design is 20 μm and the height of the wall is 5.6 μm, which are much larger than the wavelength of the absorbed light. Therefore the diffraction does not influence the derivation result significantly. To build a basic and simple model, it is not necessary to consider the diffraction effect. However, if a more accurate mode is needed or the size of wall and space are much small, the diffraction should be taken into consideration.

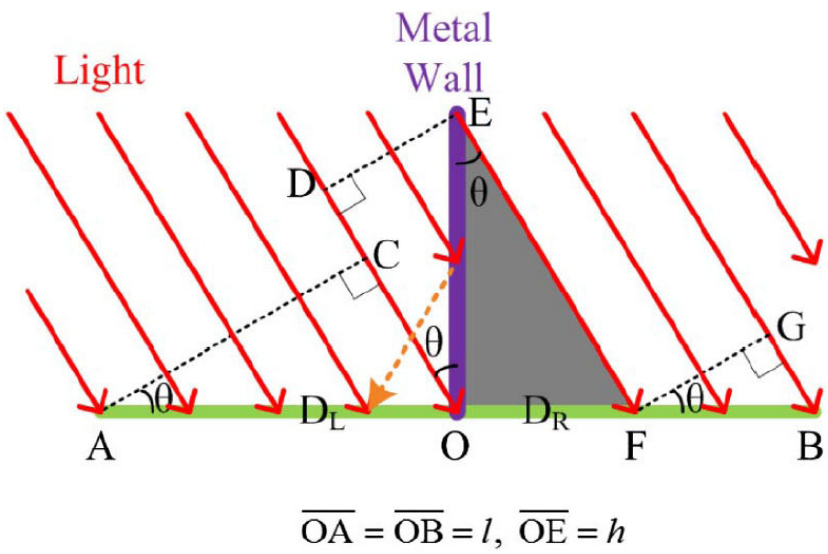

Figure 47. Diagram of the basic cell geometry for the light direction sensor.

8.3 Theory

As we know, a photodiode generates current proportional to the optical power it receives. The short-circuit photocurrent can be expressed as

$$I_{DIO} = kP_T = kP_0A_{EFF} = kP_0wL_{EFF} \tag{8.1}$$

Where, k is a constant coefficient, P_T is the total optical power the diode receives, P_0 is the incident optical power per unit cross-sectional area, A_{EFF} and L_{EFF} are the effective area and effective length of the incident light to illuminate diode, w is the width of the diode, which is shown in Fig.46.

Here we examine the case where the left diode is fully illuminated and the right diode is partly shadowed by the metal "wall". If the light comes from right side, a similar result can be achieved. The case of zero incident light on any diode is not considered for brevity. In this case, the total photocurrent from the left diode D_L can

be considered as composed of three parts. The first part is the current generated by or proportional to the light which directly illuminates the diode. This part of current can be described as

$$I_{LD} = kP_0w \cdot \overline{AC} \tag{8.2}$$

The second part of current is generated by or proportional to the reflected light from the metal "wall" with only part of the light is reflected. We assume the ratio of the light reflected to the total light reaching the metal "wall" is α, so this part of photocurrent is

$$I_{LR} = \alpha kP_0w \cdot \overline{DE} \tag{8.3}$$

Since the light illuminating the diode wouldn't be completely absorbed initially, the residual light will be reflected many times by the back metal base, the metal layers, and the interfaces of different materials. So the third part of the photocurrent can be thought as the sum of all those currents produced by the background light. It can be considered to be proportional to the total incident optical power and approximately uniform in the left and right diode regions. So this current can be indicated as

$$I_{LB} = \beta kP_0w \cdot (\overline{AC} + \overline{DE} + \overline{FG})\frac{\overline{AO}}{\overline{AB}} = \beta kP_0w \cdot \overline{AC} \tag{8.4}$$

where β is another constant in this equation. Summing the three parts of the photocurrent, we can get the total photocurrent of the left diode as

$$I_L = I_{LD} + I_{LR} + I_{LB} = kP_0w[(1+\beta) \cdot \overline{AC} + \alpha \cdot \overline{DE}] \tag{8.5}$$

Considering the incident light angle θ in Fig.47, we can rewrite the Eq. (8.5) as Eq. (8.6)

$$I_L = kP_0w[(1+\beta)l \cdot \cos\theta + \alpha h \cdot \sin\theta] \tag{8.6}$$

Similarly, the photocurrent from the right diode can be considered to include two parts. They are similar to the first and third parts of the photocurrent from the left photodiode. The total current of the right side diode can be described as,

$$I_R = kP_0w[(1+\beta)l \cdot \cos\theta - h \cdot \sin\theta] \tag{8.7}$$

In order to calculate the angle of the light, we defined a variable as the ratio of the difference of the two currents to the larger current, namely

$$R_{D/B} = \frac{|I_L - I_R|}{Max(I_L, I_R)} \tag{8.8}$$

Substituting Eq. (8.6) and Eq. (8.7) into Eq. (8.8) and considering the light comes from the left side as we assumed, we find

$$R_{D/B} = \frac{I_L - I_R}{I_L} = \frac{(\alpha+1)h \cdot \sin\theta}{(1+\beta)l \cdot \cos\theta + \alpha h \cdot \sin\theta} \tag{8.9}$$

As mentioned above, h and l are both constants for a given fabrication process and design. α and β depend on the process, layout and package, and they are assumed to be constant in a given design. In the later section of this paper, α and β will be determined by fitting this equation to the test data. We can see this assumption is reasonable and gives good accuracy over the useful angle range. From Eq. (8.9) we can see the ratio $R_{D/B}$ is independent of the light intensity and only depends on the incident light angle θ. This was verified through empirical results.

From Eq. (8.9), although $R_{D/B}$ does not have a simple relationship to the incident light angle, but with advanced analysis we find an exciting result. Based on the design parameters in this design, we can give some values for α and β and plot $R_{D/L}$ curves according to Eq. (8.9). Some of these curves are shown in Fig.48. We can see $R_{D/L}$ has an approximately linear relationship with the incident light angle over a range of $\alpha = 0.7 - 0.95$ and $\beta = 0.5 - 0.9$. We have also verified the linearity with

the $\alpha = 0.1, 0.2, ..., 0.9$ and $\beta = 0.1, 0.2, ..., 0.9$. This linear relationship allows us to calculate the angle in a very simple way.

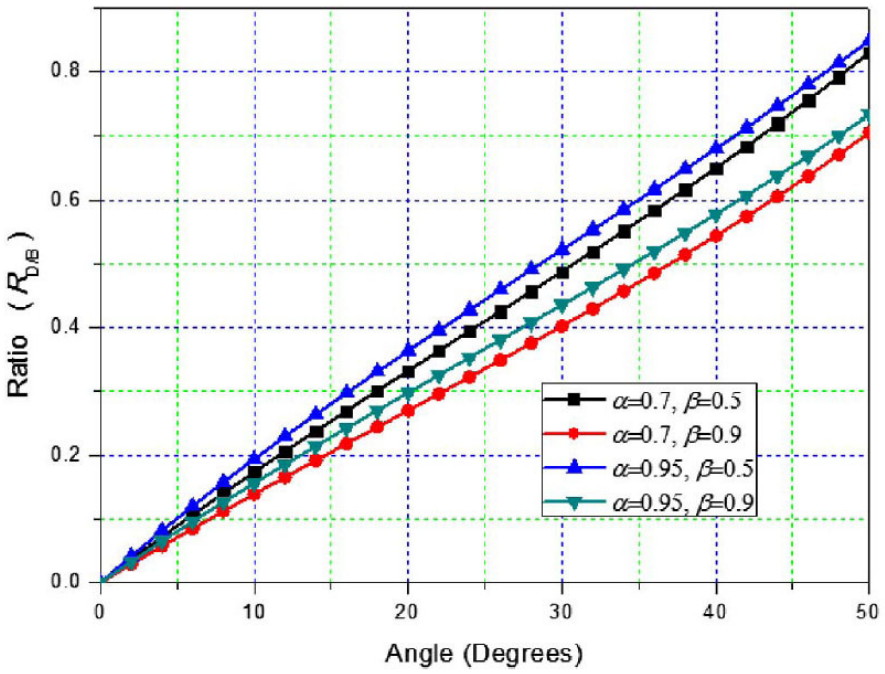

Figure 48. Curves for $R_{D/B}$ at different α and β versus incident light angle according to Eq. (8.9)).

8.4 Results and Discussion

We designed and fabricated this sensor in a standard 0.5 μm CMOS process. In Fig.49, the photomicrograph of the sensor is illustrated. The sensor in this design has 50 basic cells connected in parallel with a total size of only 0.11 mm^2.

Fig.50 shows the test results for the sensor with short-circuit photocurrents (top) and the ratio $R_{D/B}$ (bottom) v.s. optical power at different incident light angles.

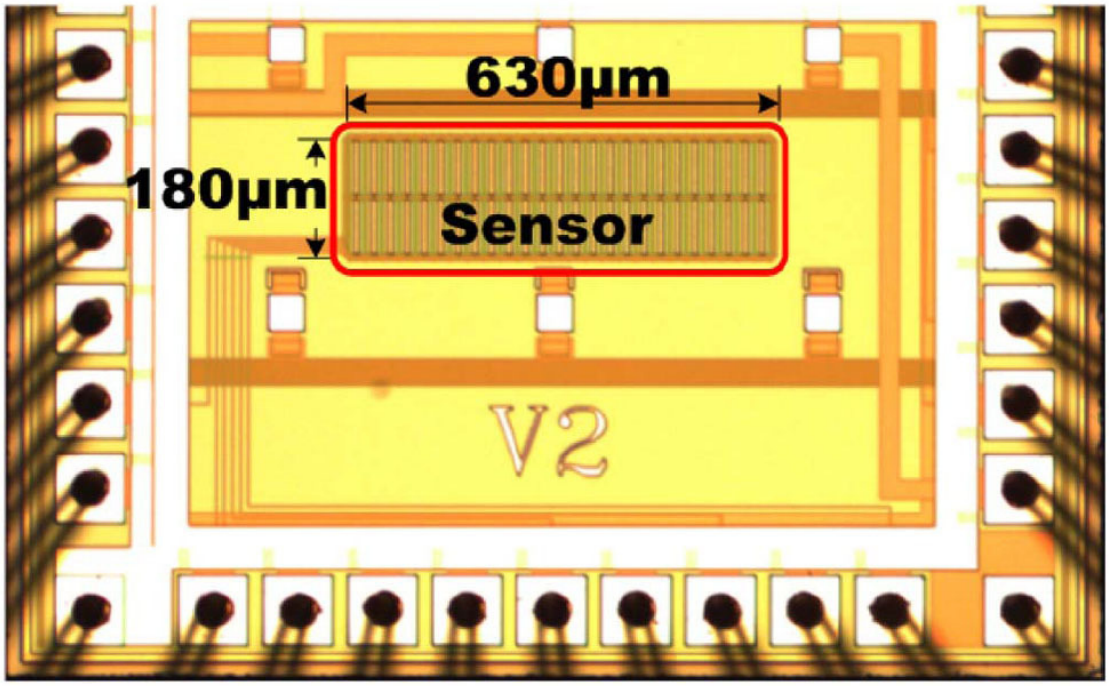

Figure 49. Photomicrograph of the presented light direction sensor based on a standard 0.5 μm CMOS integrated circuit process.

$R_{D/B}$ was calculated based on the short-circuit photocurrent and Eq. (8.8) separately. It is clear from the Fig.50 that $R_{D/B}$ is almost constant over a wide range of the light intensities, which agrees with Eq. (8.9).

Fig.51 (top) shows the two photocurrents versus the incident light angle when the light intensity is a constant of 65 mW/cm^2. Fig.51 (bottom) includes $R_{D/B}$ calculated from the tested data, the linear fit of the tested $R_{D/B}$, and the calculated $R_{D/B}$ according to Eq. (8.9). This shows the $R_{D/B}$ values based on empirical results really have a very nearly linear relationship with the incident light angle. If we use a linear relationship to calculate the angles based on the tested ratio $R_{D/B}$, the maximum error is 1.6 degrees over a range of -50 to 50 degrees. On the other hand, if we calculated the angle based Eq. (8.9) with $\alpha = 0.79$ and $\beta = 0.73$, the maximum error

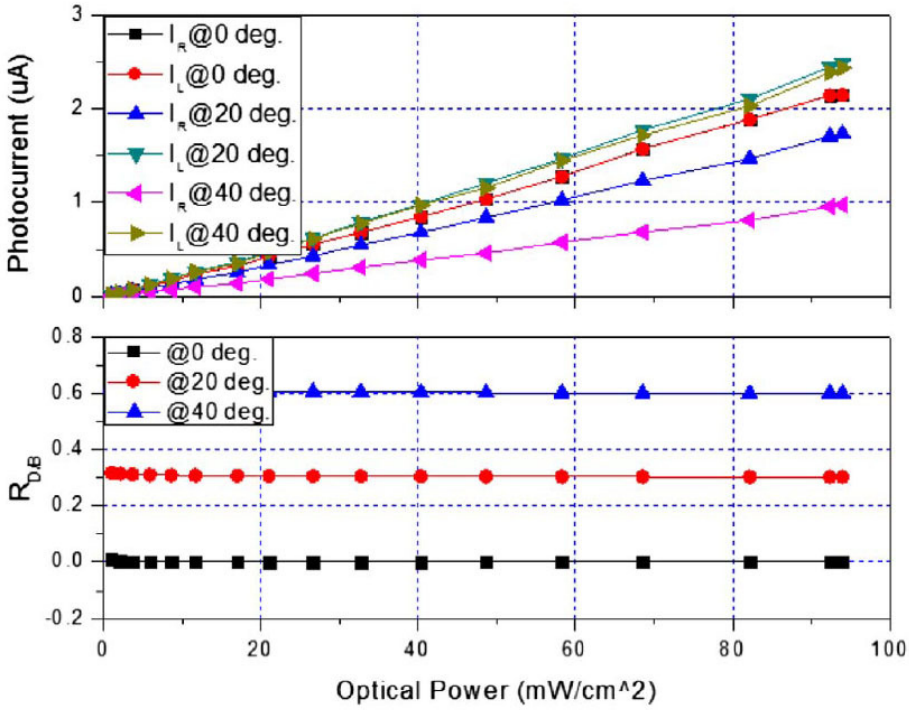

Figure 50. Short-circuit photocurrents (top) and the ratio $R_{D/B}$ (bottom) v.s. incident light intensity measured at different incident light angles.

is 2 degrees. All of these results verified the conclusions we derived from the model presented above.

Of course we can obtain better precision for the angle calculation through calibration, which is in fact quite simple with a commercial integrated circuits process. Signal processing circuits can be easily integrated in the same die. Additionally, designing a two-dimensional sensor would only require placing two sensors with a 90° angle between them to realize the two-dimension detection.

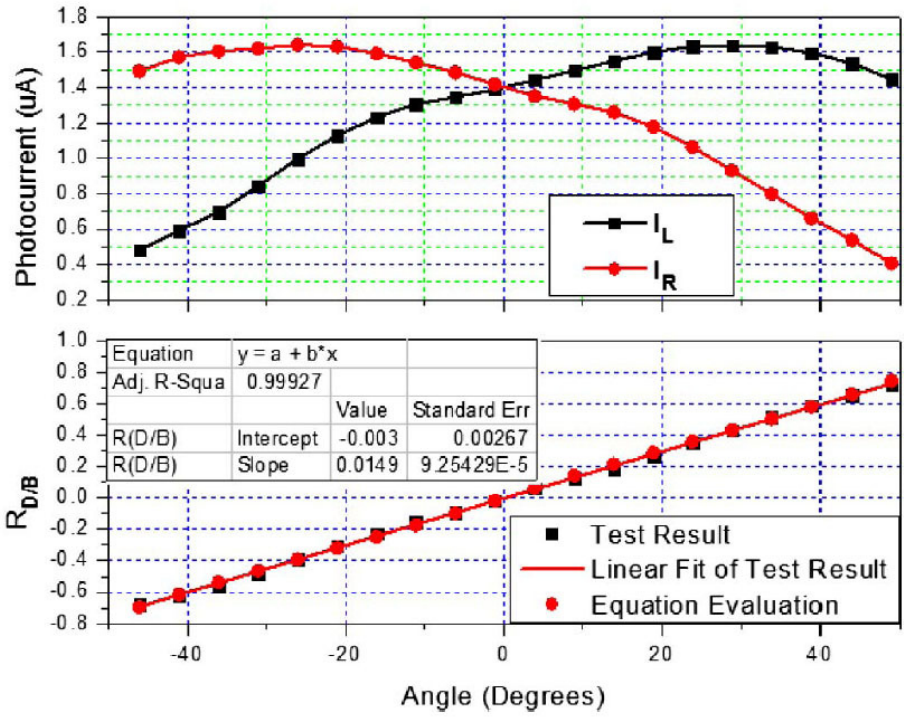

Figure 51. Photocurrents and ratio $R_{D/B}$ vs. light angle with a 65 mW/cm^2 incident light.

8.5 Conclusion

In summary, the on-chip light direction detection sensor is fabricated by the most popular IC fabricating process, CMOS, with a small area of 0.11 mm^2. It can be easily integrated with other integrated circuits, and no other special mechanical and optical post-processing or modifications are necessary for the presented sensor to work. Another significant feature of the presented sensor is that it can give a signal with a very linear relationship to the incident light angle. This makes it very convenient to evaluate the angle from this signal.

Chapter 9

A SELF-POWERED SENSOR WITH DIGITALIZED OUTPUT FOR LIGHT DIRECTION

This chapter presents a novel self-powered chip to detect the direction of incident light. This chip directly provides digitized output without the need of any off-chip power supply, optical or mechanical components. The chip was implemented in a standard 0.5 μm CMOS process Hongyi Wang et al. 2014. This chip was designed with Dr Hongyi Wang's help. Micro-scale metal baffle was created by stacking all metal layers, contacts and vias available in the process to produce on-chip shadowing. N-well/p+ photodiode arrays are located on both sides of the baffle to sense light. The photocurrent generated by a photodiode depends on the size of the photodiode and the shadowing. The shadowed area depends on the incident angle of the light. A current mirror circuit is used to compare the currents generated by the photodiodes on the opposite sides of the baffle and consequently, provide digital signal to indicate the incident light angle. Compared with the ideal linear digital light angle detector with the same resolution, the presented sensor achieved the maximum error of only 2 degrees over 110 degree test range.

9.1 Background

Low-power design is increasingly important in many fields, especially in a system where a battery is used as the power supply Fish, Hamami, and Yadid-Pecht 2006; Fish and Yadid-Pecht 2008. Many investigators are focused on finding solutions for

this topic. One solution is the technique of energy harvesting Law, Bermak, and Shi 2011; Ay 2011, absorbing energy from local environment to power a device. On the other hand, it is often necessary to detect the direction of the incident light; these applications include spacecraft attitude control Sohrab Mobasser and C. C. Liebe 2004, solar energy collection C.-Y. Lee et al. 2009, and motion detection Mousazadeh et al. 2009. Most methods introduced in the previous articles C.-Y. Lee et al. 2009; Pissavin et al. 1997 require off-chip mechanical and/or optical components such as boards with apertures C.-Y. Lee et al. 2009, baffles Pissavin et al. 1997, mirrors C.-Y. Lee et al. 2009, etc. In addition, these methods often need a relatively long distance between the light window and light sensing devices so that the light can illuminate different sensors in different directions. In this paper, we present a self-powered CMOS digital sensor to detect the light direction. It does not need power supply, further mechanical, optical components or post-processing. An NMOS current mirror circuit is designed to convert the angle information into digital output. Compared with the ADC circuit used in El Gamal, Yang, and Fowler 1999, the current mirror circuit is much more simple and robust. The standard CMOS process provides ease of fabrication, low cost, small size, and excellent reliability.

9.2 Sensor Structure

The presented sensor uses a vignetting effect Catrysse, Liu, and El Gamal 2000; Hongyi Wang et al. 2013 that is demonstrated in Fig.52 to improve detection with respect to macroscale Pineda and Arredondo 2012 or MEMS S. Mobasser and C. Liebe 2003 implementations. Compared with the original idea introduced in Hongyi Wang et al. 2013, this chip has a novel self-powered structure with photodiode arrays as the

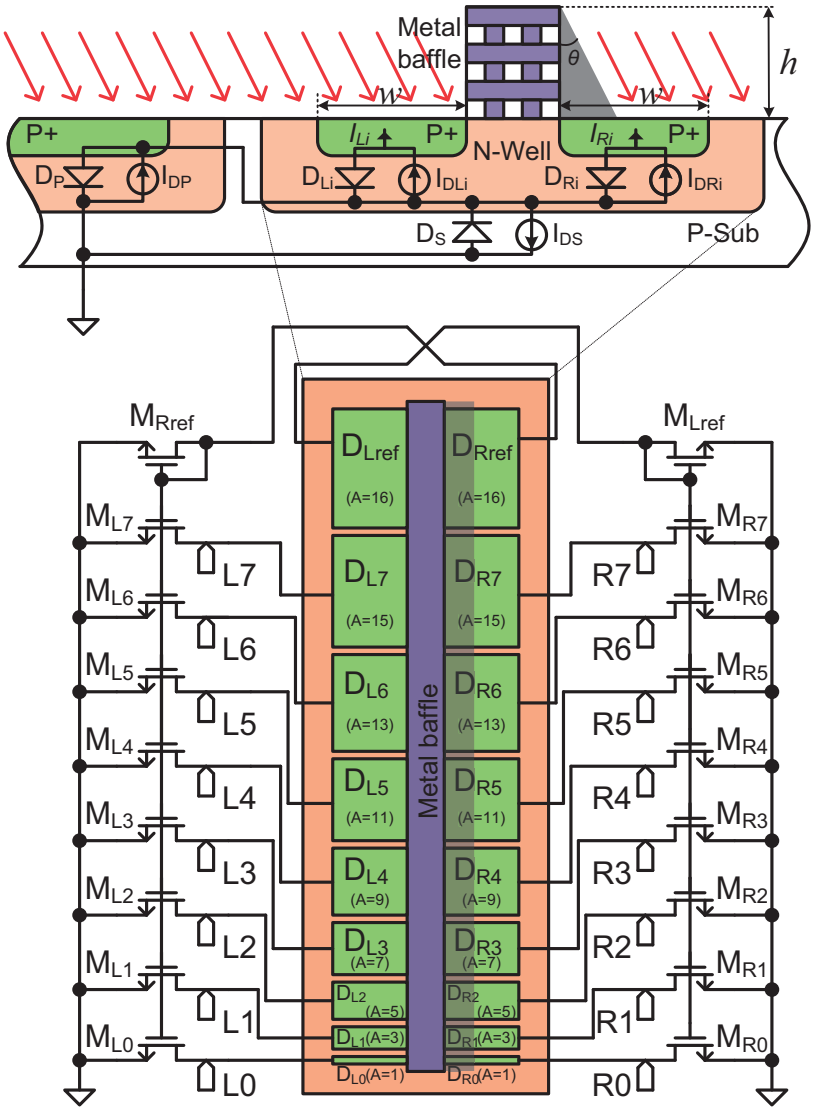

Figure 52. Structure of the proposed CMOS light direction sensor shown in cross-section with shadowing by the metal baffle (top) and the current mirror circuits used to achieve digital output (bottom).

light sensor and a current mirror circuit as the signal processing unit. The top part in Fig.52 is a cross-section of the sensor. A metal "wall" created by stacking all metal layers, contacts and vias available in the process acts as an on-chip optical baffle.

Two identical photodiodes D_{Li} and D_{Ri} are placed on opposite sides of the baffle. The schematic current sources shown beside each diode indicate the photocurrents generated by the corresponding photodiodes. When light comes from directly above of the baffle, the two photodiodes are illuminated equally and produce equal currents. When light comes from one side above the baffle, the baffle blocks part of the light to the opposite photodiode which therefore produces less current than the other photodiode. The difference of these two currents depends on the incident angle of the light.

9.3 Principle of Operation

To design such a sensor with good performance, it is important to optimize the dimensions of the metal wall and the photodiodes. It is obvious that the higher the metal wall is, the bigger the produced shadow difference in case of a certain angle change. So, it is usually reasonable to make the metal wall as high as possible to enhance the sensor's sensitivity. In this chip the height h of the wall is about 4.6 μm, which is determined by the used process. The width of the photodiodes is chosen according to the range of the light angle to be detected. In this design, the width w of all photodiodes is 6 μm. Therefore the maximum angel θ_{max} that can be effectively detected is given by Eq. (9.1)

$$\theta_{max} = arctan(w/h) \tag{9.1}$$

An angle exceeding θ_{max} will result in worse sensitivity because the photodiode on one side is completely shadowed. Substituting w and h into Eq. (9.1), we know that θ_{max} is about 53 degree in this design. The test range should not be too wide for it will decrease the sensitivity. There is a trade-off between the test range and the sensor's

sensitivity. The width of the metal wall is not critical. Therefore, several rows of vias and contacts were laid in a staggered pattern in order to block the light and to meet the design rules(e.g. metal density, via/contact space and etc.)

Diffraction is often an important factor to be considered when one designs a optical sensor. Considering the bandgap voltage of silicon is 1.12 V, the longest wavelength of the absorbed light is about 1.1 μm. Actually, the absorption peak is around 0.7 μm. However, in this design the space between two adjacent metal walls is 20 μm, and the height of the wall is 5.6 μm, which are all much larger than the wavelength of the absorbed light. Thus the diffraction does not influence the sensor's performance significantly.

In order to generate a digital signal related to the light angle, two identical photodiode arrays are located on opposite sides of the baffle. The diodes in each array have the normalized areas of $16, 15, 13, 11, 9, 7, 5, 3$, and 1, respectively. The smallest diode D_{L0} or D_{R0} with the normalized area of 1 is composed of 12 basic cells. Each basic cell has a size of $6\mu m \times 60\mu m$. The photocurrents of D_{Lref} and D_{Rref} flow into diode-connected NMOSs, M_{Lref} and M_{Rref}, respectively. They produce two gate bias signals for M_{R0-7} and M_{L0-7}. Each of the other photodiodes is connected to the drain of an NMOS. All the NMOSs in Fig.52 have identical sizes.

If the examined light comes from the left side, the left diodes are fully illuminated and the right diodes are partly shadowed due to the metal baffle. The case of zero incident light on any diode is not considered for brevity. If the photocurrent generated by D_{Li} is larger than the photocurrent generated by D_{Rref}, the voltage of node Li will be high. Otherwise, it will be low. The subscript i indicates different photodiodes, $i = 0 - 7$. The farther left the light comes from, the wider the shadow on the right side, and the less the photocurrent in D_{Rref}. Then the smaller photodiode on the left

side can produce a photocurrent larger than that produced by D_{Rref}. As a result, there will be more Li nodes with high voltage level.

Similarly, the farther right the light comes from, the more Ri nodes will be high. If the light comes from directly above the baffle, All the Li and Ri are low. So the number of high voltage level Li or Ri indicates the angle of the incident light. The circuit actually has thermometer code output which is similar to a Flash ADC.

In order to make the current mirror work well, the photocurrent produced by D_{Lref} is assumed to completely flow into M_{Lref}, and that of D_{Rref} into M_{Rref}. That means the threshold voltage of NMOS, V_{thn} should be lower than the forward conduction voltage of the photodiode. This forward voltage is about 0.6 V. This requirement can be fulfilled by a low threshold NMOS process. However, the V_{thn} in the used 0.5 μm CMOS process is about 0.7 V. That is too high to be turn on by the photodiode generated voltage. To solve this problem, we used another photodiode D_P to boost the potential of the common N-well of the photodiodes (Fig.52). In this case, the photocurrent I_{DP} needs to be larger enough to support the sum of I_{DLi}, I_{DRi} and I_{DS}. I_{DS} is the current generated by the big N-well/P-sub photodiode D_S. To keep costs to a minimum, we used three of the same chips for verification. One is the main chip, and the other two auxiliary chips connected in parallel are used as a big enough D_P. That is shown in Fig.53.

As we know, the threshold voltage V_{thn} changes with the temperature and the process corner. Fortunately, V_{thn} and V_{Dio} have same changing tendency with the temperature, which is helpful to keep the current mirror work. Considering the different process corners, it would be better to use low threshold process for this design. In order to achieve a good accuracy, the current mirror circuit should be paid

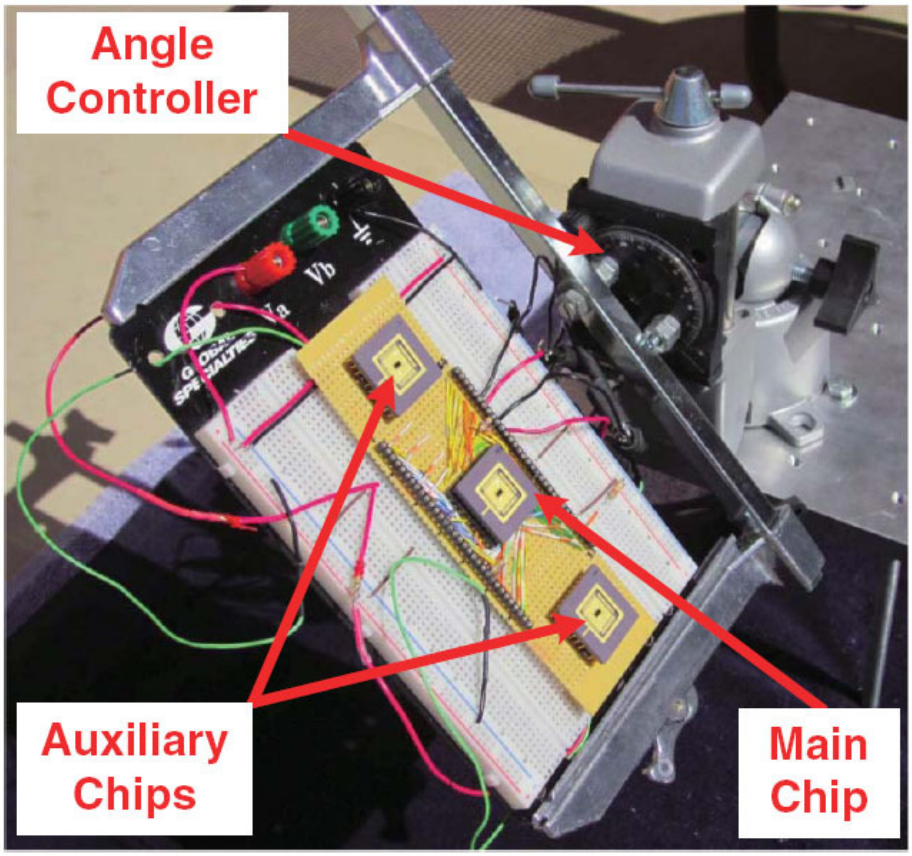

Figure 53. Experimental setup for light-direction detection.

more attention to deal with the mismatch. Large size (W/L=20*4μm/4μm) NMOSs and common-center structure were used in the layout for this purpose.

Fig.54 shows the photomicrograph of the presented chip. It was fabricated in a standard 0.5 μm CMOS process. To improve the sensor's sensitivity, each photodiode shown in Fig.52 consists of a number of basic diode cells connected in parallel. The number is dependent on the area ratio. The current mirror circuit is located on the right side of the chip. It occupies a very small area and is shielded by a few metal layers to avoid light influence.

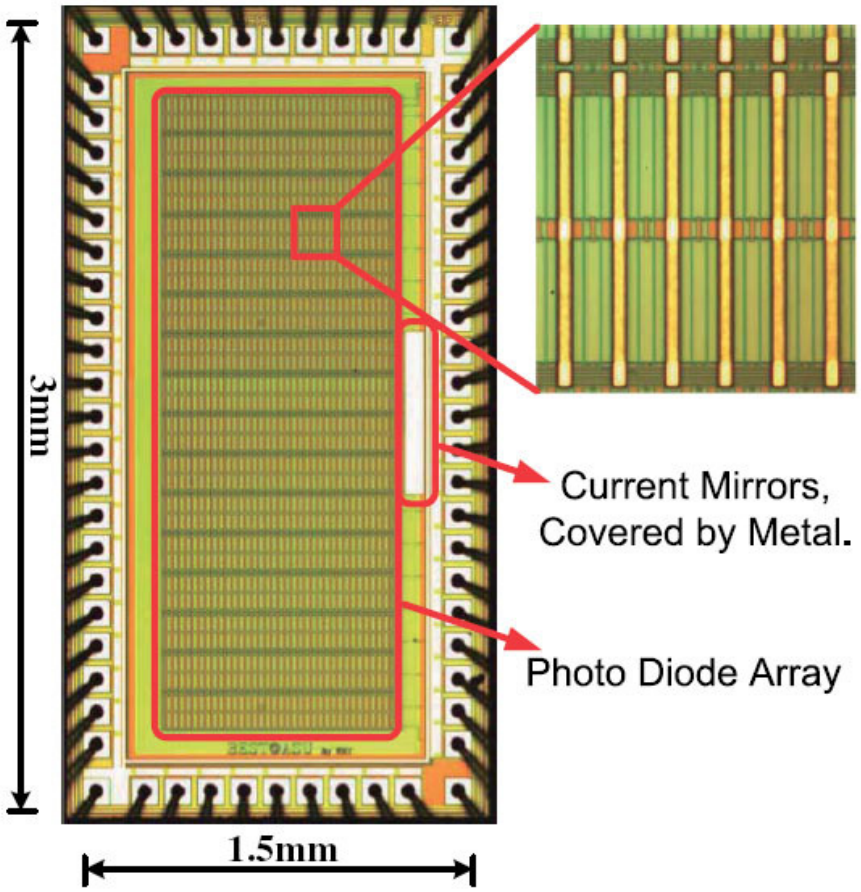

Figure 54. Micrograph of the presented chip.

9.4 Results and Discussion

To verify the photodiodes, we tested the short-circuit current of each diode at different angles. The results are shown in Fig.55. I_{Li} and I_{Ri} in the x-axis indicate the photocurrent of D_{Li} and D_{Ri}, respectively. It can be seen, for a given angle, the currents of different diodes have the same ratios as their area. That indicates all the photodiodes are functional.

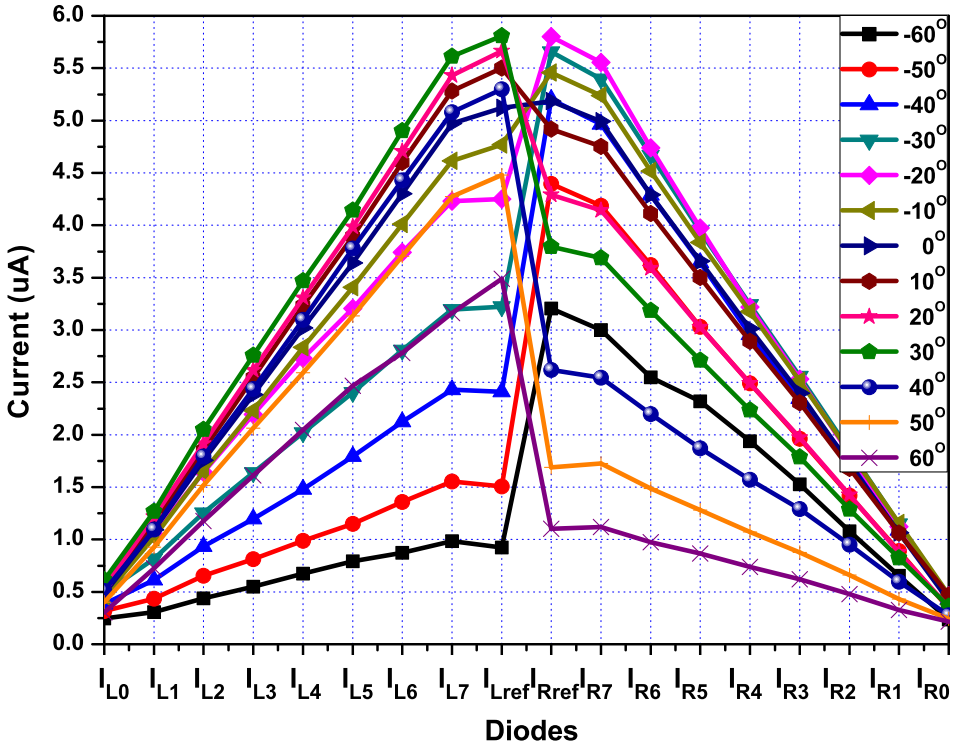

Figure 55. Photocurrents of each diode at different angles under sunlight with light intensity of 85 mW/cm^2.

The digital outputs of the chip were measured under sunlight by a 4-channel oscilloscope repeatedly to get all the output signals (Fig.56). The outputs $L0 - L7$ and $R0 - R7$ change with varying angles. Without a power supply, the output voltage of the chip can range from 0 V to 0.9 V. $R0$, $R1$, and $L0$ did not change their states because the photocurrents of D_{RO}, D_{R1}, and D_{L0} could not be larger than the photocurrent generated by D_{Lref} and D_{Rref} due to the background noise. However, in Fig.56 we can see the digital output has a nearly linear relationship with the incident angle of the light, which is in accord with the theory derived in Ref Hongyi Wang et al. 2013. To verify this, we convert the digital output into a decimal form and plot it in Fig.57. An ideal theoretical result is also shown in Fig.57. The ideal theoretical

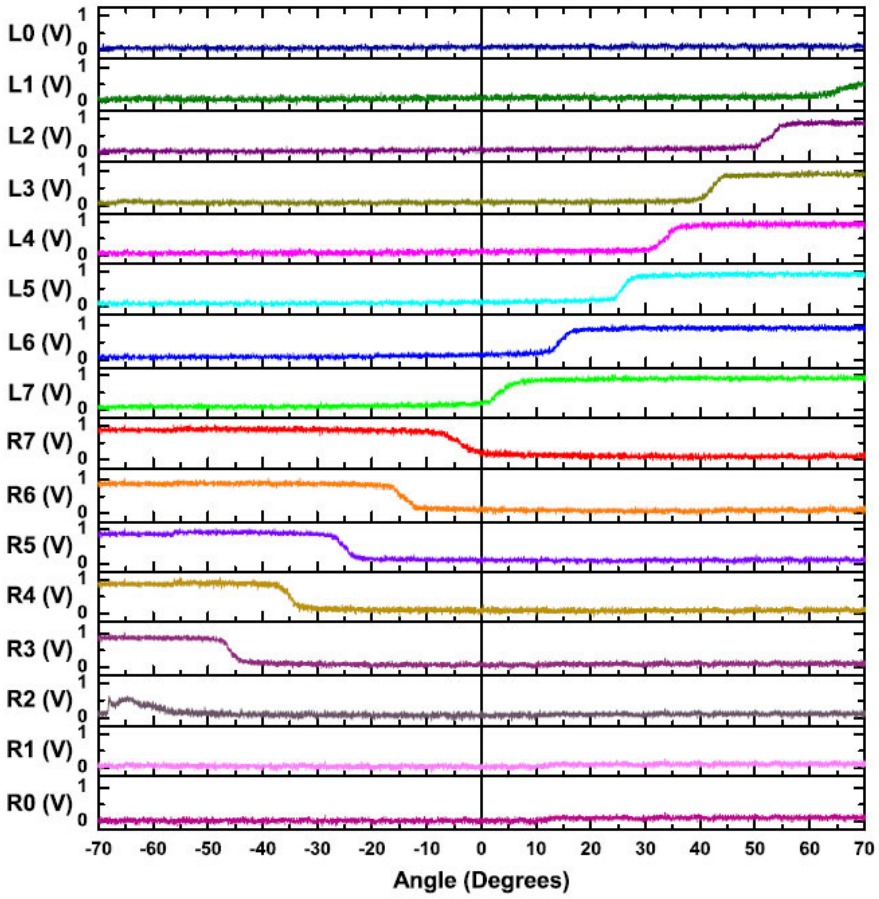

Figure 56. Outputs of the flash ADC versus the angle of the incident light.

result is derived from a linear digital light angle sensor with the same test range of 110 degrees and same resolution of 10 degrees. Comparing these two curves, we can see the maximum difference between these two series of transition points is only 2 degrees over the range from -50 to 60 degrees. Therefore, it is excepted that based on this structure and a bigger array with more different size of photodiodes, it is feasible to design a new sensor with resolution and accuracy less than 2 degrees over the range of 110 degrees (i.e., a 5.5 bit of light-angle-to-digital conversion resolution).

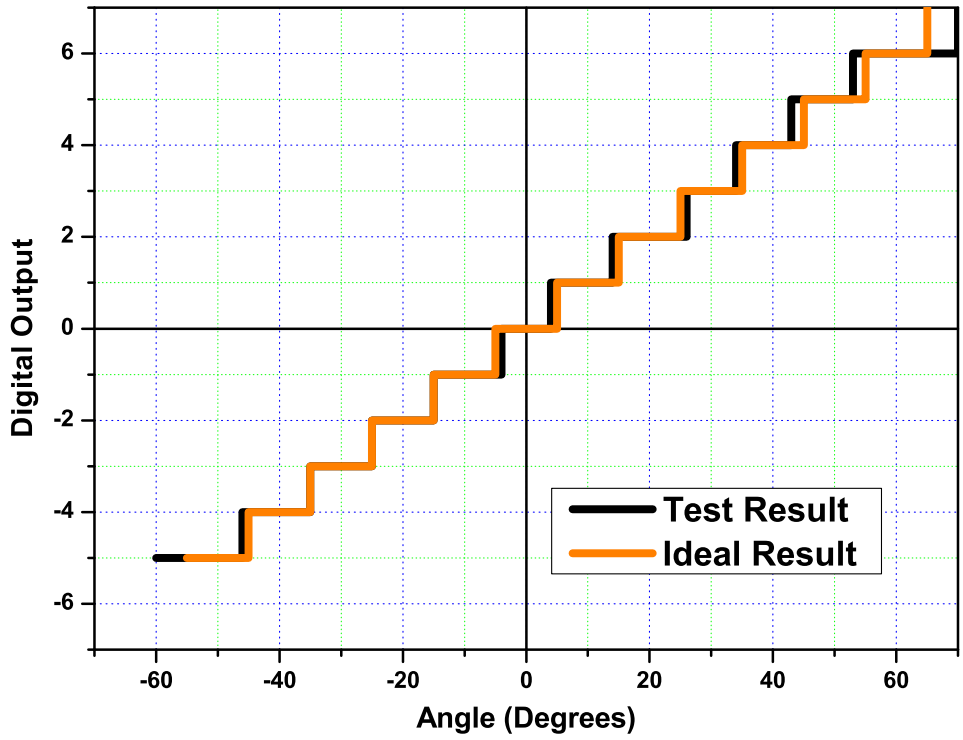

Figure 57. Comparison of the tested outputs with the ideal output of the self-powered ADC.

9.5 Conclusion

In this chapter, a self-powered on-chip sensor with digitalized output for light direction detection is demonstrated. Fabricated in a standard 0.5 μm CMOS process, all the metal layers, contacts and vias in the process are stacked as an optical baffle to create on-chip shadowing. Two arrays with various sizes of photodiodes are located on the opposite sides of the baffle to act as the light sensors. A simple current mirror circuit compares the photocurrents and provides digital output to indicate the incident light angle. Test Results show an error of only 2 degrees can be achieved compared with the ideal output. The digital output has voltage level range of 0 V to 0.9 V, and the detected angle range is from -50 to 60 degrees.

Chapter 10

A SUN TRACKER WITH AN ON-CHIP SENSOR

This chapter demonstrates a self-powered Maximum Power Direction Tracking (MPDT) system capable of maximizing the energy harvesting by automatically adjusting the angle of the solar panel Hongyi Wang et al. 2015. The whole system is powered by a solar panel so no extra power supply is needed. The entire system consists of a solar panel, a motor, and a CMOS chip. A novel light direction sensor and the needed circuit are integrated in a single chip which is fabricated by a standard 0.5 μm CMOS process. Thus, it is small-size and low-cost. The system was tested to verify performance with different light direction and intensity. The results show that the system has good sensitivity to the incident angle and achieve tracking accuracy of $\pm$1.8 degrees over a optical power range of 30-110 mW/cm^2. This work is in collaboration with Dr Hongyi Wang.

10.1 Background

In a variety of applications, we usually need a tracking system to get maximum solar panel output power. For example, it is used in the spacecraft power system to improve the energy harvesting efficiency and also used for the spacecraft attitude determination Liebe and Mobasser 2001; Deans, Wettergreen, and Villa 2005; Delgado et al. 2012. Many of these applications require low power, low cost, small size, and light weight. Miniaturized on-chip sensor is an attractive choice to meet these requirements. That make it easy to integrate complex circuits in a same chip, to improve the

reliability, and to cut down the cost. In this case, it is necessary to have an on-chip light direction sensor for this system. Many techniques have been developed to detect sun or light direction, such as the shading device method Quero et al. 2001, the tilted surface method Karimov et al. 2005; Koyuncu and Balasubramanian 1991, and the collimator tube method Mousazadeh et al. 2009. However, for the shading method, not only the achieved accuracy of ± 10 degrees is lower than the tilted surface method and collimator tube method, but also its light sensitivity is low compared with the other two methods. For the tilted surface method, it requires special off-chip optical components, for example, light dependent resistors (LDR). Which make it impossible to realize it on a chip. Although the accuracy of the collimator tube method is high, the detection range is relative small i.e. 1 degree and its size is large. It is also difficult to make this sort of sensor small-volume and light-weight.

This chapter presents a self-powered maximum power direction tracking system, which consists of a motor, a solar panel, and a CMOS chip with a light direction sensors and the signal processing circuits. Most of the circuits are integrated on the same chip to process the sensing signal and control the motor. Because batteries are expensive, bulky and require replacement and disposal, many ways to recharge or replace them are being researched Sarkar and Chakrabartty 2013; Guan and Liao 2005; Dong et al. 2007. To overcome this problem, a solar panel is used to power the sensor chip and the motor driver, which means this system is completely self-powered.

10.2 Sensor Design

In this chapter, an on-chip CMOS sensor is designed to detect the incident light direction so as to know the strongest light direction. Fig. 58 shows a basic cell of

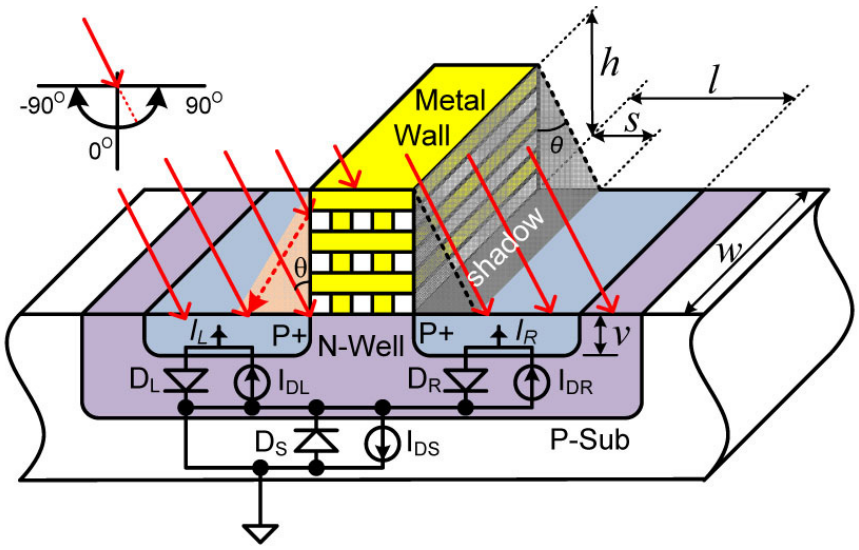

Figure 58. Structure of the proposed CMOS light direction sensor.

the sensor. The whole sensor is formed by a number of the basic cells. A metal wall created by stacking all metal layers, contacts, and vias available in the process is used to generate on-chip micro-scale shadow. The height of the metal wall is h. We should optimize the dimensions of the metal wall for the sensor's good performance. In this design, we choose 4.6 μm as the height of the metal wall.

In this design, diffraction has been considered. As we all know, the bandgap voltage of silicon is about 1.12 V. So the longest wavelength of the absorbed light is about 1.1 μm. Actually, the absorption peak is around 0.7 μm. However, in this design the distance between two adjacent metal walls is 20 μm, and the height of the mental wall is 4.6 μm. The physical dimensions are much larger than the wavelength of the absorbed light. So the diffraction has little influence on the sensor performance Hongyi Wang et al. 2013, 2014.

Two identical photodiodes are located on opposite sides of the metal wall. D_L is the left side diode and D_R the right side diode. They have same width w and

same length, l. The schematic current sources shown beside each diodes indicate the photocurrents generated by the corresponding photodiodes. The angle between the metal wall and the light direction is θ. When the light comes from directly above of the wall, namely $\theta = 0$, the two photodiodes are illuminated equally and produce same currents. When the light comes from one side above the wall, namely $\theta > 0$ or $\theta < 0$, the wall blocks part of the light to the opposite photodiode which therefore produces less current than the other photodiode. So the relationship between of I_{DL} and I_{DR} is relative to angle of the incident light. We can get more details by deriving the expressions of I_{DL} and I_{DR} as flowing.

As we known, the photocurrent generated by a photodiode is proportional to the optical power the photodiode receives. The short-circuit photocurrent can be written as

$$I_{DIO} = kP_T = kP_0A_{EFF} = kP_0wL_{EFF} \tag{10.1}$$

where, k is a constant coefficient, P_T is the total optical power the diode receives, P_0 is the optical power per unity sectional area of the light, A_{EFF} is the sectional area of the incident light, and L_{EFF} is the length of the sectional area.

Here, we analyze the case of $\theta > 0$. That means the left diode is fully illuminated and the right diode is partly shadowed by the metal wall. The case of zero incident light on any diode is not considered for brevity. In this case, the total photocurrent generated by the left diode D_L can be divided into three parts. The first part is the current generated by the light which directly illuminates the diode. According to Eq. (10.1) and the geometrical structure, this part of current can be described as

$$I_{LD} = kP_0wl\sin\theta \tag{10.2}$$

The second part of current is the current generated by the reflected light (Fig. 58) from the metal wall. Since only part of the light is reflected, we assume the ratio of

the light reflected to the total light reaching the left side of the metal wall is α. This part of photocurrent is expressed as

$$I_{LR} = \alpha k P_0 w h \sin\theta \tag{10.3}$$

Since the light illuminating the diode wouldn't be completely absorbed initially, the residual light will be reflected many times by the back metal base, the metal layers, and the interfaces of different materials. So the third part of the photocurrent can be thought as the sum of all those currents produced by these background lights. It can be considered to be nearly proportional to the total incident optical power and approximately uniform in the left and right diode regions. So this part of current can be indicated as

$$I_{LB} = \beta k P_0 w l \sin\theta \tag{10.4}$$

where, β is other constant in this equation. Summing the three parts of photocurrent, we can get the total photocurrent of the left diode as

$$I_{DL} = I_{LD} + I_{LR} + I_{LB} = k P_0 w \left[(1+\beta) l \cdot \cos\theta + \alpha h \cdot \sin\theta\right] \tag{10.5}$$

Similarly, the photocurrent generated by the right side diode can be considered to include two parts. They are similar to the first and third parts of the photocurrent generated by the left photodiode. The total current of the right side diode can be described as,

$$I_{DR} = k P_0 w (1+\beta) l \cdot \cos\theta - h \cdot \sin\theta \tag{10.6}$$

From Eq. (10.5) and Eq. (10.6), we can get the current ratio of I_{DL} and I_{DR} is,

$$\frac{I_{DL}}{I_{DR}} = \frac{(1+\beta) l \cdot \cos\theta + \alpha h \cdot \sin\theta}{(1+\beta) l \cdot \cos\theta - h \cdot \sin\theta} \tag{10.7}$$

In the other case, if the light comes from the right side, $\theta < 0$, the right side diode is completely illuminated and the left side diode is partly shadowed. We can get the

following result in a same way.

$$\frac{I_{DL}}{I_{DR}} = \frac{(1+\beta)l \cdot \cos\theta + h \cdot \sin\theta}{(1+\beta)l \cdot \cos\theta - \alpha h \cdot \sin\theta} \tag{10.8}$$

Eq. (10.7) and Eq. (10.8) can be combined together as Eq. (10.9),

$$f(\theta) = \frac{I_{DL}}{I_{DR}} = \begin{cases} \dfrac{(1+\beta)l \cdot \cos\theta + \alpha h \cdot \sin\theta}{(1+\beta)l \cdot \cos\theta - h \cdot \sin\theta}, & \theta \geq 0 \\ \dfrac{(1+\beta)l \cdot \cos\theta + h \cdot \sin\theta}{(1+\beta)l \cdot \cos\theta - \alpha h \cdot \sin\theta}, & \theta < 0 \end{cases} \tag{10.9}$$

As mentioned before, h and l are both constants when the device has been fabricated. α and β depend the process, layout and package. Their values could not be exactly estimated but they are reasonably assumed to be constant in a given design. Therefore, from Eq. (10.9) we can see the current ratio of I_L/I_R is independent on the light intensity and only depends on the incident light angle θ. This is a useful feature that means with a given I_L/I_R, the angle can be determined by

$$\theta = f^{-1}\left(\frac{I_{DL}}{I_{DR}}\right) \tag{10.10}$$

With this analysis result, it is possible to design a circuit to control the tracking system focusing on the sun with a certain angle error range under different light intensity.

10.3 Circuit Design

Fig. 59 shows the circuit of the tracking system. Photodiodes D_L and D_R and photocurrents I_{DL} and I_{DR} are same as shown in Fig. 58. The values of R_L, R_{R1}, R_{R2}, and R_{R3} can be selected to make the voltage V_L and V_R are much lower than the forward conductive voltage of the diodes D_L and D_R. Under this condition, almost all

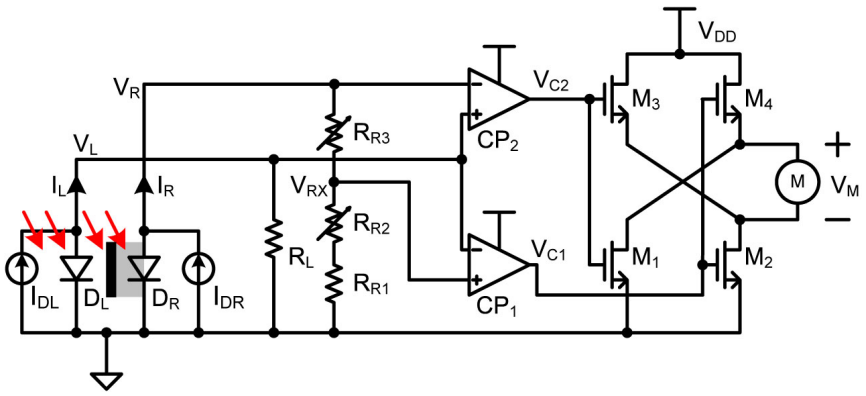

Figure 59. Block diagram of the proposed tracking circuit.

of the currents I_{DL} and I_{DR} flow into the resistors, namely, $I_L = I_{DL}$ and $I_R = I_{DR}$. So

$$\begin{cases} V_L = I_{DL} R_L \\ V_R = I_{DR}(R_{R1} + R_{R2} + R_{R3}) \\ V_{Rx} = I_{DR}(R_{R1} + R_{R2}) \end{cases} \tag{10.11}$$

There are two comparators CP_1 and CP_2 in Fig. 59. Both them are integrated in a same die with the light direction sensor. For the comparator CP_1, the flip point locates where its negative input and non-negative input equal to each other, $V_L = V_{Rx}$, namely

$$I_{DL} R_L = I_{DR}(R_{R1} + R_{R2}) \tag{10.12}$$

so,

$$\frac{I_{DL}}{I_{DR}} = \frac{R_{R1} + R_{R2}}{R_L} \tag{10.13}$$

From Eq. (10.10) and Eq. (10.13), the corresponding angle θ_1 for CP_1 flipping can be expressed as

$$\theta_1 = f^{-1}\left(\frac{R_{R1} + R_{R2}}{R_L}\right) \tag{10.14}$$

In the same way we can get the flip point for the comparator CP_2 is

$$\theta_2 = f^{-1}\left(\frac{R_{R1} + R_{R2} + R_{R3}}{R_L}\right) \tag{10.15}$$

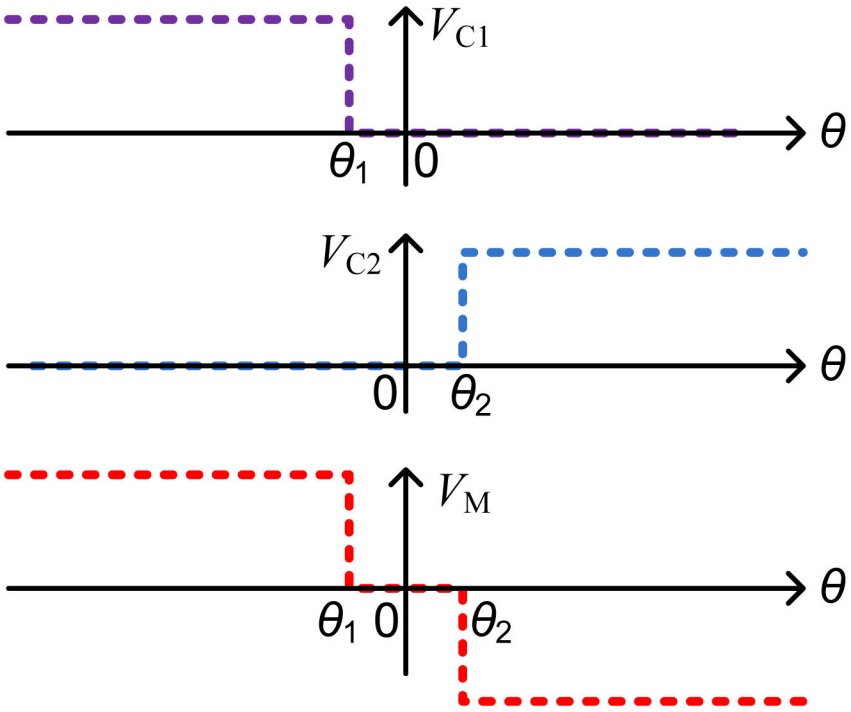

Figure 60. Curve of the tracking circuit.

From Eq. (10.14) and Eq. (10.15), we can see the two angle flip points are completely determined by the resistor ratio and irrelative to the light intensity. That provide easy to adjust this two angles θ_1 and θ_2 by turning the two adjustable resistor R_{R2} and R_{R3}. By proper values for R_{R2} and R_{R3}, the signal curves in Fig. 60 can be achieved.

It can be seen when $\theta < \theta_1$, the motor is driven by $V_M > 0$, the angle will increase. When $\theta > \theta_2$, the motor is driven by $V_M < 0$ and the angle will decrease. When $\theta_1 < \theta < \theta_2$, $V_M = 0$, the motor will be stationary and there will be no power consuming by the motor driver. That is the stable region. For the fixed-location

solar-cell to track sun application, the needed rotating speed is very slow, so most of the time this system stays in a very low power state, in which the motor driver does not consume power, and only the comparators continuously work. In this design, the consume current is only 88 μA. This is another significant feature for the low power applications.

The two comparators in Fig. 59 have the same circuit structure. The design details have been shown previously Luo et al. 2013. This comparator has a push-pull output stage. The driving ability can be bigger than 40 mA. At the same time, the quiescent current is only 44 μA as mentioned.

For a feedback loop, it is necessary to consider the stability issue. Since the mechanical stuff have inertia, the rotation movement always has an overshoot before it completely stop. For example, when the panel rotates from a more minus angle to θ_1, although the motor driving current is cut off very quickly, the rotating structure cannot stop immediately and will stop at a angle larger than θ_1. If this angle is beyond θ_2, the system will need to turn back. At the worst case, this turn back rotation stop at an angle less than θ_1 due to the inertia, thus an oscillation happens. This is the stability issue. An simple way used in this design to prevent oscillation is to set the stable range $(\theta_2 - \theta_1)$ larger than the maximum overshoot in the worst case.

In this design, all the circuit and the motor are powered by a solar panel. The resistors in Fig. 59 are discrete components for the facility to adjust the flip points of the comparators. For different applications, the driving currents of the motor are much different. So the motor driving MOSFETs M1-M4 also use discrete components.

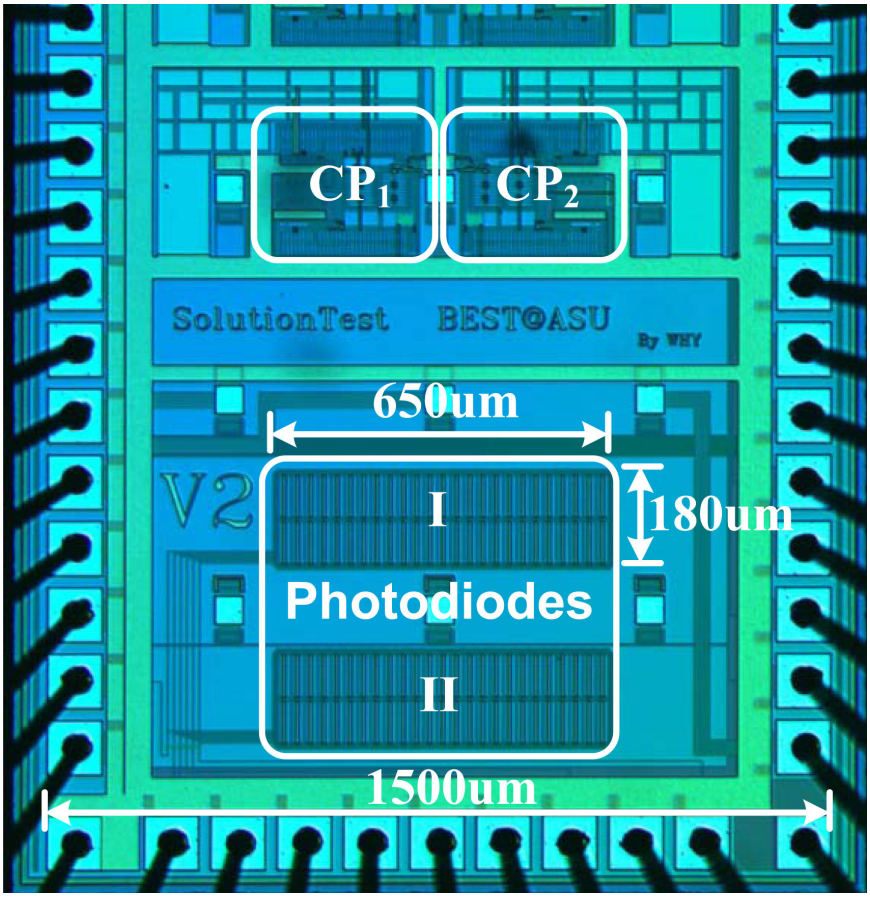

Figure 61. Microphotograph of the chip.

10.4 Implementation and Verification

Both the light direction sensor and the comparators are implemented in a same die by a 0.5 μm standard CMOS process. The microphotograph is shown as Fig. 61. The whole sensor consists of part I and part II. Each parts is composed of 50 basic sensor cells as shown in Fig. 58. All the basic cells are connected in parallel. The total area of the light direction senor is only 0.234 mm^2. For the chip also includes other circuit

not related to this tracking system, the other circuits are not be described in this chapter.

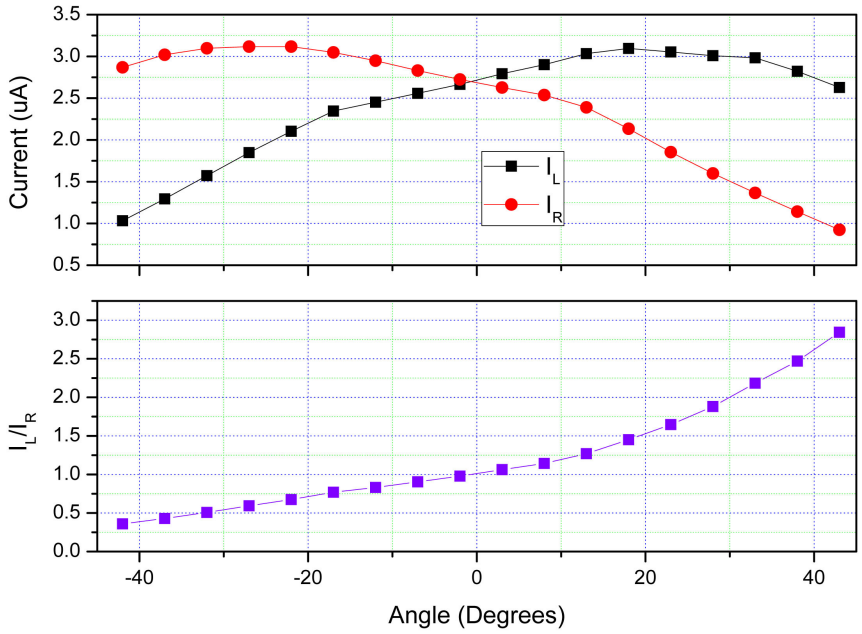

Figure 62. Currents and current ratio of the photodiode versus the light direction angle under sunlight (Optical power = $83mW/cm^2$).

Fig. 62 plots the curves of photocurrent I_L, I_R, and the ratio I_L/I_R versus the angle of the incident light under a constant light intensity of 83 mW/cm^2. The detailed data is listed in Table 2. We tested the data with KEITHLEY 2636A SYSTEM Source Meter. Each photocurrents changes with the light angle. When the angle is zero, I_L and I_R are nearly equal to each other. When the light comes from left side ($\theta < 0$), $I_L > I_R$. And when the light comes from right side ($\theta > 0$), $I_L < I_R$. This means the sensor can function to indicate the incident angle as we analyzed in section 10.2.

The top part of Fig. 63 is the curves of the photocurrents of I_L and I_R at different

Angle(Degree)	$I_R(\mu A)$	$I_L(\mu A)$	I_L/I_R
43	2.628	0.924	2.84416
38	2.8215	1.142	2.47067
33	2.9835	1.366	2.18411
28	3.008	1.5995	1.88059
23	3.0536	1.854	1.64698
18	3.0955	2.134	1.45056
13	3.0335	2.39	1.26925
8	2.901	2.5375	1.14325
3	2.7925	2.6275	1.0628
0	2.69725	2.69725	1
-2	2.6655	2.724	0.97852
-7	2.558	2.83	0.90389
-12	2.452	2.949	0.83147
-17	2.346	3.048	0.76969
-22	2.1035	3.1175	0.67474
-27	1.849	3.1175	0.5931
-32	1.5725	3.0975	0.50767
-37	1.294	3.0195	0.42855
-42	1.032	2.869	0.35971

Table 2. Currents and current ratio of the photodiode v.s. the light direction angle under sunlight(Optical power = $83mW/cm^2$).

angles versus different optical power. The ratio curves of I_L/I_R at different angles are plotted at the bottom part of Fig. 63. It is obviously that for a given angle the ratio almost does not changes over a optical power range of 1-94 mW/cm^2 . This range is much wider than the sunlight intensity in the daytime. The measurement results well meet the analysis conclusion obtained in section 10.2. The conclusion shows that the ratio I_L/I_R is independent on the optical intensity.

To verify the tracking performance, we set up a self-powered optical-mechanical-electronic system as shown in Fig. 64. A solar panel with size of 13 cm $\times$ 8.5 cm is adopted as the power supply of the whole system including the chip and the motor driver.The specification of the solar panel and the motor are shown in Table 3 and

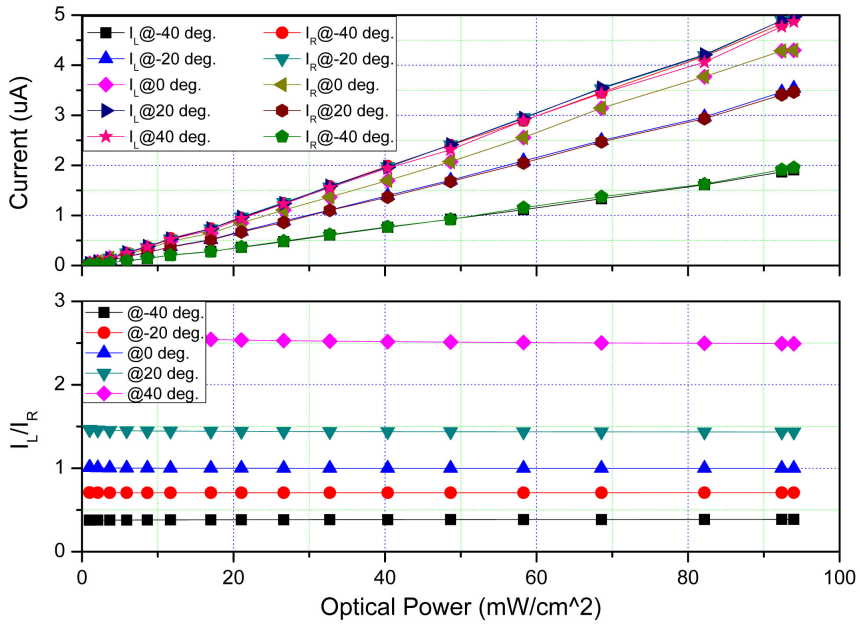

Figure 63. Currents and current ratios of the photodiode v.s. light power (probe station fiber light source).

Table 4. All the solar panel, the chip, and the discrete components are mounted on a bread board which can rotate along an axis by a motor. The motor is driven by the circuit shown in Fig. 59. When this system was put under the sunlight, the system automatically rotates to make the normal of the chip always point to strongest light direction even if the base of the system is moved or rotated. Moreover, when the resistors are set appropriate values, the system works very stable and without any oscillation.

Parameter	Value
Typical Power Output	1.5 W
Typical Output Voltage	4.5 V
Typical Output Current	334 mA
Panel Dimensions	130mm × 85mm × 3mm

Table 3. Parameters of solar panel

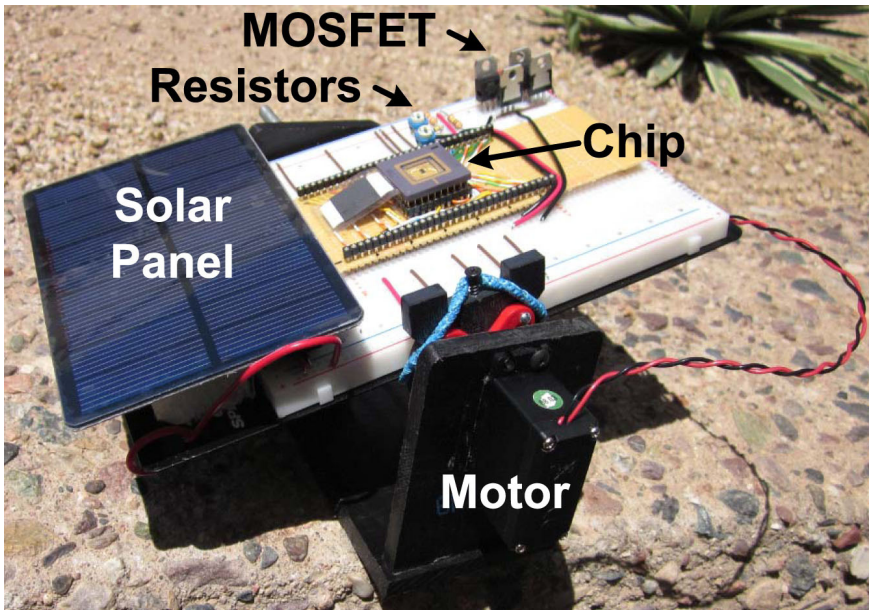

Figure 64. Photograph of the tracking setup.

To further verify the stable angle range, we tested the tracking system in the lab by different light intensities. For there is no a light source in our lab which can illuminate the whole solar panel, we use a power supply for the system in this case and just use the light source to illuminate the chip. Fig. 65 shows the test results of the stable range angels, θ_1 and θ_2. We can see the stable range only change a little over a optical power range of 30-110 mW/cm^2. The tracking accuracy of good as ± 1.8 degrees is achieved.

In order to make the system reliable under the condition of different temperature, strong wind, and other critical circumstances, it is necessary to design the mechanical structure carefully. The motor should provide enough torque and the gear should be able to withstand the maximum torque. The needed torque is determined by weight of the rotating part, the distance of the orthocenter to the axis, the wind velocity, the friction and so on.

Parameter	Value
Operating Voltage	4.8-6.0 Volts
Operating Temperature Range	-20 to +60 Degree C
Operating Speed (4.8V)	0.24sec/60 at no load
Operating Speed (6.0V)	0.20sec/60 at no load
Stall Torque (4.8V)	106.93 oz/in. (7.7kg.cm)
Stall Torque (6.0V)	133.31 oz/in. (9.6kg.cm)
Continuous Rotation Modifiable	Yes
Current Drain (4.8V)	8.8mA/idle and 350mA no load operating
Current Drain (6.0V)	9.1mA/idle and 450mA no load operating
Motor Type	3 Pole Ferrite
Potentiometer Drive	Indirect Drive
Bearing Type	Dual Ball Bearing
Gear Type	3 Metal Gears and 1 Resin Metal Gear
Connector Wire Length	11.81" (300mm)
Dimensions	1.59" × 0.77"× 1.48" (40.6mm × 19.8mm × 37.8mm)
Weight: 1.94oz. (55.2g)	

Table 4. Parameters of motor

10.5 Conclusion

Fabricated in a standard 0.5 μm process, an on-chip sensor for light direction detection is presented. It is integrated with the comparators used for the signal processing in a same chip. The chip, a few discrete components, a motor, and a solar panel are used to implement a self-powered optimal power tracking system. The whole system is powered by the solar panel. The system was tested under the sunlight. Test results show the on-chip sensor work well to detect the light direction and the control circuit can drive the motor to track the strongest light direction sun without any oscillation. The system was also tested in a lab by a optical power range of 30-110 mW/cm^2. In this range the tracking accuracy can be as good as $\pm$1.8 degrees.

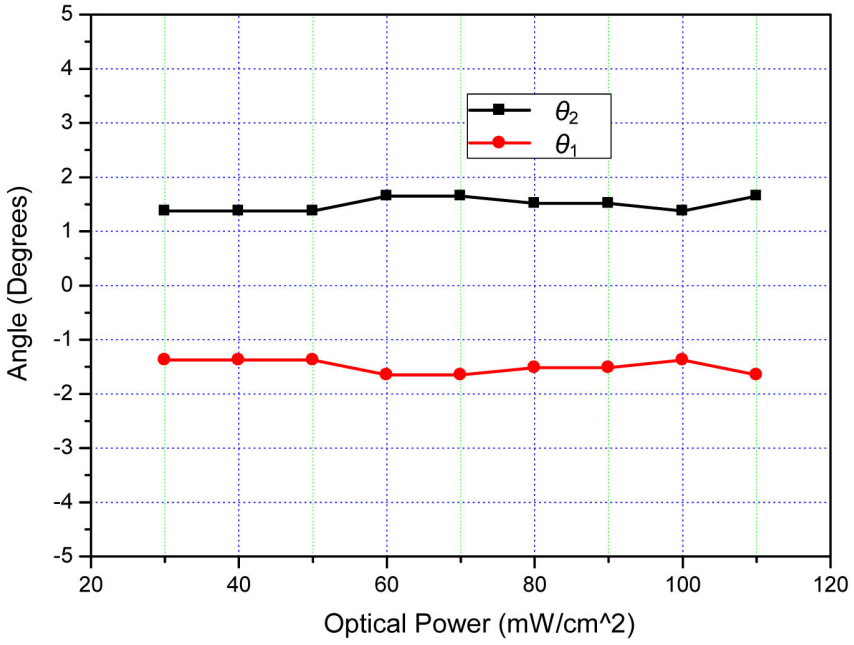

Figure 65. Tracking performance versus light power.

NOTES

REFERENCES

Amemiya, Mitsuaki, and Akira Miyake. 1995. *Angle detecting device and optical apparatus, such as exposure apparatus, employing the same.* US Patent 5,400,386, March.

Anorga, L., A. Rebollo, J. Herran, S. Arana, E. Bandrés, and J. García-Foncillas. 2010. "Development of a DNA Microelectrochemical Biosensor for CEACAM5 Detection." *Sensors Journal, IEEE* 10 (8): 1368–1374.

Ay, S.U. 2011. "A CMOS Energy Harvesting and Imaging (EHI) Active Pixel Sensor (APS) Imager for Retinal Prosthesis." *Biomedical Circuits and Systems, IEEE Transactions on* 5 (6): 535–545.

Bakshi, U.A., and A.P. Godse. 2009. *Analog And Digital Electronics.* Technical Publications.

Bard, Allen J, and Larry R Faulkner. 2000. *Electrochemical Methods: Fundamentals and Applications, 2nd.* Hoboken: Wiley / Sons.

Barker, Geoffrey C., and Arthur W. Gardner. 1992. "Forty years of square-wave polarography." *Analyst* 117 (12): 1811–1828.

Barsoukov, E., and J.R. Macdonald. 2005. *Impedance Spectroscopy: Theory, Experiment, and Applications.* Wiley.

Bhavsar, K., A. Fairchild, E. Alonas, D.K. Bishop, J.T. La Belle, J. Sweeney, T.L. Alford, and L. Joshi. 2009. "A cytokine immunosensor for Multiple Sclerosis detection based upon label-free electrochemical impedance spectroscopy using electroplated printed circuit board electrodes." *Biosensors and Bioelectronics* 25 (2): 506–509.

Cao, Feifei, David Greve, and Irving Oppenheim. 2008. "Development of Microelectrodes for Integrated CMOS Chemical Sensors." *ECS Transactions* 16 (11): 217–225.

Catrysse, Peter B., Xinqiao Liu, and Abbas El Gamal. 2000. "QE reduction due to pixel vignetting in CMOS image sensors." In *Proc. SPIE 3965, Sensors and Camera Systems for Scientific, Industrial, and Digital Photography Applications, 420 (May 15, 2000),* 3965:420–430.

Chang, Byoung-Yong, and Su-Moon Park. 2007. "Fourier Transform Analysis of Chronoamperometric Currents Obtained during Staircase Voltammetric Experiments." *Analytical Chemistry* 79 (13): 4892–4899.

Chen, Aicheng, and Badal Shah. 2013. "Electrochemical sensing and biosensing based on square wave voltammetry." *Anal. Methods* 5 (9): 2158–2173.

Chen, Xuhai, and Min Du. 2010. "FPGA-based floating-point data acquisition system with automatic-gain-control and peak-detection for multi-channel electrochemical measurement." In *Biomedical Engineering and Informatics (BMEI), 2010 3rd International Conference on,* 4:1489–1493. October. doi:10.1109/BMEI.2010.5639374.

Cui, Lin, Jie Wu, and Huangxian Ju. 2015. "Electrochemical sensing of heavy metal ions with inorganic, organic and bio-materials." *Biosensors and Bioelectronics* 63:276–286. doi:http://dx.doi.org/10.1016/j.bios.2014.07.052.

Deans, Matthew C, David Wettergreen, and Daniel Villa. 2005. "A sun tracker for planetary analog rovers." In *8th International Symposium on Artificial Intelligence, Robotics and Automation in Space,* 1–7.

Delgado, F.J., J.M. Quero, J. Garcia, C.L. Tarrida, P.R. Ortega, and S. Bermejo. 2012. "Accurate and Wide-Field-of-View MEMS-Based Sun Sensor for Industrial Applications." *Industrial Electronics, IEEE Transactions on* 59 (12): 4871–4880.

Dong, Yuan, Zhiyu Wen, Haiyang Liao, and Zhongquan Wen. 2007. "Power Self-Regulation Circuit of Piezoelectric Multi-Shaker Micro-Generator." In *Electronic Measurement and Instruments, 2007. ICEMI '07. 8th International Conference on,* 656–660.

Eccles, Gordon N. 1991. "Recent Advances in Pulse Cyclic and Square-Wave Cyclic Voltammetric Analysis." *Critical Reviews in Analytical Chemistry* 22 (5): 345–380. doi:10.1080/10408349108051639.

Economou, A., S.D. Bolis, C.E. Efstathiou, and G.J. Volikakis. 2002. "A "virtual" electroanalytical instrument for square wave voltammetry." *Analytica Chimica Acta* 467 (1–2): 179–188. doi:http://dx.doi.org/10.1016/S0003-2670(02)00191-5.

El Gamal, Abbas, David X. D. Yang, and Boyd A. Fowler. 1999. "Pixel-level processing: why, what, and how?" In *Proc. SPIE 3650, Sensors, Cameras, and Applications for Digital Photography, 2 (March 22, 1999),* 3650:2–13.

Fairchild, A.B., K. McAferty, U.K. Demirok, and J.T. La Belle. 2009. "A label-free, rapid multimarker protein impedance-based immunosensor." In *Complex Medical Engineering, 2009. CME. ICME International Conference on,* 1–5.

Fish, A., S. Hamami, and O. Yadid-Pecht. 2006. "CMOS Image Sensors With Self-Powered Generation Capability." *Circuits and Systems II: Express Briefs, IEEE Transactions on* 53 (11): 1210–1214.

Fish, A., and O. Yadid-Pecht. 2008. "Low-power "Smart" CMOS image sensors." In *Circuits and Systems, 2008. ISCAS 2008. IEEE International Symposium on,* 1408–1411.

Freitas, P., L.G. Dias, A.M. Peres, L.M. Castro, and A.C.A. Veloso. 2012. "Determination of 2,4,6-Trichloroanisole by Cyclic Voltammetry." *Procedia Engineering* 47:1125–1128.

Guan, Mingjie, and Wei-Hsin Liao. 2005. "Comparative analysis of piezoelectric power harvesting circuits for rechargeable batteries." In *Information Acquisition, 2005 IEEE International Conference on,* 243–246.

He, Zhen, and Florian Mansfeld. 2009. "Exploring the use of electrochemical impedance spectroscopy (EIS) in microbial fuel cell studies." *Energy Environ. Sci.* 2 (2): 215–219.

Hegyi, Dennis J. 1993. *System for determining the direction of incident optical radiation.* US Patent 5,264,691, November.

Hill, Jerry M. 1993. *Apparatus and method for angle measurement.* US Patent 5,264,910, November.

Huang, Xinjian, Huilian Chen, Haiqiang Deng, Lishi Wang, Shijun Liao, and Aimin Tang. 2011. "A fast and simple electrochemical impedance spectroscopy measurement technique and its application in portable, low-cost instrument for impedimetric biosensing." *Journal of Electroanalytical Chemistry* 657 (1–2): 158–163.

Huang, Yue, Ying Liu, B.L. Hassler, R.M. Worden, and A.J. Mason. 2013. "A Protein-Based Electrochemical Biosensor Array Platform for Integrated Microsystems." *Biomedical Circuits and Systems, IEEE Transactions on* 7 (1): 43–51.

Hwang, Sungkil, C.N. LaFratta, V. Agarwal, Xin Yu, D.R. Walt, and S. Sonkusale. 2009. "CMOS Microelectrode Array for Electrochemical Lab-on-a-Chip Applications." *Sensors Journal, IEEE* 9 (6): 609–615.

Jang, Ling-Sheng, and Min-How Wang. 2007. "Microfluidic device for cell capture and impedance measurement." *Biomedical microdevices* 9 (5): 737–743.

Jurczakowski, Rafał, and Andrzej Lasia. 2004. "Limitations of the Potential Step Technique to Impedance Measurements Using Discrete Time Fourier Transform." *Analytical Chemistry* 76 (17): 5033–5038.

Karimov, Kh.S., M.A. Saqib, P. Akhter, M.M. Ahmed, J.A. Chattha, and S.A. Yousafzai. 2005. "A simple photo-voltaic tracking system." *Solar Energy Materials and Solar Cells* 87:49–59.

Koyuncu, B., and K. Balasubramanian. 1991. "A microprocessor controlled automatic sun tracker." *Consumer Electronics, IEEE Transactions on* 37 (4): 913–917.

Kozak, Mucahit, and Izzet Kale. 2003. *Oversampled Delta-Sigma Modulators: Analysis, Applications, and Novel Topologies.* Kluwer Academic Publishers.

La Belle, Jeffrey T., Ugur Korcan Demirok, Dharmendra R. Patel, and Curtiss B. Cook. 2011. "Development of a novel single sensor multiplexed marker assay." *Analyst* 136 (7): 1496–1501.

Law, M.K., A. Bermak, and C. Shi. 2011. "A Low-Power Energy-Harvesting Logarithmic CMOS Image Sensor With Reconfigurable Resolution Using Two-Level Quantization Scheme." *Circuits and Systems II: Express Briefs, IEEE Transactions on* 58 (2): 80–84.

Lee, Chia-Yen, Po-Cheng Chou, Che-Ming Chiang, and Chiu-Feng Lin. 2009. "Sun tracking systems: a review." *Sensors* 9 (5): 3875–3890.

Lee, Hakho, Yong Liu, Donhee Ham, and Robert M. Westervelt. 2007. "Integrated cell manipulation system-CMOS/microfluidic hybrid." *Lab Chip* 7 (3): 331–337.

Lehmann, U., M. Sergio, S. Pietrocola, E. Dupont, C. Niclass, M.A.M. Gijs, and E. Charbon. 2008. "Microparticle photometry in a CMOS microsystem combining magnetic actuation and in situ optical detection." *Sensors and Actuators B: Chemical* 132 (2): 411–417.

Li, Lin, Xiaowen Liu, W.A. Qureshi, and Andrew J. Mason. 2011. "CMOS Amperometric Instrumentation and Packaging for Biosensor Array Applications." *Biomedical Circuits and Systems, IEEE Transactions on* 5 (5): 439–448.

Liebe, C.C., and S. Mobasser. 2001. "MEMS based Sun sensor." In *Aerospace Conference, 2001, IEEE Proceedings.* 3:1565–1572.

Lim, Byounghyun, Masato Futagawa, Sou Takahashi, Fumihiro Dasai, Makoto Ishida, and Kazuaki Sawada. 2013. "Integrated Square Wave Voltammetry Redox Sensor System for Electrochemical Analysis." *Japanese Journal of Applied Physics* 52 (4): 116502.

———. 2014. "Integrated 8 × 8 array redox sensor system employing on-chip square wave voltammetric circuit for multi point and high-speed detection." *Japanese Journal of Applied Physics* 53 (4): 046502.

Lovric, Milivoj. 2002. *Electroanalytical Methods.* Springer Berlin.

Luo, Tao, Hongyi Wang, Hongjiang Song, and J.B. Christen. 2013. "CMOS potentiostat for chemical sensing applications." In *SENSORS, 2013 IEEE,* 1–4.

———. 2014. "CMOS-based on-chip electrochemical sensor." In *Biomedical Circuits and Systems Conference (BioCAS), 2014 IEEE,* 336–339.

Manickam, A., A. Chevalier, M. McDermott, A.D. Ellington, and A. Hassibi. 2010. "A CMOS Electrochemical Impedance Spectroscopy (EIS) Biosensor Array." *Biomedical Circuits and Systems, IEEE Transactions on* 4 (6): 379–390.

Mason, A., Yue Huang, Chao Yang, and Jichun Zhang. 2007. "Amperometric Readout and Electrode Array Chip for Bioelectrochemical Sensors." In *Circuits and Systems, 2007. ISCAS 2007. IEEE International Symposium on,* 3562–3565.

Mirceski, V., S. Komorsky-Lovric, and M. Lovric. 2007. *Square-Wave Voltammetry: Theory and Application.* Springer.

Mirceski, Valentin, Rubin Gulaboski, Milivoj Lovric, Ivan Bogeski, Reinhard Kappl, and Markus Hoth. 2013. "Square-Wave Voltammetry: A Review on the Recent Progress." *Electroanalysis* 25 (11): 2411–2422.

Mobasser, S., and C.C. Liebe. 2003. "MEMS based sun sensor on a chip." In *Control Applications, 2003. CCA 2003. Proceedings of 2003 IEEE Conference on,* 2:1483–1487. June.

Mobasser, Sohrab, and Carl Christian Liebe. 2004. "Micro sun sensor for spacecraft attitude control." In *International Federation of Automatic Control, St. Petersburg, Russia, June 14-18, 2004.*

Mohammad, Nur, and Tarequl Karim. 2013. "Design and Implementation of Hybrid Automatic Solar-Tracking System." *Journal of Solar Energy Engineering* 135 (1): 011013.

Mohsen, Q, Sahar A Fadl-allah, and Nahla S El-Shenawy. 2012. "Electrochemical impedance spectroscopy study of the adsorption behavior of bovine serum albumin at biomimetic calcium–phosphate coating." *Int. J. Electrochem. Sci* 7 (5): 4510–4527.

Mousazadeh, Hossein, Alireza Keyhani, Arzhang Javadi, Hossein Mobli, Karen Abrinia, and Ahmad Sharifi. 2009. "A review of principle and sun-tracking methods for maximizing solar systems output." *Renewable and Sustainable Energy Reviews* 13 (8): 1800–1818.

Nagatani, Naoki, Keiichiro Yamanaka, Masato Saito, Ritsuko Koketsu, Tadahiro Sasaki, Kazuyoshi Ikuta, Toshiro Miyahara, and Eiichi Tamiya. 2011. "Semi-real time electrochemical monitoring for influenza virus RNA by reverse transcription loop-mediated isothermal amplification using a USB powered portable potentiostat." *Analyst* 136 (24): 5143–5150. doi:10.1039/C1AN15638A.

Nazari, M.H., H. Mazhab-Jafari, Lian Leng, A. Guenther, and R. Genov. 2013. "CMOS Neurotransmitter Microarray: 96-Channel Integrated Potentiostat With On-Die Microsensors." *Biomedical Circuits and Systems, IEEE Transactions on* 7 (3): 338–348.

Nicholson, R. S., and Irving. Shain. 1964. "Theory of Stationary Electrode Polarography. Single Scan and Cyclic Methods Applied to Reversible, Irreversible, and Kinetic Systems." *Analytical Chemistry* 36 (4): 706–723.

Nishikata, A., Y. Ichihara, and T. Tsuru. 1995. "An application of electrochemical impedance spectroscopy to atmospheric corrosion study." *Corrosion Science* 37 (6): 897–911.

Ortmanns, Maurits, and Friedel Gerfers. 2006. *Continuous-Time Sigma-Delta A/D Conversion: Fundamentals, Performance Limits and Robust Implementations.* Springer.

Pellicer, Cristina, Alberto Gomez-Caballero, Nora Unceta, M. Aranzazu Goicolea, and Ramon J. Barrio. 2010. "Using a portable device based on a screen-printed sensor modified with a molecularly imprinted polymer for the determination of the insecticide fenitrothion in forest samples." *Anal. Methods* 2 (9): 1280–1285. doi:10.1039/C0AY00329H.

Pineda, F., and C.A. Arredondo. 2012. "Design and implementation of sun tracker prototype for solar module positioning." In *Photovoltaic Specialists Conference PVSC, 2012 38th IEEE,* 002905–002910. June.

Pissavin, P, JP Krebs, P LeLong, Ph Vidal, and R Navoni. 1997. "Improved star tracker for Odin satellite." In *Spacecraft Guidance, Navigation and Control Systems,* 381:611–616.

Prodromakis, T., K. Michelakisy, T. Zoumpoulidis, R. Dekker, and C. Toumazou. 2009. "Biocompatible encapsulation of CMOS based chemical sensors." In *Sensors, 2009 IEEE,* 791–794.

Quero, J.M., A. Guerrero, L.G. Franquelo, M. Dominguez, I. Ameijeiras, and L. Castaner. 2001. "Light source position microsensor." In *Circuits and Systems, 2001. ISCAS 2001. The 2001 IEEE International Symposium on,* 3:648–651.

Radke, S.M., and E.C. Alocilja. 2005. "A microfabricated biosensor for detecting foodborne bioterrorism agents." *Sensors Journal, IEEE* 5 (4): 744–750.

Randles, J. E. B. 1948. "A cathode ray polarograph. Part II. The current-voltage curves." *Trans. Faraday Soc.* 44:327–338.

Rattanarat, Poomrat, Wijitar Dungchai, David Cate, John Volckens, Orawon Chailapakul, and Charles S. Henry. 2014. "Multilayer Paper-Based Device for Colorimetric and Electrochemical Quantification of Metals." *Analytical Chemistry* 86 (7): 3555–3562. doi:10.1021/ac5000224.

Ruzic, I. 1972. "On the theory of Kalousek commutator, square-wave and related techniques: I. Equations for current-potential curves." *Journal of Electroanalytical Chemistry and Interfacial Electrochemistry* 39 (1): 111–122.

Sarkar, P., and S. Chakrabartty. 2013. "A compressive piezoelectric front-end circuit for self-powered mechanical impact detectors." In *Circuits and Systems (ISCAS), 2013 IEEE International Symposium on,* 2207–2210.

Schreier, Richard, and Gabor C Temes. 2005. *Understanding Delta-Sigma Data Converters.* A John Wiley & Sons, INC.

Stanacevic, M., K. Murari, A. Rege, G. Cauwenberghs, and N.V. Thakor. 2007. "VLSI Potentiostat Array With Oversampling Gain Modulation for Wide-Range Neurotransmitter Sensing." *Biomedical Circuits and Systems, IEEE Transactions on* 1 (1): 63–72.

Strycharz, Sarah M., Anthony P. Malanoski, Rachel M. Snider, Hana Yi, Derek R. Lovley, and Leonard M. Tender. 2011. "Application of cyclic voltammetry to investigate enhanced catalytic current generation by biofilm-modified anodes of

Geobacter sulfurreducens strain DL1 vs. variant strain KN400." *Energy Environ. Sci.* 4 (3): 896–913.

Wang, Hongyi, Tao Luo, Youyou Fan, Zhijian Lu, Hongjiang Song, and Jennifer Blain Christen. 2015. "A self-powered single-axis maximum power direction tracking system with an on-chip sensor." *Solar Energy* 112:100–107.

Wang, Hongyi, Tao Luo, Zhijian Lu, Hongjiang Song, and Jennifer Blain Christen. 2014. "CMOS self-powered monolithic light-direction sensor with digitalized output." *Opt. Lett.* 39 (9): 2618–2621.

Wang, Hongyi, Tao Luo, Hongjiang Song, and Jennifer Blain Christen. 2013. "On-chip sensor for light direction detection." *Opt. Lett.* 38 (22): 4554–4557.

Wang, Hua, Yan Chen, A. Hassibi, A. Scherer, and A. Hajimiri. 2009. "A frequency-shift CMOS magnetic biosensor array with single-bead sensitivity and no external magnet." In *Solid-State Circuits Conference - Digest of Technical Papers, 2009. ISSCC 2009. IEEE International,* 438–439, 439a.

Wang, Joseph. 2006. *Analytical Electrochemistry.* John Wiley & Sons.

Warren-Smith, Stephen C., Sabrina Heng, Heike Ebendorff-Heidepriem, Andrew D. Abell, and Tanya M. Monro. 2011. "Fluorescence-Based Aluminum Ion Sensing Using a Surface-Functionalized Microstructured Optical Fiber." *Langmuir* 27 (9): 5680–5685.

Wei, Yan, Chao Gao, Fan-Li Meng, Hui-Hua Li, Lun Wang, Jin-Huai Liu, and Xing-Jiu Huang. 2012. "SnO2/Reduced Graphene Oxide Nanocomposite for the Simultaneous Electrochemical Detection of Cadmium(II), Lead(II), Copper(II), and Mercury(II): An Interesting Favorable Mutual Interference." *The Journal of Physical Chemistry C* 116 (1): 1034–1041. doi:10.1021/jp209805c.

Yamada, M., Y. Maeda, M. Nakamura, T. Terada, and M. Shirai. 1996. *Photosensor for detecting the position of incident light in two dimensions using a pair of film resistors and a photoconductive element sandwiched therebetween.* US Patent 5,517,017, May.

Yang, Chao, Yue Huang, B.L. Hassler, R.M. Worden, and A.J. Mason. 2009. "Amperometric Electrochemical Microsystem for a Miniaturized Protein Biosensor Array." *Biomedical Circuits and Systems, IEEE Transactions on* 3 (3): 160–168.

Yang, Chao, S.R. Jadhav, R.M. Worden, and A.J. Mason. 2009. "Compact Low-Power Impedance-to-Digital Converter for Sensor Array Microsystems." *Solid-State Circuits, IEEE Journal of* 44 (10): 2844–2855.

Yoo, Jung-Suk, and Su-Moon Park. 2000. "An Electrochemical Impedance Measurement Technique Employing Fourier Transform." *Analytical Chemistry* 72 (9): 2035–2041.

Yoo, Jung-Suk, Inja Song, Ji-Hun Lee, and Su-Moon Park. 2003. "Real-Time Impedance Measurements during Electrochemical Experiments and Their Application to Aniline Oxidation." *Analytical Chemistry* 75 (14): 3294–3300.